



5-2018

Advanced Time-of-Flight Diamond Detection Systems

Ahmed Ali Alghamdi

University of Tennessee, aalgham2@vols.utk.edu

Follow this and additional works at: https://trace.tennessee.edu/utk_graddiss

Recommended Citation

Alghamdi, Ahmed Ali, "Advanced Time-of-Flight Diamond Detection Systems. " PhD diss., University of Tennessee, 2018.

https://trace.tennessee.edu/utk_graddiss/4962

This Dissertation is brought to you for free and open access by the Graduate School at TRACE: Tennessee Research and Creative Exchange. It has been accepted for inclusion in Doctoral Dissertations by an authorized administrator of TRACE: Tennessee Research and Creative Exchange. For more information, please contact trace@utk.edu.

To the Graduate Council:

I am submitting herewith a dissertation written by Ahmed Ali Alghamdi entitled "Advanced Time-of-Flight Diamond Detection Systems." I have examined the final electronic copy of this dissertation for form and content and recommend that it be accepted in partial fulfillment of the requirements for the degree of Doctor of Philosophy, with a major in Nuclear Engineering.

Eric D. Lukosi, Major Professor

We have read this dissertation and recommend its acceptance:

Jason P. Hayward, Lawrence H. Heilbronn, Stefan M. Spanier

Accepted for the Council:

Dixie L. Thompson

Vice Provost and Dean of the Graduate School

(Original signatures are on file with official student records.)

Advanced Time-of-Flight Diamond Detection Systems

A Dissertation Presented for the
Doctor of Philosophy
Degree
The University of Tennessee, Knoxville

Ahmed Ali Alghamdi
May 2018

© by Ahmed Ali Alghamdi, 2018
All Rights Reserved.

This work is dedicated to my mother and my dearly departed father for their endless support and devotion.

Acknowledgments

I would like to express my sincere gratitude to my Ph.D. advisor and mentor, Dr. Eric Lukosi, who has guided and motivated me in accomplishing this research. I would also like to thank Dr. Lawrence Heilbronn for giving me the opportunity to work on the beamline experiment. It could not have been done without his help and support. I would also like to thank my other Ph.D. committee members, Dr. Jason Hayward and Dr. Stefan Spanier for their interest and valuable comments on the research. Also, I thank Scott Emert for his support and patience. My sincerest thanks are extended to Dr. Michael Sivertz from Brookhaven National Lab for his encouragement and guidance. I am also grateful to the radiation safety department at the University of Tennessee for helping me through the DNSC experiment. To my mother, brothers and sisters, thank you for great encouragement and support. My beautiful wife, Rawan, has been my helpmate throughout my scholastic endeavors. To my daughter and son, Lateen and Eyad, you were my strength throughout one of the toughest years in my life. To my friends, thank you for your love and encouragement throughout my life. I would like also to thank all my team members for their support, Thomas Wulz, Elan Herrera, Danial Hamm, Ryan Priest, Michael (Dylan) Richardson, and Mikah Rust. You made my life much easier with your advice and encouragement. Special thanks to Dr. Callie Goetz for proofreading my dissertation and providing valuable feedback. Finally, I would like also to express my gratitude and appreciation to my sponsor KACST for the generous scholarship to pursue my Ph.D.

“Seek knowledge from the Cradle to the Grave”

- Prophet Muhammad PBUH

Abstract

The radiation detection field has been rapidly growing in the recent three decades due to the Special Nuclear Materials (SNM) proliferation hazards. Monitoring and detecting SNM with high resolution has been a practical issue. Recently, Neutron Scatter Camera (NSC) addressed this issue by identifying the different SNM with high efficiency. However, the huge size of the detection system beside the poor resolution requires developing an alternative NSC. Two Diamond-based Neutron Scatter Camera (DNSC) systems were investigated. The two-diamond array demonstrated good energy resolution of reconstructing spectrum of multiple neutron sources. Moreover, the spectrum of $^{239}\text{PuBe}$ source was reconstructed experimentally via the two-diamond array NSC. The measured spectrum agreed well with the peak of 3 and 10 MeV. On the other hand, the diamond array, in addition to its capability of spectroscopy, pinpointed several neutron sources. For instance, the simulated system could locate and identify a highly active ^{252}Cf source (2.3×10^{10} n/s) placed 1 meter away within 6 hours.

The Chi-Nu measurements started back in 2012 at Los Alamos National Lab to obtain more accurate data of fission neutrons. In this dissertation, a novel Double Time-of-Flight (DToF) detection system was utilized to investigate the capability of reconstructing the prompt fission neutrons spectra that were produced by the fast neutron irradiation of two fissile materials which coated a diamond detector. Unlike the Chi-Nu, DToF simulation measurements used only one type of detector (diamond detectors) for all neutron energy range. The simulation results represented good resolution but more accurate correction factors are needed for the low detection efficiency ($\approx 3\%$) of the system.

Protecting astronauts for future space missions from galactic cosmic rays (GCR) is an issue for NASA. Identifying the light ions that strike through the spaceship craft is the

first goal to design a shielding material. To address this issue, a $\Delta E/\Delta E$ detector was explored for the measurement of Minimum Ionizing Particles (MIPs) using the beam-line at the NASA Space Radiation Laboratory (NSRL). The measurements were analyzed by Geant4 simulation, which showed promising results in using a $\Delta E/\Delta E$ detector to define interacted isotopes.

Table of Contents

1	Introduction	1
1.1	Novel Contribution	2
2	Background	3
2.1	Synthetic Diamond	3
2.1.1	Chemical Vapor Deposition Growth Technique	4
2.1.2	Single-Crystal Diamond Detector	5
2.2	Particle Detection and Spectroscopy	6
2.2.1	Neutron Particles	6
2.2.2	Charged Particles	9
2.3	Time-of-Flight Spectrometer	12
2.3.1	Neutron Scatter Camera	13
3	Diamond-based Neutron Scatter Camera	17
3.1	Introduction	17
3.2	Monte Carlo Simulation	18
3.3	Post-Processing Algorithm	21
3.3.1	Two-Diamond Array	22
3.3.2	Diamond Array System	24
3.4	Uncertainty Calculation	25
3.5	DN-SC Efficiency and Resolution Properties	27
3.5.1	Detection Efficiency	28
3.5.2	Energy Resolution	28

3.6	Experimental Setup	29
3.7	Results	33
3.7.1	Two-Diamond Array	33
3.7.2	Diamond Array System	42
4	Diamond Time-of-Flight Detector	50
4.1	Introduction	50
4.2	MCNP code	51
4.3	Data Analysis	51
4.4	Results	53
4.4.1	Prompt Fission Spectrum	53
4.4.2	Neutron Multiplicity Counter	55
4.4.3	$\bar{\nu}$ Calculation	56
5	$\Delta E/\Delta E$ Diamond Detector	58
5.1	Introduction	58
5.2	Experimental Approach	58
5.3	Geant4 Simulation	61
5.4	Results	63
5.4.1	Position 1 Measurements	63
5.4.2	Position 2 Measurements	65
6	Conclusions and Future Work	70
6.1	Conclusions	70
6.2	Future Work	72
	Bibliography	74
	Appendices	84
A	$\Delta E/\Delta E$ detection system recorded runs.	85
	Vita	91

List of Tables

2.1	Physical properties of solid-state detectors at room temperature(300 K). . .	4
2.2	Electronic characteristics of CVD diamond detectors.	5
2.3	Main fast neutron reaction with SDD.	8
3.1	Configuration of simulated point sources.	44
3.2	Expected measurement time for each configuration.	47
3.3	Diamond array NSC resolution and number of cones for different energy thresholds.	48
4.1	Detection efficiency of the DToF system.	57
5.1	$\Delta E/\Delta E$ detection system recorded runs.	60

List of Figures

2.1	Cross-section of neutron interactions with carbon atom. Green and blue cross-section stand for the elastic and inelastic scattering, respectively. Other interactions represent absorption cross-section.	6
2.2	Energy deposition spectra of distinct neutron projectiles with SDD.	7
2.3	Pulse height spectrum of two neutron projectiles, 20.5 MeV (black) and 8.3 MeV(blue), with SDD.	9
2.4	^{241}Am α source spectroscopy using (left) Si detector and (right) SDD.	11
2.5	^{252}Cf source measurements using ToF technique (a) ToF distribution for γ rays and neutrons. (b) Spontaneous neutron fission spectrum.	12
2.6	Back-projection scheme for a double neutron scattered event.	14
2.7	NSC back-projected image of ^{252}Cf source placed 30 m away.	16
2.8	(left) Schematic of an SVSC-PiPS system. (right) Reconstructed image for a ^{252}Cf source located 1m from the center of detection system; x indecats the true source position.	16
3.1	^{252}Cf and $^{239}\text{Pu-Be}$ neutron sources spectra.	20
3.2	Relationship between the angular distribution, neutron recoil angle in CM, and neutron energy. The plot was generated from CENDL-3.1 ENDF neutron library.	21
3.3	The flowchart of C++ code to extract double-scattering events from DNSC PTRAC output files.	23
3.4	Illustration of the back-projection technique with two pixelated diamonds.	25
3.5	Walk and jitter uncertainties in leading-edge discriminator mode.	26

3.6	5 MeV reconstructed peak using two-diamond array NSC.	29
3.7	Screen shot of the designed PCB board in the Altium software.	30
3.8	Aluminum box enclosure.	31
3.9	Electronic block diagram of the two-diamond system NSC.	32
3.10	CAEN digitizer acquisition window.	32
3.11	Reconstructed 1 MeV neutron energy of the two-diamond system in various separation distances.	33
3.12	Two-diamond array NSC setup.	34
3.13	Detection efficiency and energy resolution of the two-diamond array system.	35
3.14	Two-diamond NSC system counts per hour for an isotropic ^{239}Pu -Be source.	35
3.15	(a) Simulated neutron source and obtained spectrum. (b) Correction factor for the neutron source.	36
3.16	The reconstructed spectrum of ^{252}Cf source using two-diamond NSC.	37
3.17	The reconstructed spectrum of ^{239}Pu -Be source using two-diamond NSC. . .	37
3.18	16-pixel two-diamond array reconstructed spectrum for (a) ^{252}Cf source and (b) ^{239}Pu -Be source.	38
3.19	Arrangement of the two-diamond array NSC experiment.	40
3.20	Pulse height spectrum of ^{239}Pu -Be source in the second SDD.	41
3.21	Reconstructed neutron spectrum of the ^{239}Pu -Be source.	41
3.22	Schematic view of the diamond array NSC.	42
3.23	Diamond array system reconstructed spectrum of (a) ^{252}Cf source (b) ^{239}Pu - Be source.	43
3.24	Diamond array system reconstructed images for configuration No. (a) 1 (b) 2 (c) 3 and (d) 4 as listed in Table 3.1.	45
3.25	Reconstructed image planes for two 4 MeV mono-energetic neutron sources located at (10, 100, 0) and (0, 100, 10) for multiple cone rates (a) 10 cones (b) 50 cones (c) 500 cones.	46
3.26	Reconstructed image planes for two 4 MeV mono-energetic neutron sources located at (10, 100, 0) and (0, 100, 10) for different Y distances (a) 20 cm (b) 100 cm (c) 200 cm.	46

3.27	The 2D profiles of (a) horizontal and (b) vertical axes of the reconstructed image for a ^{252}Cf point source located at (0,10,0).	48
4.1	Schematic view of the DToF detection system.	52
4.2	Total numbers of detected neutrons for ^{239}Pu target with 1 MeV incoming neutron.	53
4.3	The prompt fission neutron spectra of the 1 MeV incident neutron with 1000 μm thick target of (a) ^{235}U (b) ^{239}Pu	54
4.4	The prompt fission neutron spectra of the 4 MeV incident neutron with 1000 μm thick target of (a) ^{235}U (b) ^{239}Pu	54
4.5	Neutron multiplicity factor for the 1 MeV neutron source and 1000 μm thick target of (a) ^{235}U (b) ^{239}Pu	55
4.6	Neutron Multiplicity factor for the 4 MeV neutron source and 1000 μm thick target of (a) ^{235}U (b) ^{239}Pu	56
4.7	$\bar{\nu}$ measurements of the DToF detection system.	57
5.1	Layout of the $\Delta E/\Delta E$ detection system inside the aluminum enclosure. . . .	59
5.2	A schematic of the signal chain of the $\Delta E/\Delta E$ detection system.	60
5.3	$\Delta E/\Delta E$ experimental arrangements.	61
5.4	$\Delta E/\Delta E$ detection system located in position 2 at the NSRL beam room. . .	62
5.5	800 MeV proton beam (a) Geant4 simulation spectra (b) experimental measured spectra (c) simulated $\Delta E/\Delta E$ measurements and (d) experimental $\Delta E/\Delta E$	64
5.6	Experimental versus simulation spectra for (a) 2.5 GeV and (c) 800 MeV proton beams. Simulated spectra for different upstream target thicknesses of (b) 2.5 GeV and (d) 800 MeV proton projectiles.	66
5.7	Interacted particles with first diamond detector for proton beams (a) 2.5 GeV and (b) 800 MeV	67
5.8	(a) 400 MeV beam measurements and experimental results. (b) Simulated spectra of 400 MeV proton beam for all upstream target thicknesses.	68
5.9	First diamond detector interacted particles of 400 MeV proton beam.	68

5.10 Identification of hydrogen isotopes ion using ToF and $\Delta E1$ for Fe-400 AMeV simulated projectile.	69
A.1 $\Delta E/\Delta E$ spectral analysis of 2.5 GeV proton beam.	85
A.2 $\Delta E/\Delta E$ spectral analysis of 800 MeV proton beam.	86
A.3 $\Delta E/\Delta E$ spectral analysis of 400 MeV proton beam.	87
A.4 $\Delta E/\Delta E$ spectral analysis of 400 MeV iron beam.	88
A.5 $\Delta E/\Delta E$ spectral analysis of 800 MeV iron beam.	89
A.6 $\Delta E/\Delta E$ spectral analysis of 1474 MeV iron beam and 400 and 800 MeV helium beams	90

Chapter 1

Introduction

The threat of proliferation of special nuclear material (SNM) has been rapidly growing both within the USA and worldwide. Many approaches are under investigation and development in order to detect and identify SNM through emitted γ and neutron radiation. γ -rays are easily shielded but neutrons are highly penetrating which makes them ideal candidates for SNM monitoring. Consequently, immense efforts have been put forth to develop methods for the detection of neutrons emitted by SNM. Currently, neutron measurements are most often conducted using ^3He as well as scintillation detectors. However, due to the shortage in ^3He isotopes beside the limited energy resolution of scintillators detectors lead to the need of alternative detectors [1].

The evolution of semiconducting materials has resulted in other advanced detectors with promising detection characteristics such as high carrier mobility, superior electrical properties and the compact size [2]. In particular, a diamond detector has several promising features for neutron detection. Namely, fast responsive signal, low atomic number and high radiation hardness. Moreover, the carbon atom has a high neutron elastic scattering cross-section as well as several usable fast neutron reactions. The combination of these features make the diamond detector a good candidate for neutron Time-of-flight (ToF) applications [3]. Nevertheless, diamond detector are considered as an insulator material due to the high-band gap.

1.1 Novel Contribution

The proposed work describes the use of diamond-based radiation detection systems for a variety of applications. One such application is a novel Diamond-based Neutron Scatter Camera (DNSC). DNSC uses elastic scattering interactions to reconstruct the neutron source spectrum and its location. The DNSC was investigated computationally and benchmarked experimentally through choice experiments.

The second application of diamond detectors is the simulation of a novel Double Time-of-Flight (DToF) detection system that utilizes many diamond detectors for spectroscopic analysis of fissile and fissionable materials under fast neutron irradiation. A target diamond detector is coated with a thin layer of fissile material. Then, an array of diamond detectors surrounds the target, and the excellent timing performance of the diamond detectors is used to discriminate between the interrogating neutron beam and the interaction of fission neutrons with the surrounding diamond detectors. Simulations considered the placement and number of diamond detectors and compared their performance to other detection systems currently used for measuring the fast neutron-induced fission neutron spectrum and multiplicity, such as the LiI detectors in the Chi-Nu campaign [4].

The third, and final, application of diamond sensors is a $\Delta E/\Delta E$ detector for the measurement of Minimum Ionizing Particles (MIPs). Experiments utilized two diamond detectors and investigated light ions traveling through the detector from a variety of incident particles striking thick targets. The experiments were conducted using the beam line at the NASA Space Radiation Laboratory (NSRL) at Brookhaven National Lab (BNL).

Chapter 2

Background

Natural diamond is an attractive material because of its many mechanical characteristics [5]. The extreme hardness comes from its crystalline structure, cubic lattice with tetrahedral covalent bonds between carbon atoms [6]. However, the rareness of diamond and presence of defects or impurities in natural diamond affect the usefulness of natural diamond in the radiation detection field. As a result, Chemical Vapor Deposition (CVD) growth of diamond has been used to produce synthetic diamond with sufficient properties for radiation detection applications.

2.1 Synthetic Diamond

High pressure and high temperature (HPHT) was the first growth technique used for synthetic diamond production [6]. The synthetic diamond was fabricated by simulating the natural thermodynamic conditions on a diamond substrate. The HPHT technique has successfully grown synthetic diamond with the same crystal shape of natural diamond [7]. Still, the high impurity of the grown diamond yields poor electrical properties. In the 1980s, a new growth technique, chemical vapor deposition (CVD), was utilized to grow diamond with adequate electrical properties [8].

2.1.1 Chemical Vapor Deposition Growth Technique

CVD growth mechanisms involve treating a hydrogen plasma and methane gas with high temperature (~ 2000 °C) and low pressure (30-300 Torr) to induce chemical reactions with the heated substrate surface (>600 °C), resulting in a diamond crystal growth [6, 8, 9]. In the 1990s, the first polycrystalline CVD (pcCVD) diamond detector with a higher charge collection distance was introduced [8]. Table 2.1 shows the extraordinary physical properties of synthetic diamond detectors compared to other solid-state detectors.

Table 2.1: Physical properties of solid-state detectors at room temperature(300 K)^a.

Properties	Diamond	Si	Ge ^b	GaAs ^b
Atomic number ^b	6	14	32	31,33
Mass density (g/cm ³) ^b	3.51	4.96	4.41	4.43
Band gap (eV)	5.5	1.12	0.67	1.42
Resistivity ($\Omega.cm$)	$> 10^{11}$	2.3×10^5	47	10^8
Thermal conductivity (W/cm/K)	20	1.27	0.60	0.45
Electron mobility (cm ² /V/s)	1800	1500	3900	8500
Hole mobility (cm ² /V/s)	1200	600	1900	400
Dielectric constant	5.7	11.9	16.3	13.1
Energy to create an $e-h$ pair (eV)	13	3.6	3@77K	4.3

^a All data taken from Michimasa et. al. 2013 [10] unless otherwise mentioned.

^b Data taken from [11].

Due to the large band gap and relatively small dielectric constant, diamond detectors exhibit low leakage current and detector capacitance, respectively..The large displacement energy (43 eV) results in a high radiation hardness. These superior characteristics make diamond suitable to use in a high-radiation environment compared to other semiconductor detectors [10]. However, De Boer *et.al.* demonstrated the decrease of the output signal of diamond detector by a factor of two due to the extreme irradiation of 24 GeV proton beam ($6 * 10^{15}$ p/cm²). In the same study, it was found that the high fluence of neutron irradiation for energy below 100 MeV made the silicon detector harder by a factor of two to three (the

factor value differs based on the neutron energy) than pcCVD due to the high carbon elastic scattering cross-section. However, the low band gap of silicon detector found the necessity of cooling detector [12].

Moreover, high carrier mobilities of the diamond detector yield an extremely fast charge collection time. All of these features make the diamond sensor a strong candidate for timing measurements for neutron and high-energy physics experiments [13]. However, studies have shown that the pcCVD diamond has a significant issue with charge collection due to grain boundaries [14]. Because of poor collection efficiency, RD42 began collaborating in 1994 to develop the CVD technique to grow a higher quality of CVD diamond detectors [15].

2.1.2 Single-Crystal Diamond Detector

In 2002, the Element Six company created the first single-crystal CVD (SDD) diamond detector [9]. Two main advantages of the SDD over the pcCVD include a longer charge carrier lifetime and high drift mobility [16]. Table 2.2 indicates the significant electronic SDD performance.

Table 2.2: Electronic characteristics of CVD diamond detectors [6].

Properties	Polycrystalline	Single Crystal
Electron mobility (cm ² /V s)	1800	>2000
Hole mobility (cm ² /V s)	1000	>2000
Carrier lifetime (ns)	1-10	2000
Charge Collection Efficiency (for 500 μ m plate)	36%	95%

Charge collection efficiency (CCE) is the amount of charge measured from a radiation interaction in the diamond detector [17]. SDD shows significant improvement in CCE compared to pcCVD due to the higher carrier mobility and lifetime. In addition, SDD carrier mobilities show faster responsive signal than pcCVD. However, recent studies reveal even higher carrier mobility [9]. Carrier drift mobility and mobility-lifetime play key roles in energy resolution [16]; subsequently, SDDs have been widely adopted in the radiation detection field as described in the next section.

2.2 Particle Detection and Spectroscopy

2.2.1 Neutron Particles

The neutron particle is considered one of the basic constituents of the atom nucleus. A neutron is part of all nuclei except in a hydrogen atom (^1H) [18]. Because it lacks an electric charge, a neutron penetrates deeply through objects. It interacts via the nuclear force. In other words, the neutron interacts only with nuclei. The probability of reaction (cross-section) depends mainly on the projectile neutron energy, the target nucleus, and the type of interaction [19]. Various types of fast neutron interactions are possible with carbon (diamond). The dominant fast neutron reaction with carbon atom is elastic scattering. However, the neutron inelastic scattering results in the production of 3α particles and absorption reactions produce light ions. Figure 2.1 shows the cross-section of neutron reaction with ^{12}C atom [20].

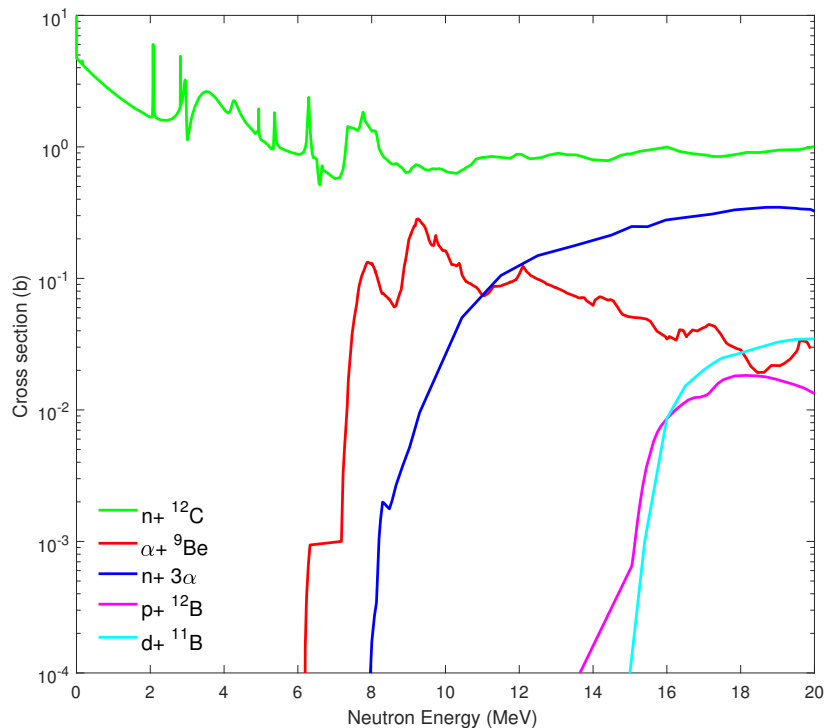


Figure 2.1: Cross-section of neutron interactions with carbon atom [20]. Green and blue cross-section stand for elastic and inelastic scattering, respectively. Other interactions represent absorption cross-section.

In elastic scattering, the total kinetic energy and momentum of the two colliding particles are conserved. Additionally, both colliding particles (neutron and carbon atom) reappear after interacting, but the kinetic energy redistributes between them [21]. The scattered neutron usually escapes the diamond detector whereas the recoil carbon atom stops within the diamond sensor due to the low range of such large atom [22]. Elastic scattering is the main reaction for detecting neutrons with energy lower than 6 MeV, and it shows a continuous spectrum of energy deposition because of the various energy depositions of recoil carbon atoms. Also, neutron scattering cross-section variation reflects differences in counting rate as shown in Figure 2.2.

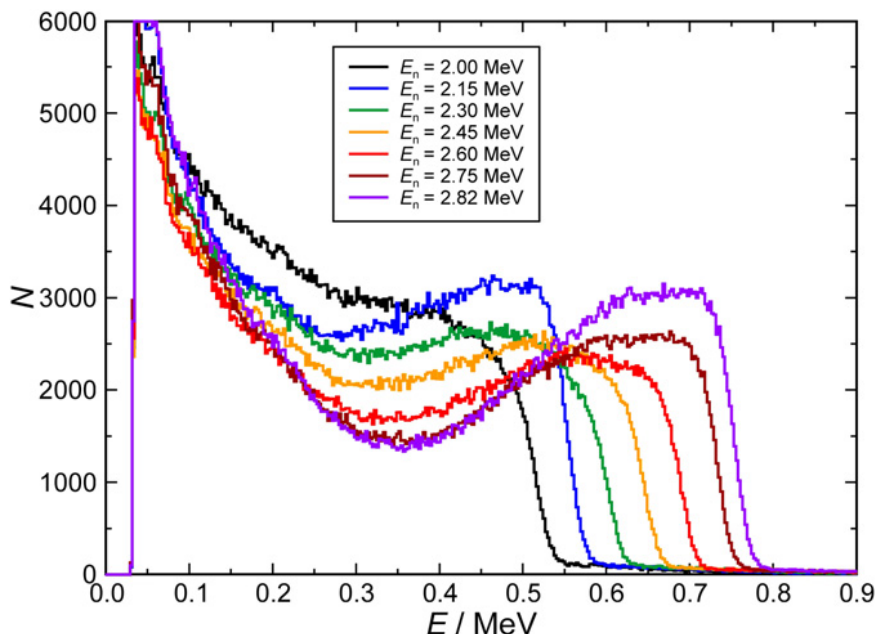


Figure 2.2: Energy deposition spectra of distinct neutron projectiles with SDD [22].

For neutron energies greater than 6.17 MeV, fast neutron interaction peaks start to appear in the pulse height spectrum since incident neutron exceeding interaction threshold energy for (n,α) absorption interactions. The main fast neutron reactions with the SDD are listed in Table 2.3 with reaction Q-values and thresholds [23]. Additionally, the secondary charged particles out of the fast neutron interactions have a lower range, and they usually deposit all of their energies within the SDD.

Table 2.3: Main fast neutron reaction with SDD [23].

Reaction	Q-value (MeV)	Threshold Energy (MeV)
$^{12}\text{C}(\text{n},\text{n}')^{12}\text{C}$	0	0
$^{12}\text{C}(\text{n},\alpha)^9\text{Be}$	-5.701	6.17
$^{12}\text{C}(\text{n},\text{n}')3\alpha$	-7.275	7.886
$^{12}\text{C}(\text{n},\text{p})^{12}\text{B}$	-12.587	13.644
$^{12}\text{C}(\text{n},\text{d})^{11}\text{B}$	-13.732	14.886
$^{12}\text{C}(\text{n},\text{t})^{10}\text{B}$	-18.929	20.52

Researchers have studied the capability of using diamond detectors in fast neutron spectroscopy [23–25]. Pillon *et al.* emphasized the capacity of an SDD as a fast neutron energy spectrometer. Basically, the SDD was exposed to beams of multiple mono-energetic neutrons. Neutron beam induced inelastic and absorption interactions that shows sharp peaks in pulse height spectrum, as provided in Figure 2.3. The 20.5 MeV neutron beam shows all fast neutron interactions with diamond except the (n,t) interaction since the neutron energy is lower than the interaction threshold. Moreover, for the measured peak of $^{12}\text{C}(\text{n},\alpha)^9\text{Be}$ interaction, the SDD reached a good intrinsic resolution (FWHM=56 keV). Moreover, the produced α particles has the range of 62 μm [23].

Similarly, Rebai *et al.* demonstrated the eligibility of an SDD with the ToF technique to determine quasi mono-energetic neutrons up to the energy of 40 MeV. The source was a spallation neutron spectrum in the nTOF CERN facility, and the ToF technique was used to characterize each neutron energy spectrum. After pre-amplification, all coinciding events between SDD output signals and pico-second CERN synchrotron were stored in a fast digitizer (1 GHz sampling rate) and then post-processed offline. Pulse height spectra of the SDD show good agreement with the Pillon *et al.* measurements [23, 24].

Furthermore, an SDD was exposed to high neutron fluxes out of the tokamak fusion reactor. Both (D,D) and (D,T) reaction neutrons were detected in the SDD with good resolution ($\approx 2\%$ at 5 MeV). Additionally, due to the SDD's fast signals, the SDD recorded

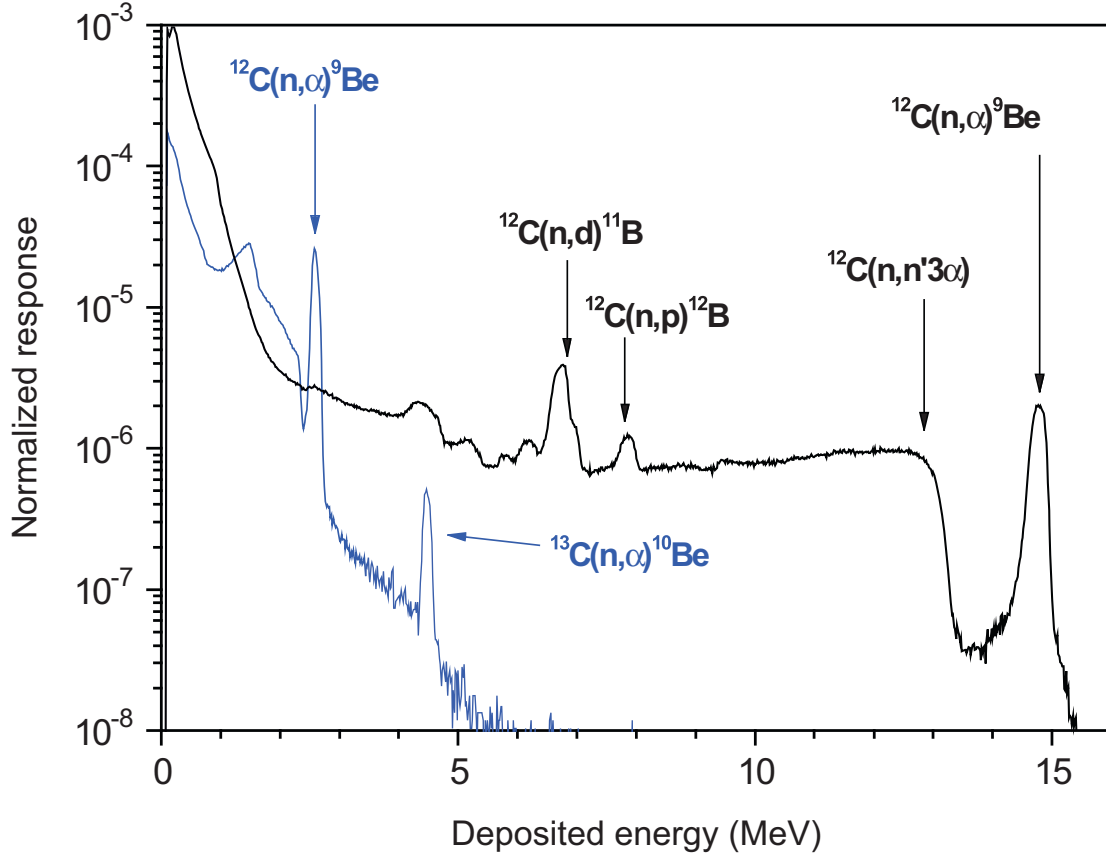


Figure 2.3: Pulse height spectrum of two neutron projectiles ,20.5 MeV (black) and 8.3 MeV(blue), with SDD [23].

a much higher counting rate compared to the NE213 liquid scintillator. This study proved the capability and reliability of SDDs in harsh radiation environments [25].

2.2.2 Charged Particles

Charged particles interact with any material traveling through via Coulomb interactions with nuclei, and atoms orbital electrons. The main energy loss mechanisms of the travelling charged particle are excitation and ionization. Excitation occurs when an electron, while still bound to the nucleus, transfers from its orbit to occupy one of a higher energy. Ionization, on the other hand, occurs when an electron gains enough energy to escape the nucleus, leaving behind a positive ion [26]. Energy loss due to excitation and ionization is estimated by the Bethe-Bloch relation (stopping power equation), as described in Equation 2.1 [27].

$$\left\langle -\frac{dE}{dx} \right\rangle = 4\pi r_0^2 z^2 \frac{mc^2}{\beta^2} NZ \left[\ln\left(\frac{2mc^2}{I} \beta^2 \gamma^2\right) - \beta^2 \right] \quad (2.1)$$

where

r_0 = classical electron radius = 2.818×10^{-15} m

z = charged number of the incident ion.

c = speed of light = $2.997930 \times 10^8 \frac{m}{s}$

mc^2 = electron rest mass = 0.511 MeV

β = beta Lorentz factor = $\frac{v}{c}$

γ = gamma Lorentz factor = $\frac{1}{\sqrt{1-\beta^2}}$

N = number of atoms in the target material per unit volume ($\#/cm^3$)

Z = material atomic number

I = mean excitation energy (eV)

Pomskey *et al.* used an SDD to measure the spectrum of α particles emitted by a ^{241}Am source. The α particles stopes within few μm . The SDD presented good energy resolution because of its high carrier lifetime and charge collection efficiency. To evaluate SDD energy resolution, a commercial silicon (Si) detector measured the α source as well. Both detectors used same electronics and measured for equal amounts of time. The SDD exhibited not only comparable resolution but also a higher count rate, as provided in Figure 2.4 [28].

In the experiment, the SDD showed high stability, with no observable polarization during the experiment (48 hours). Polarization effect causes output signal degradation over time because of the build-up of space charge [17]. Furthermore, radiation hardness and fast rise signals make an SDD a good candidate for high-energy physics experiments [28].

2.2.2.1 Energetic Ion Measurements

Radiation hardness and fast timing capability are two essential properties that make an SDD an alternative candidate for current silicon detectors in high-energy physics tracking experiments [29]. One advantage of diamond sensor over silicon detector that there is no need of cooling down due to the high band gap. An immense number of studies by the RD42

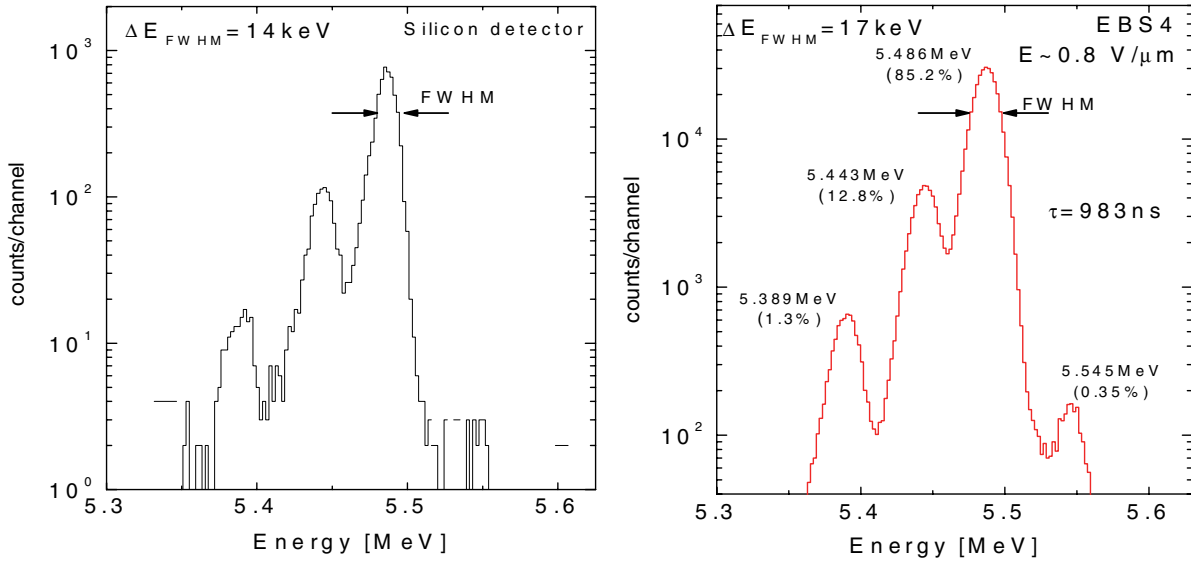


Figure 2.4: ^{241}Am α source spectroscopy using (left) Si detector and (right) SDD [28].

collaboration have been conducted on the feasibility of using diamond particle tracking sensors in high-rate energetic ion accelerators [30]. In fact, CERN has already used diamond sensors in a Large Hardon Collider (LHC) experiment [31]. The first pixelated SDD was characterized in a high-flux experiment ($\approx 10^{15}$ particles/cm²) with 100 GeV π particles bombardment. The SDD demonstrated high detection efficiency ($\approx 99.9\%$), with no recorded polarization [32].

In addition, a new pixelated diamond sensor, the Diamond Beam Monitor (DBM), was used in the ATLAS experiment for luminosity monitoring, in which the DBM counted the particles produced from an energetic collision in the LHC [33]. Recently, the RD42 collaboration succeeded in creating a 3D-diamond detector with low voltage bias and even higher charge collection efficiency to be used in future heavy-ion experiments [34]. In summary, due to its many advantages, the SDD shows excellent reliability in high-energy physics tracking experiments; however, no study shows the feasibility of the SDD as a particle identifier in such experiments.

2.3 Time-of-Flight Spectrometer

The time-of-flight (ToF) concept for mass spectrometers was first proposed and designed by McLaren and Wiley in 1955 [35]. Particle flight time reflects the energy of the detected particle; thus, fast neutrons arrive in the detector before epithermal neutrons, whereas fast and epithermal neutrons ranges are (1-20 MeV) and (0.025-0.4 eV), respectively [36]. Additionally, because of the high velocity of photons, ToF technique can differentiate between photons and neutrons. Using ToF to distinguish between γ rays and neutron particles was first addressed by Smith *et al.*. Detected neutron particles and γ rays emitted by a ^{252}Cf source were plotted as a function of time as shown in Figure 2.5a [37]. Moreover, as provided in Figure 2.5b, a reconstructed spectrum of spontaneous fission neutrons of the ^{252}Cf source was plotted with acceptable accuracy.

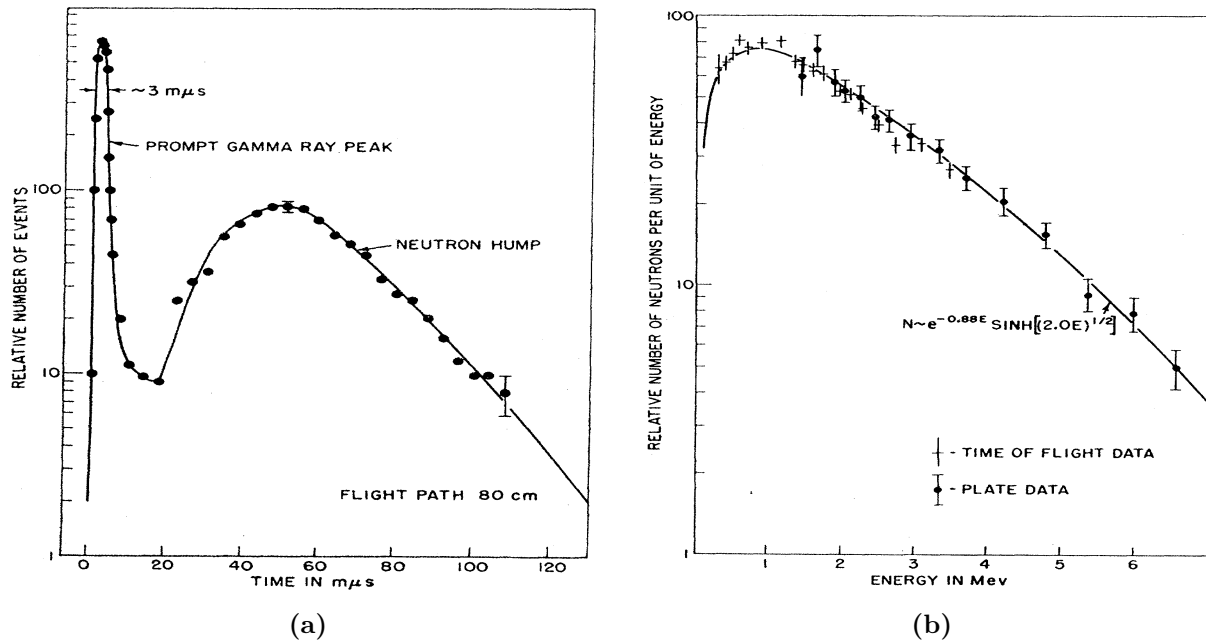


Figure 2.5: ^{252}Cf source measurements using ToF technique. (a) ToF distribution for γ rays and neutrons. (b) Spontaneous neutron fission spectrum [37].

^{252}Cf neutron energies were reconstructed based on simple kinematics equations to convert ToF into energy. After identifying a neutron particle from ToF distribution graph, the neutrons velocity was calculated based on the ToF measurement in a previously known path distance (d) as follows,

$$v = \frac{d}{ToF} \quad (2.2)$$

The reconstructed neutron kinetic energy (non-relativistically) is approximated by,

$$E_n = \frac{1}{2}m_nv^2 \quad (2.3)$$

where E is the neutron energy (MeV) and m_n is the neutron rest mass (939.565 MeV).

As stated by Turner *et al.* [38], Equation 2.3 represents a neutron with energy equal to or less than 10 MeV. However, relativistic kinematics was utilized for higher energies to determine neutron energy, as described in Equation 2.4,

$$E_n = (\gamma - 1) * m_n \quad (2.4)$$

where γ is a Lorentz factor and is defined as,

$$\gamma^2 = \frac{1}{(1 - \beta^2)} = \frac{1}{\left(1 - \frac{v^2}{c^2}\right)} \quad (2.5)$$

Additionally, the ToF technique was used to identify recoil nuclei as well. Bowman *et al.* distinguished between light and heavy fission fragments from the spontaneous fission of the ^{252}Cf source. The fission neutron multiplicity was defined and counted; however, identification of different nuclei, using ToF data, in each group was not achieved [39].

2.3.1 Neutron Scatter Camera

The neutron scatter camera (NSC) was first proposed by Mascarenhas *et al.* to locate SNM sources for homeland security [40]. The SNM source spectrum was identified based on the reconstructed fast fission neutrons. A source spectrum was plotted using the ToF of neutron double-scattering events. The NSC consists of two parallel panels, each with 4 liquid scintillators. Since the SNM sources emitted photons beside neutron particles, the pulse shaping discrimination (PSD) processing method was used for (n- γ) discrimination [41].

The neutron source origin was located by creating probability cones of scattered neutrons, as provided in Figure 2.6.

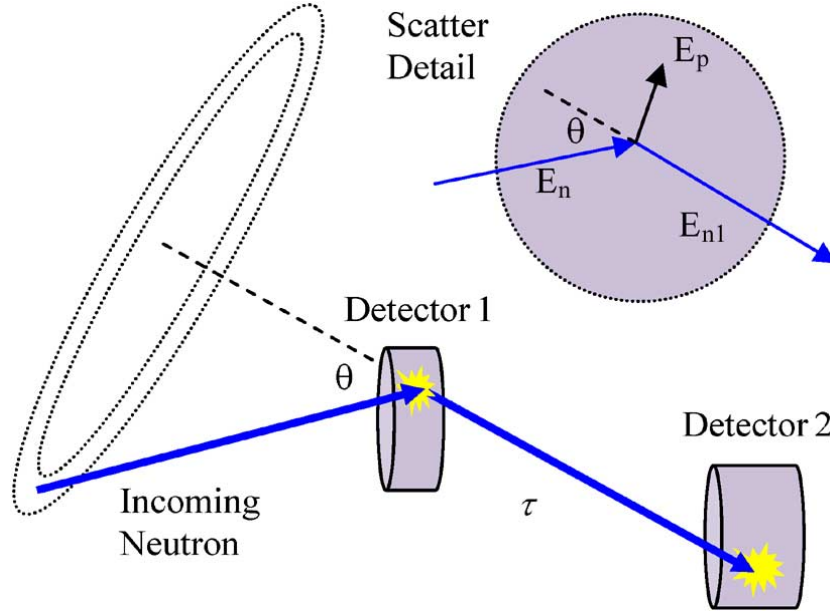


Figure 2.6: Back-projection scheme for a double neutron scattered event [42].

For spectral analysis, the incident neutron energy E_n was calculated based on the deposited energy of the recoil proton E_p and the ToF between two scintillation detectors. The recoil proton energy was measured using scattering angle (θ) as follows,

$$E_p = E_{n1} \tan(\theta)^2 \quad (2.6)$$

Next, the scattered neutron energy was calculated by Equation 2.7,

$$E_{n1} = \frac{m_n}{2} \left(\frac{d}{ToF} \right)^2 \quad (2.7)$$

Then, the incident neutron energy was reconstructed using the conversion of energy, as described in Equation 2.8,

$$E_n = E_p + E_{n1} \quad (2.8)$$

With a more advanced NSC, Mascarenhas *et al.* successfully pinpointed a ^{252}Cf source placed 30 meters away from the NSC [43], as shown in Figure 2.7. The detection threshold was set as 70 keVee to prevent noises. 120° angle view was recorded for the NSC. The system indicated an angular resolution (1σ) of 12° and the capability to reconstruct neutron energy in the range of 0.5-10 MeV.

Detection efficiency was improved by increasing the number of liquid scintillator detectors (EJ-309) per each panel from 9 to 16. In this improved system, the separation distance between the two panels was adjustable (13-127 cm), the lowest distance (13 cm) achieved the highest detection efficiency while the separation distance of 127 cm provided the best angular resolution. Using 40 cm spacing between the two panels, the energy resolution of a reconstructed mono-energetic neutron (2.5 MeV) was recorded as 10-15% (non-Gaussian peak shape). The high thickness of the detectors (5 cm and 13 cm in front and back panels, respectively) resulted in reducing the energy resolution of the system. In addition, the increased number of NSC elements yielded higher angular resolution ($\approx 10^\circ$) than in previous NSC design [42, 44, 45]. However, the large size and poor energy resolution of organic liquid scintillators remain unresolved drawbacks for the NSC systems.

Recently, the single-volume scatter camera made of pillars of plastic scintillators (SVSC-PiPS) system was simulated to use as an NSC device to locate neutron sources. The SVSC-PiPS (as shown in Figure 2.8) is composed of segmented pillars of plastic scintillators with reflected channels. To increase light collection efficiency, each plastic scintillator was separated by a 1-mm air gap [46].

The simulation located a ^{252}Cf isotropic source with 10^8 particle history as shown in Figure 2.8. Using 1 MeV as the energy threshold for each detector, the angular resolution (1σ) of the polar and azimuth angles, were calculated as 23.93° and 17.77° , respectively, for a ^{252}Cf source located at the center of the axis ($0^\circ, 0^\circ$) and 1 meter away from the detection system. The SVSC-PiPS detection efficiency increased by an order of magnitude greater than that of the NSC [46]. Still, the ability of SVSC-PiPS to reconstruct the neutron spectrum was not examined, and the construction of the SVSC-PiPS system is still in process.

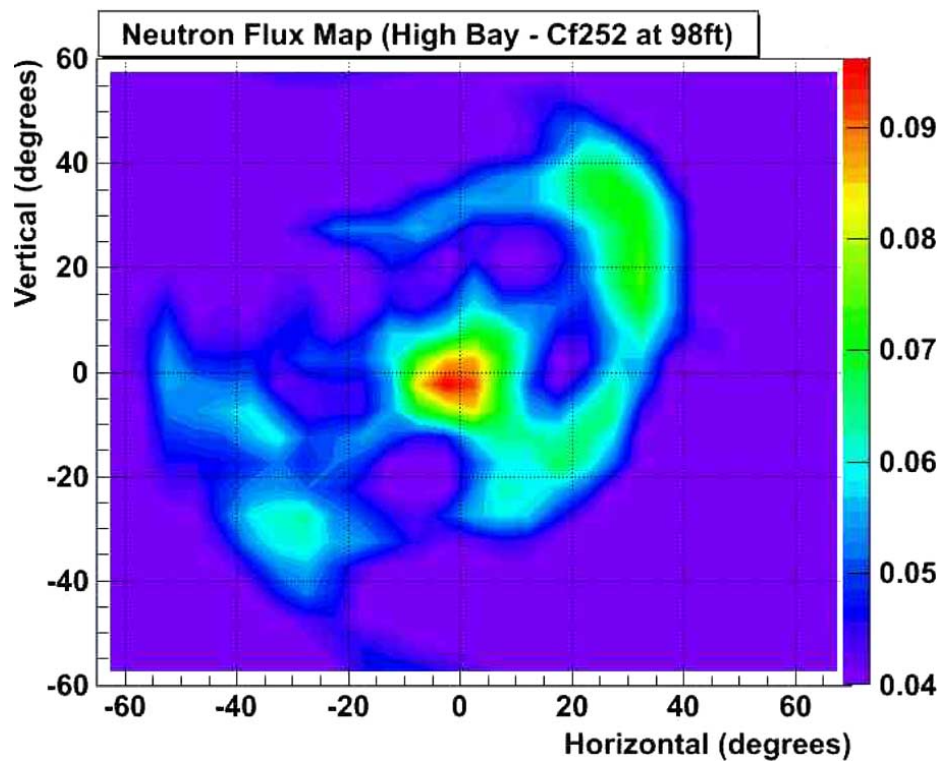


Figure 2.7: NSC back-projected image of ^{252}Cf source placed 30 m away [43].

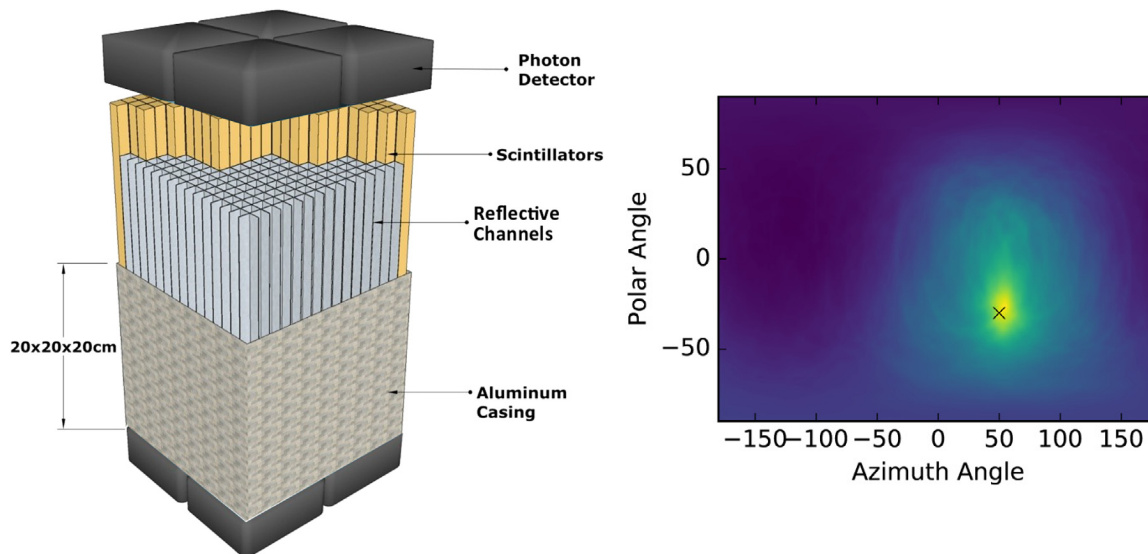


Figure 2.8: (left) Schematic of an SVSC-PiPS system. (right) Reconstructed image for a ^{252}Cf source located 1m from the center of detection system; x indicates the true source position [46].

Chapter 3

Diamond-based Neutron Scatter Camera

3.1 Introduction

The increased threat of the proliferation of radioactive materials requires more advanced detection techniques to locate and define SNM sources. Although the NSC technique shows a high validation in locating SNM sources, the need for large scintillator detectors makes the transportation of NSC instruments impractical. Additionally, the poor energy resolution of the scintillator detectors points to the need to investigate an alternative compact NSC system. [40, 47].

The DNSC was built to use the advantages of diamond detectors characteristics; namely, extremely fast rise signals and radiation hardness [3]. The DNSC concept was to operate in harsh radiation environments with high reliability such as in fusion reactors, which generate highly intense neutron flux, or in future space missions, where small size and light weight are extremely valuable. The system was designed for both spectral analysis and localizing neutron sources based on a large set of Monte Carlo simulations. The DNSC was investigated experimentally as well to proof the diamond NSC concept and validate the simulation results.

3.2 Monte Carlo Simulation

Los Alamos National Laboratory software, the Monte Carlo N-Particles (MCNP) simulation, was chosen for this work. MCNP is a global code used for particle transport applications. Neutron, photon, and electron particles are simulated for various applications such as detector design [48]. Tallies are considered the main method of printing MCNP simulation results. However, the lack of presenting precise interaction times leads to activating a Particle TRACk (PTRAC) card instead.

The PTRAC card outputs an immense size of file of the complete history of primary and secondary particles. The files include detailed information of each interaction such as particle coordinates, particle type, energy, and interaction times. Large output file size is considered one of the drawbacks of the PTRAC card. To reduce the size of the generated files, a filter card was implemented by including only interest detector cell numbers and collision event types. Parallel processing of MCNP codes with different sequences of particle history numbers was performed to gain much data in a shorter period of time.

The potential of a DNSC depends on several parameters: the number of diamond detectors or pixels per diamond, the relative orientation between the diamond detectors, the distances between them, the size of each diamond detector, the minimum energy deposited, and the timing performance of each detector. In this dissertation, each of these parameters was considered for mapping out device performance as a function of system design parameters.

A diamond detector was simulated as ^{12}C material because an SSD contains a very high percentage of ^{12}C isotopes [6]. The most recent library of evaluated nuclear reaction data (ENDF/B-VII.1) from the National Nuclear Data Center (NNDC) was implemented in the simulation [49]. All simulated diamond detectors were surrounded by natural air to mimic real experiment conditions [50].

The MCNP6 treated neutron capture in either implicit or analog capture. Analog capture was used in this study instead of implicit capture because the latter is recommended to use only in highly absorbing media [51]. Multiple mono-energetic sources (0.25-14 MeV) were modeled as point sources to investigate the best scattering angles that demonstrated

the best energy resolution while also maintaining good detection efficiency. It was found that scattering angle has a proportional relationship to energy deposited in the diamond detector. Once the optimum angle was defined, the separation distance between the diamond detectors were chosen based on the accuracy of the reconstructed neutron energy of 1 MeV. The incident neutron energy was chosen due to the high neutron cross-section with the ^{12}C atom.

Once DNSC geometrical designs were obtained based on mono-energetic neutrons, ^{252}Cf and $^{239}\text{Pu-Be}$ sources were simulated as neutron sources. The ^{252}Cf source was generated using the built-in card option in MCNP6. ^{252}Cf is a spontaneous fission source that generates high yields of neutron and γ -rays. The fission neutrons exhibited the typical Watt fission distribution, as described in the following equation [52],

$$p(E) = C \exp\left[\frac{-E}{a}\right] \sinh(bE)^{0.5} \quad (3.1)$$

where a and b are parameters and have the values 1.3 and 2.948 in default, respectively. However, the MCNP manual provided the parameters values of the ^{252}Cf spontaneous fission source: a=1.18 and b=1.03419 [48]. The $^{239}\text{Pu-Be}$ neutron source, on the other hand, shows low yield of γ -rays but exhibits several spectral features of neutron particles and extends as high as 11 MeV [48, 53]. The $^{239}\text{Pu-Be}$ neutron source spectrum was obtained from Reference [53]. Neutron source spectra were plotted in Figure 3.1.

Two DNSC setups were implemented through MCNP: a two-diamond array system and a diamond-array system. The two-diamond array system was constructed to evaluate the capability of spectroscopy measurements. Once the optimum system of geometrical orientation was defined for a given threshold and timing uncertainty, ^{252}Cf and $^{239}\text{Pu-Be}$ neutron sources were used to evaluate the potential of NSC. Both neutron sources were modeled as point sources to reduce machine runtime. Additionally, the sources were simulated far enough away from the two-diamond array to enable appropriate assumptions of an incident plane wave of neutrons.

The main goal of diamond array implementation was to reconstruct high resolution neutron images using the back-projection technique. The diamond arrangements were

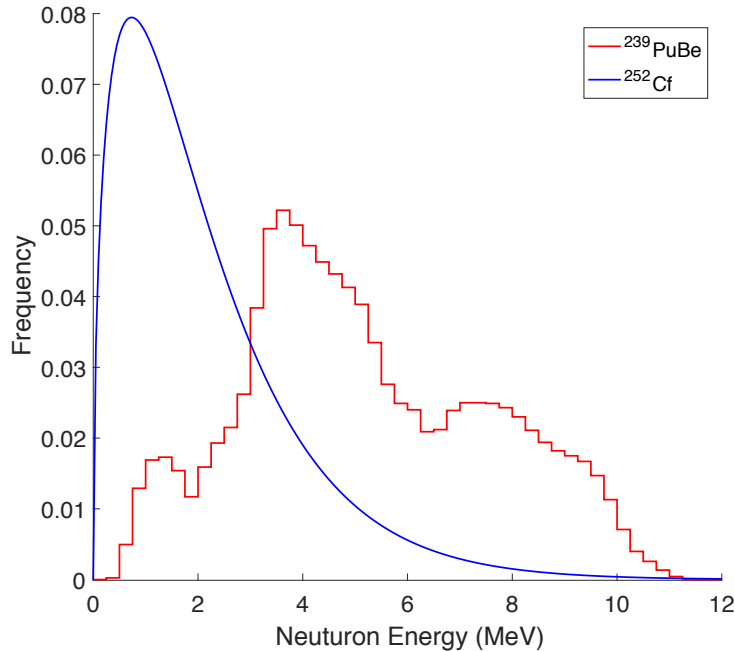


Figure 3.1: ^{252}Cf and $^{239}\text{Pu-Be}$ neutron sources spectra.

determined based on such factors as detection efficiency, spectral analysis, and source localization. The diamond-array system included numerous pixelated diamond detectors distributed in two arrays. The neutron sources were modeled as cone sources instead of isotropic sources because the latter required considerable simulation runtime. Moreover, the cone angle was implemented to cover the whole array of diamonds to allow simulated neutrons to interact with each pixel. Examining different orientations with immense numbers of pixels led to the need for creating a C++ code capable of building MCNP codes based on user input of system geometry specifications. For instance, the code was built based on a class function called Pixel. The class algorithm read the following user input parameters: diamond size (width and thickness), number of diamonds per array, separation distance between diamonds in each array, and array separation distance. Then, the same class printed the MCNP code in an output file. The first diamond array, located in the center of the axis coordinates (0,0,0). Additionally, the output file included all cards except source specifications, which were typed manually after running the C++ code.

The DNSC used double-scattering interactions to reconstruct a neutron source spectrum. Due to the limited growth capability of large volume diamond substrates, the angular

distribution of secondary neutrons played an important role in the DNSC design (see Figure 3.2).

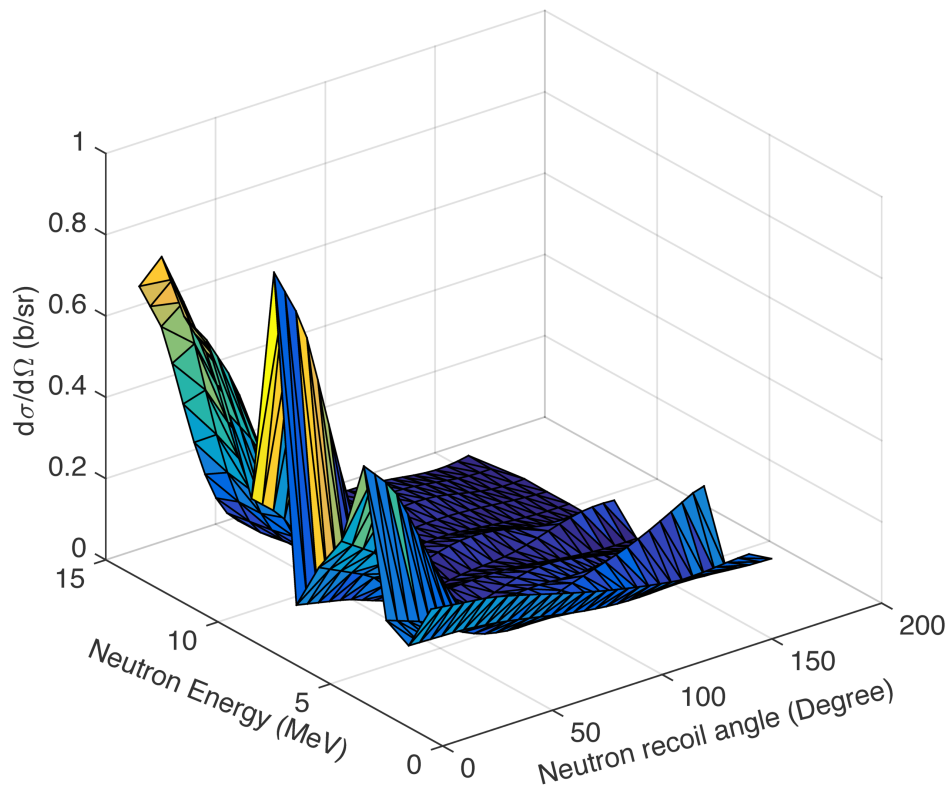


Figure 3.2: Relationship between the angular distribution, neutron recoil angle in CM, and neutron energy. The plot was generated from CENDL-3.1 ENDF neutron library [20].

After running MCNP codes for a specific number of neutron particles (i.e. $1 \cdot 10^{11}$), post-processing codes were built and conducted to extract and present the simulation results.

3.3 Post-Processing Algorithm

DNSC system design parameters were optimized through a series of MCNP6 simulations. PTRAC output files were processed through C++ code to implement all double-scattered events. To meet kinematics equation requirements (conservation of energy), the first interaction in any double-scattering event had to be elastic scattering. However, the second interaction could have been any type of interaction because it was needed for measuring ToF only. The post-processing code printed the following in an output file: incident neutron

energy, neutron-scattered energy, coordinates, and time occurring for both events. Only timing and recoil carbon atom energy were required to reconstruct the neutron source spectrum in both DNSC setups. However, other parameters were used to reconstruct the exact spectrum for comparison purposes with DNSC measurements. The flow chart in Figure 3.4 summarizes the process of C++ code for the DNSC systems.

3.3.1 Two-Diamond Array

The C++ code output files were processed through a Matlab code to build the incident neutron spectra. Using relativistic kinematics, the incident neutron energy, E_n , was calculated using Equation 3.2,

$$E_n = \frac{E'_n * (A^2 + 1)}{\left[\cos \vartheta - \sqrt{A^2 + \sin^2 \vartheta} \right]^2} \quad (3.2)$$

where ϑ is the neutron-scattered angle [54]. Based on Equation 3.2, the energy of the recoil atom was not required to reconstruct the scattered neutron like in all current NSC systems. However, an energy deposition threshold (10 keV) was chosen to investigate the feasibility of the reconstructed spectra using a two-diamond array in an experimental environment. The scattered neutron, E'_n , energy was calculated, as described before in Equation 2.4. A histogram was built of the reconstructed incident neutron source. The histogram bins were defined accordingly to decrease the uncertainties in each bin. Once the neutron energy spectrum was constructed, it had to be corrected for the small and changing detection efficiency of thin diamond detectors.

The final step in source spectrum reconstruction was correcting for the neutron cross-section of carbon (i.e., the detection efficiency). Because diamonds have 12 nucleons, as the energy of the neutron increases, the higher order quantum number L in the Legendre Polynomials results in a non-flat differential scattering cross-section and must be considered in addition to the integrated differential scattering cross-section as a function of energy (i.e., the neutron detection efficiency as a function of energy) [17]. With appropriate calibration of the DNSC, the measured response was corrected to accurately represent the incident neutron

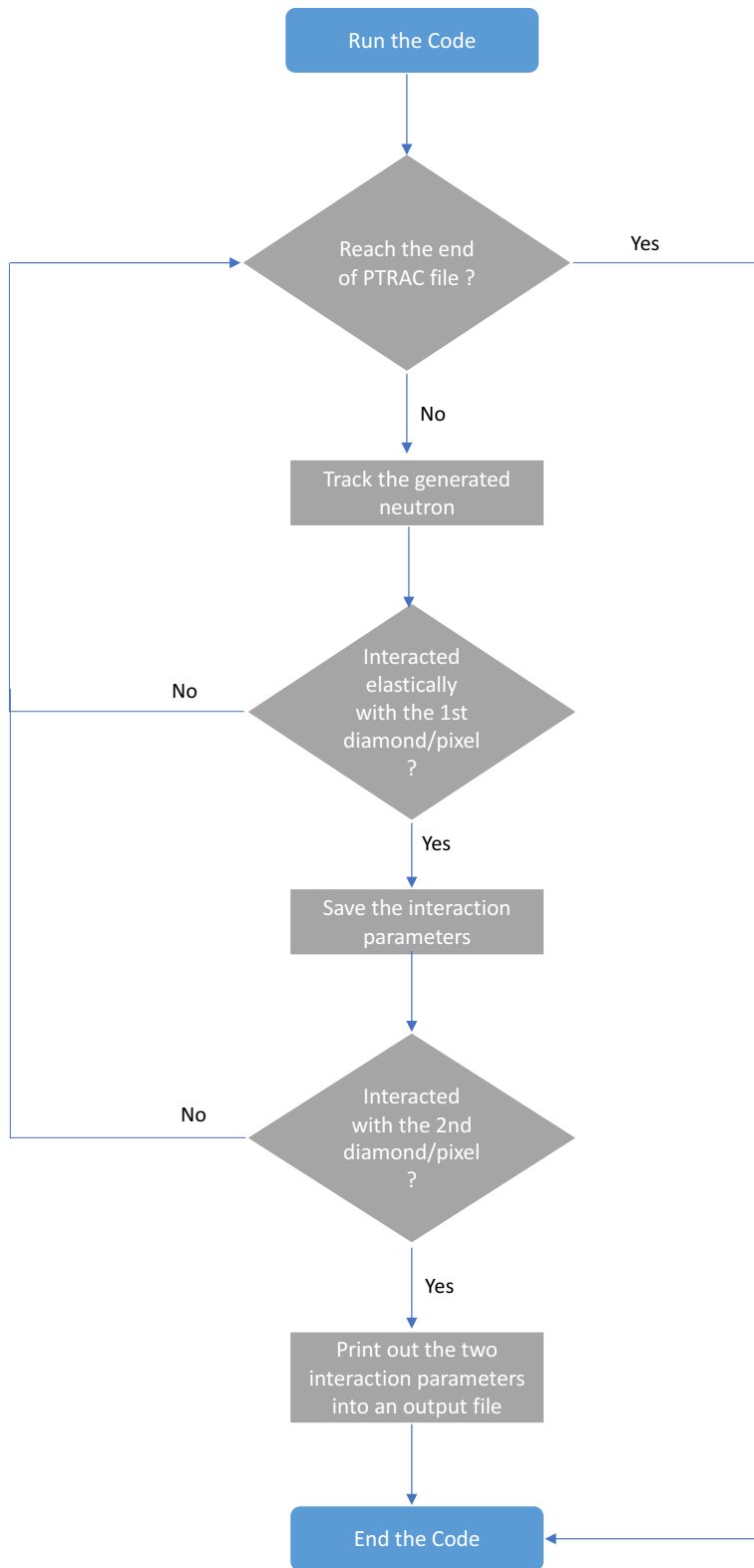


Figure 3.3: The flowchart of C++ code to extract double-scattering events from DNSC PTRAC output files.

source spectrum. Finally, both modified and unmodified DNSC spectra were plotted along with the neutron source spectrum.

3.3.2 Diamond Array System

3.3.2.1 Spectral Analysis

In contrast to the two-diamond array system, the energy deposited from the carbon recoil atom in the first pixel must be defined to build the neutron spectrum because the scattering angle has huge variation in this diamond array system. For any double-scattered neutron interaction, the energy of the scattered neutron was calculated based on Equation 2.4, while the incident neutron energy, E_n , was calculated using Equation 3.3,

$$E_n = E'_n + E_c \quad (3.3)$$

where E_c is the energy of the recoil carbon atom measured in the first detector [2].

3.3.2.2 Source Localization

Based on scattered and incident neutron energies defined in Equations 2.4 and 3.3, the scattered angle was calculated using Equation 3.4 [54].

$$\cos \theta = \frac{1}{2} \left[(A + 1) \sqrt{\frac{E'_n}{E_n}} - (A - 1) \sqrt{\frac{E_n}{E'_n}} \right] \quad (3.4)$$

Thus, arrival direction located the source via the back-projection cone, and several interactions were used to pinpoint the location of the source. Nevertheless, the projection cone angle had uncertainty, a product of uncertainties associated with timing and energy deposition [55]. The radius of the cone was calculated using the scattering angle of the first diamond detector and the distance to the image plane, as shown in Figure 3.4.

The post-processing code created a 2D image plane. The image was coded as a 2D matrix consisted of 10000 cells, each with a value of zero. The built cone increment the assigned cells. The image plane was represented in x and z axis. However, the 3D coordinates had to be defined for the image. The y-component of the image plane represented the distance

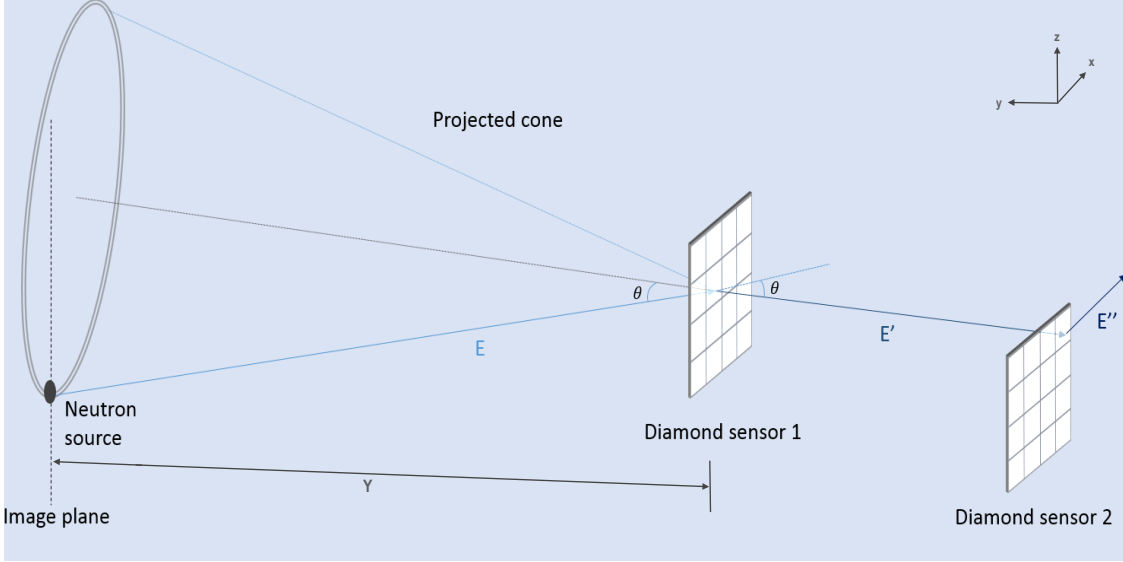


Figure 3.4: Illustration of the back-projection technique with two pixelated diamonds.

to the first array of the diamond array system (Y). To achieve the highest resolution, the Y -value of the image plane had to match the source y -component to define the real radius from the cone center to the neutron source. A color-bar was included as well in the generated image to determine the precise source position.

3.4 Uncertainty Calculation

For ToF between any two diamond detectors, much uncertainty occurs; namely, the uncertainties in the distance, angle between the two detectors/pixels, and timing associated with the involved detectors and electronic devices. The uncertainty in the distance can be minimized, but the uncertainty in the angle is a property of the size of the two detectors and the separation distance, which increased as the distance between the two detectors decreased. The uncertainty in the timing was dictated by the speed of the diamond detectors and processing electronics. Literature [28] has shown that the timing between two diamond detectors using MIPs is on the order of tens of picoseconds. Therefore, the system performance is expected to be dominated by the uncertainty of the angle between the two diamond detectors. Based on Cetiner M. [56], the relativistic energy resolution for ToF measurements was calculated by Equation 3.5,

$$\begin{aligned}
FWHM = \Gamma_d = \Delta E &= E + Mc^2 \frac{\beta^2}{1 - \beta^2} \sqrt{\left[\frac{\Delta L}{L}\right]^2 + \left[\frac{\Delta t}{t}\right]^2} \\
&= E + Mc^2 \frac{\beta^2}{1 - \beta^2} \sqrt{[\delta L]^2 + [\delta t]^2} \quad (3.5)
\end{aligned}$$

where δt and δL are relative uncertainties of ToF and scattered path length, respectively.

Equation 3.6 described timing uncertainties for both detectors.

$$\delta t = \sqrt{2 * \delta t_{walk}^2 + 2 * \delta t_{jitter}^2 + \delta t_{depth1}^2 + \delta t_{depth2}^2 + \delta t_{angle}^2} \quad (3.6)$$

The walk and jitter were caused by the uncertainty of the signals amplitude when it reached the discrimination threshold. Figure 3.5 explains the timing walk and jitter of the leading-edge timing discrimination (LED) mode.

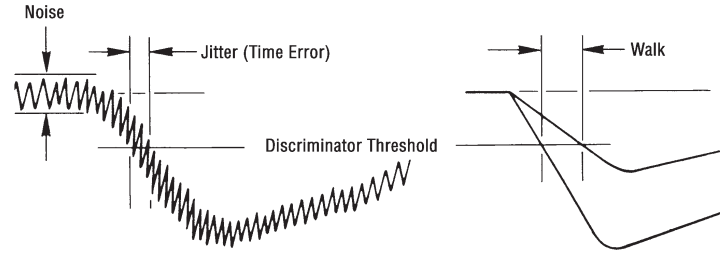


Figure 3.5: Walk and jitter uncertainties in leading-edge discriminator mode [57].

The Constant Fraction Discrimination (CFD), on the other hand, generated less walk and jitter uncertainties because the triggering event occurred independent of the analog signal amplitude [58]. Equation 3.7 represents the jitter timing based on rise signals of both diamond detector and amplifier,

$$t_{jitter} = \sigma_{jitter} = \frac{\sqrt{t_{rs}}}{V_0} \sqrt{\frac{t_{rs}}{t_{ra}} + \frac{t_{ra}}{t_{rs}}} \quad (3.7)$$

where t_{rs} and V_0 is the detector rise time and peak amplitude of detection signal. The amplifier rise time is represented by t_{ra} [56].

The jitter timing of the diamond detector for a fiber-optic cable was demonstrated as 12 picoseconds based on Reference [10]. Differences in rise times of the detector and amplitude

of the input signal caused time walk to the DNSC. In other words, higher amplitude input signals reached the LED energy threshold faster than signals with a lower amplitude [56]. According to Reference [59], the time walk equaled approximately 12 picoseconds for the detection system with fast preamplifiers.

Depth and angular uncertainties played a substantial role in DNSC timing. Both depth and angular uncertainties were found by defining the difference between the interaction locations of the scattered neutron and average angles and depths. One term (δt_{depth}) was used for depths and angular and neutron flight path length uncertainties because all of them were functions of interaction locations in the 3D coordinate system.

Due to the statistical process of electron-hole productions within the diamond detector, the Fano factor was included to obtain the energy resolution of the detector. The FWHM of single diamond detector is given by Equation 3.8 [21],

$$\Gamma_f = 2\sqrt{(2\ln 2)FE_d\omega} \quad (3.8)$$

where F is the Fano factor and had the theoretical value of 0.08 for diamond [60]. Additionally, E_d and ω were the energy deposition and energy required to create an electron-hole pair, respectively. Furthermore, the two-diamond array had only two detectors; thus,

$$\Gamma_{ft} = \sqrt{\Gamma_{f1}^2 + \Gamma_{f2}^2} \quad (3.9)$$

Consequently, the total FWHM of DNSC is described in Equation 3.10 [21],

$$\Gamma_t = \sqrt{\Gamma_d^2 + \Gamma_{ft}^2} \quad (3.10)$$

3.5 DNSC Efficiency and Resolution Properties

Various MCNP codes were modeled for several mono-energetic neutron sources to obtain and define the detection efficiency and energy resolution of the two-diamond array system. All simulated sources were modeled as mono-directional, where the first diamond facing the beam, to reduce the machine runtime. The detection system, as described in section 3.2,

consisted of two diamond detectors, the first detector was stationary and facing the neutron source while the second diamond was situated in two different positions according to the detected neutron energy. Each MCNP code was run with a mono-energetic neutron source and a specific number of simulated neutron particles (2×10^9) since they provide optimum number of neutron interactions within the DNSC. The modeled neutron sources had values from 0.25 MeV to 14 MeV. The post-processing codes were utilized to execute data from PTRAC output files and generate an informative figure of the two-diamond array NSC properties.

3.5.1 Detection Efficiency

Detection efficiency of DNSC is a function of system geometry (solid angle, detector thickness, separation distance, and scattered angle) and the intrinsic properties of diamond detectors (density and neutron cross-section). However, MCNP simulated the neutron interaction in the diamond detectors based on those factors; thus, the detection efficiency was determined as the number of double elastic scattering neutrons (N) recorded by the two-diamond array system divided by the total number of generated neutrons (2×10^9) [2, 21].

3.5.2 Energy Resolution

Energy resolution was calculated based on the width of the reconstructed neutron energy peak. The Matlab code defined the Full Width Half Maximum (FWHM) value of the peak based on its standard deviation, as shown in Figure 3.6.

Equation 3.11 and 3.12 used to obtain the energy resolution of the detection system for each neutron source,

$$Resolution(\%) = \frac{FWHM}{Average\ of\ the\ reconstructed\ neutron\ energy} * 100 \quad (3.11)$$

$$FWHM = 2.35 * \sigma \quad (3.12)$$

where σ is the standard deviation of the reconstructed peak.

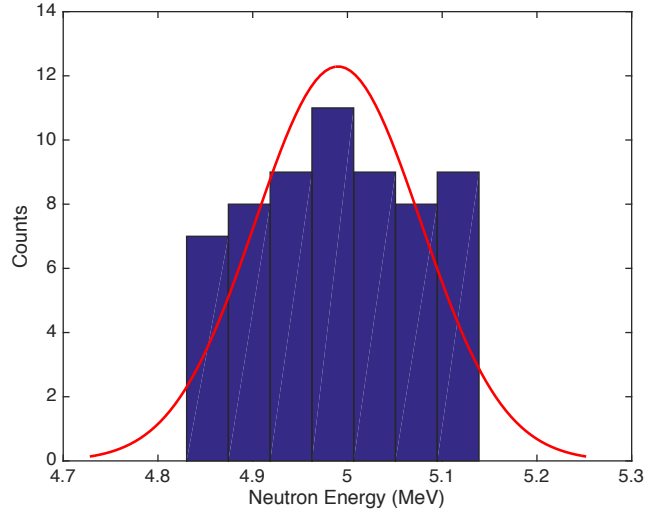


Figure 3.6: 5 MeV reconstructed peak using two-diamond array NSC.

3.6 Experimental Setup

To validate simulation results, an experimental evaluation of the two-diamond array was made. The experimental work had four main stages: preparing the SSDs, designing and fabricating the readout PCBs, mounting the SDDs with PCBs to the aluminum enclosures, and performing the experiment.

Because of the scratchy surface of the old electroplates, the old metallization contacts gold (Au)/chromium (Cr) were removed, and a new Au/Cr contact were applied. The following process summarizes the process: SDDs were boiled in Aqua Regia ($\text{HCl}:\text{HNO}_3$) (3:1) for forty-five minutes to strip the gold layer from the contacts. Next, a chromium etchant solution was applied for ten minutes to remove the chromium layer. Once the SDDs were free of contact, they were rinsed thoroughly with deionized water. A sputtering machine was used to sputter the new metallization contact to both surfaces of the SDDs. The new diamond contacts had a thickness of 100 nm and 50 nm for the chromium and gold layers, respectively. Furthermore, the SDDs were thermally annealed for 20 minutes in argon gas, heated to 600 °C, to acquire better Ohmic contact properties [17, 61].

Altium software was utilized to design the readout PCB, as shown in Figure 3.7. The PCB contained a diamond placeholder in the middle. As seen in the layout, a hole beneath the diamond was designed to reduce scattering neutrons in the PCB and, consequently, to

increase detection efficiency. A metal pad was included in the design to wire-bond the SDD to the PCB. The design layout was sent to SunStone company to fabricate two boards.

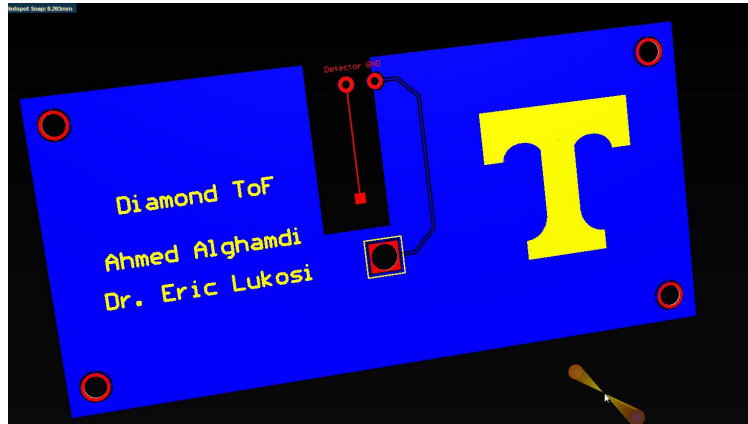


Figure 3.7: Screen shot of the designed PCB board in the Altium software.

Sliver paste was applied beneath the SDDs to hold them in the PCBs. Afterwards, a wedge bonder (Kulicke Soffa 4523D) was utilized to connect the SDDs to the boards using gold wire ($\approx 25 \mu\text{m}$). However, the wire was bonded to the board for only the first SDD due to the low electroplates layer thickness. Consequently, the wire was held with a tiny amount of silver paste applied to the top of the SDD.

Each diamond detector was contained within its own electrical housing, and each was mounted onto an aluminum extrusion frame, as shown in Figure 3.8. The frame allowed control of the relative orientation between the two diamond detectors. Since the enclosures were thick enough to increase the number of scattered neutrons, both boxes front and rear sides were cut through, and aluminum foil was used to cover cutting areas.

Besides the SSDs, two Cividec C6 fast amplifiers and a CAEN digitizer V5730 were used to capture the ToF of the double interaction events, as shown in Figure 3.9. The fast-shaping amplifier produced a fast signal with a Gaussian shape (FWHM=10ns). The digitizer had a fast sampling (500 MHz) rate with useful GUI interface. Compass software was conducted to run the digitizer in a coincidence mode and record all events within a specific timing window. The generated files included the time stamp in picoseconds, long gate, short gate, and event flag. Figure 3.10 displays the different parameters of the acquisition window.

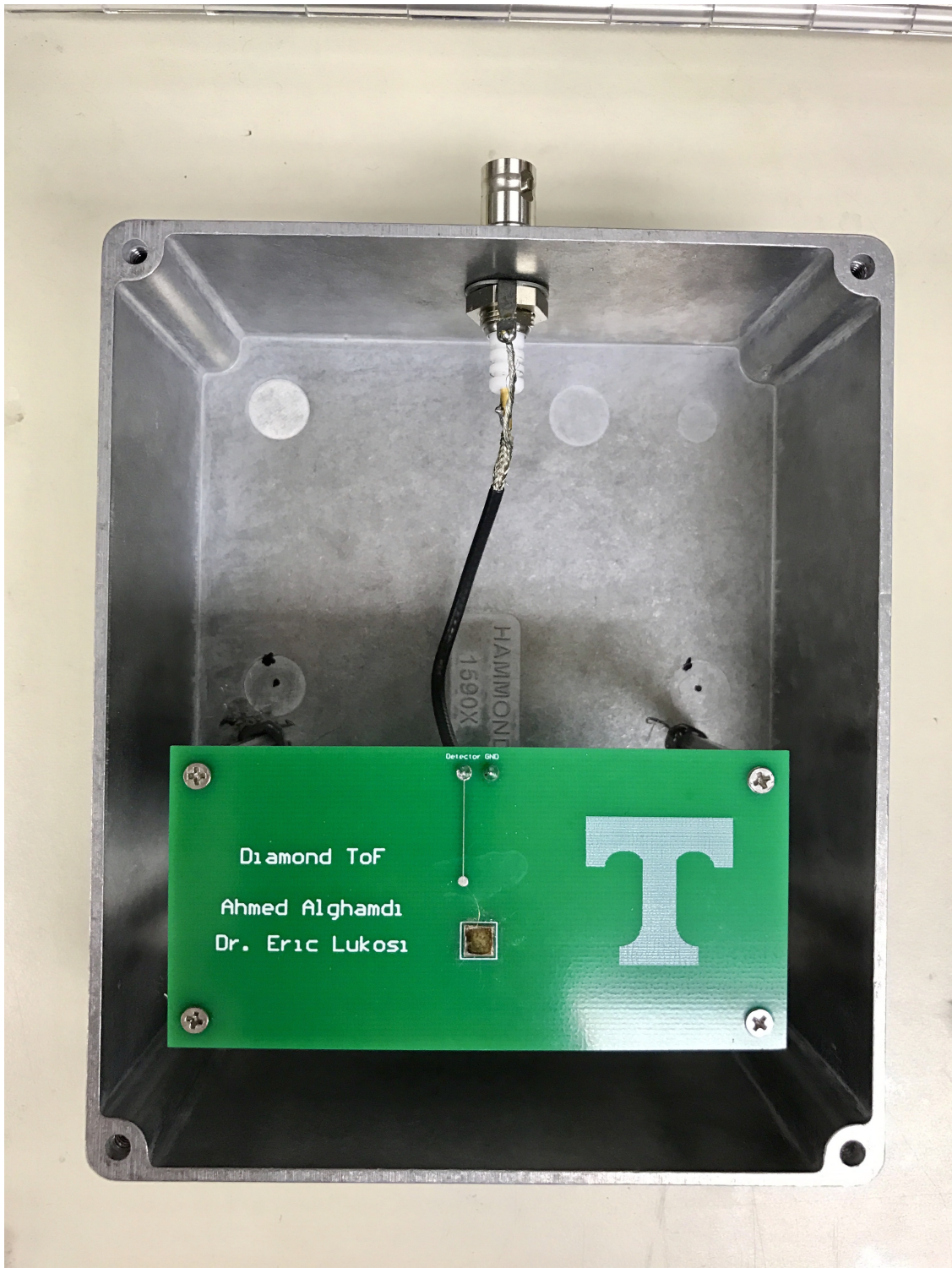


Figure 3.8: Aluminum box enclosure.

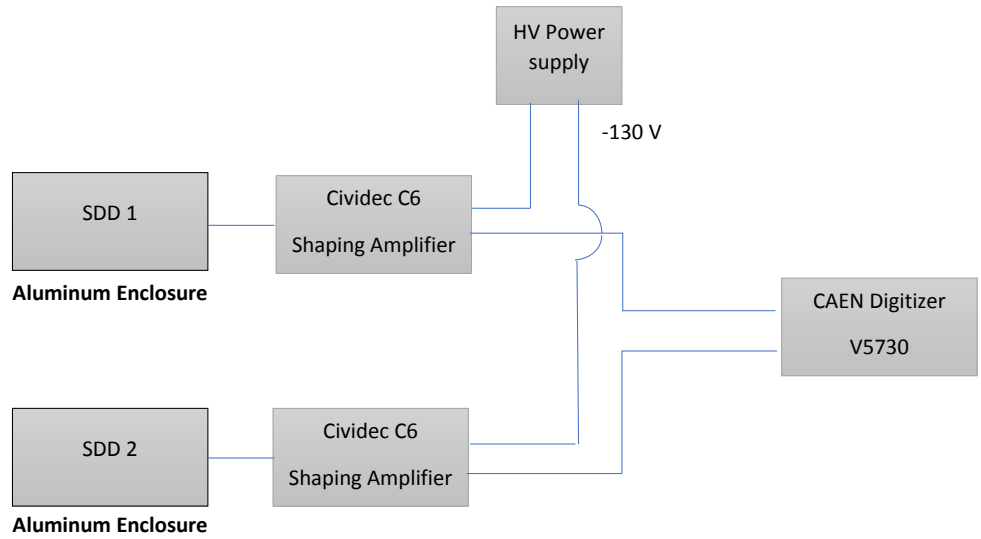


Figure 3.9: Electronic block diagram of the two-diamond system NSC.

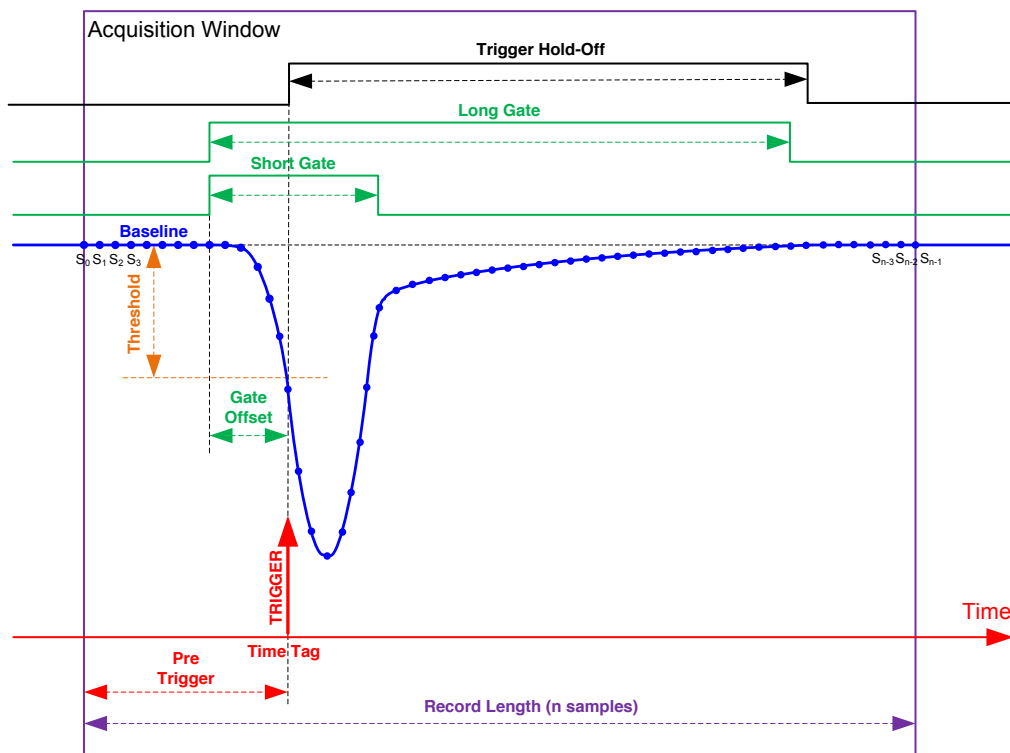


Figure 3.10: CAEN digitizer acquisition window.

3.7 Results

3.7.1 Two-Diamond Array

Mapping out the system sensitivity in simulation space to fast mono-energetic neutrons indicated that the angle between the two diamond detectors strongly impacted the sensitive energy range of the two-array diamond NSC. Separation distance was investigated based on the accuracy of the reconstructed energy of the 1 MeV mono-energetic neutron. Figure 3.11 displays the uncertainties of the reconstructed incident neutron for a variety of separation distances.

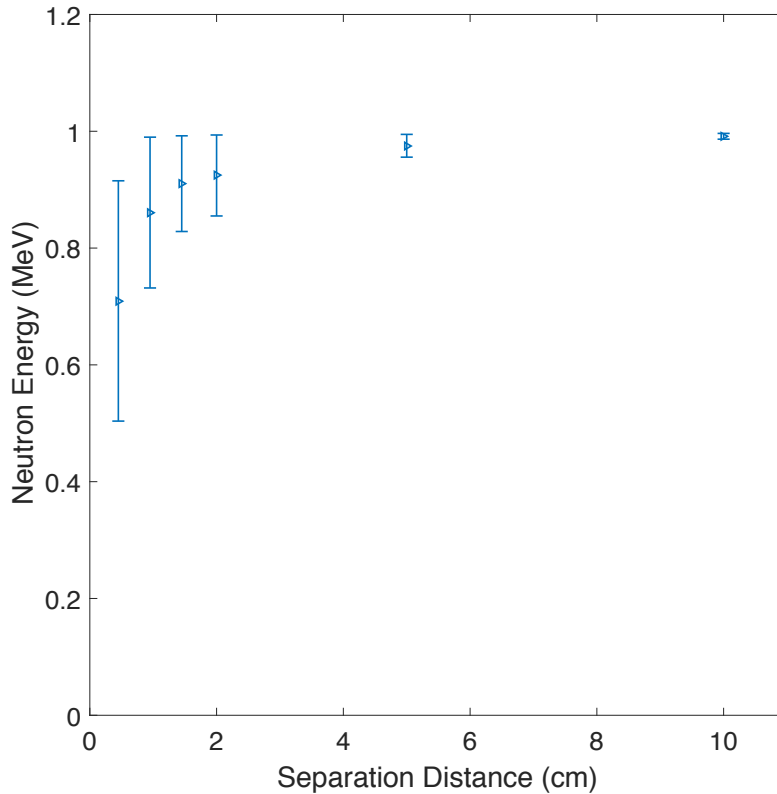


Figure 3.11: Reconstructed 1 MeV neutron energy of the two-diamond system in various separation distances.

The first diamond detector was stationary while the second diamond movable to two different positions for higher detection efficiency. Moreover, the two-diamond array NSC was simulated as three diamond detectors instead of running each position of second diamond separately. After running massive amount of different detection geometries, it was found that

best systems for detection efficiency and energy resolution was three $5 \times 5 \times 0.5 \text{ mm}^3$ diamond detectors separated by 10 cm. Moreover, for incident neutron energies below 1 MeV, the ideal angle that maximized detection threshold was 160° . For neutrons at or above 1 MeV, the best scattering angle based on simulation results was defined as 45° (see Figure 3.12).

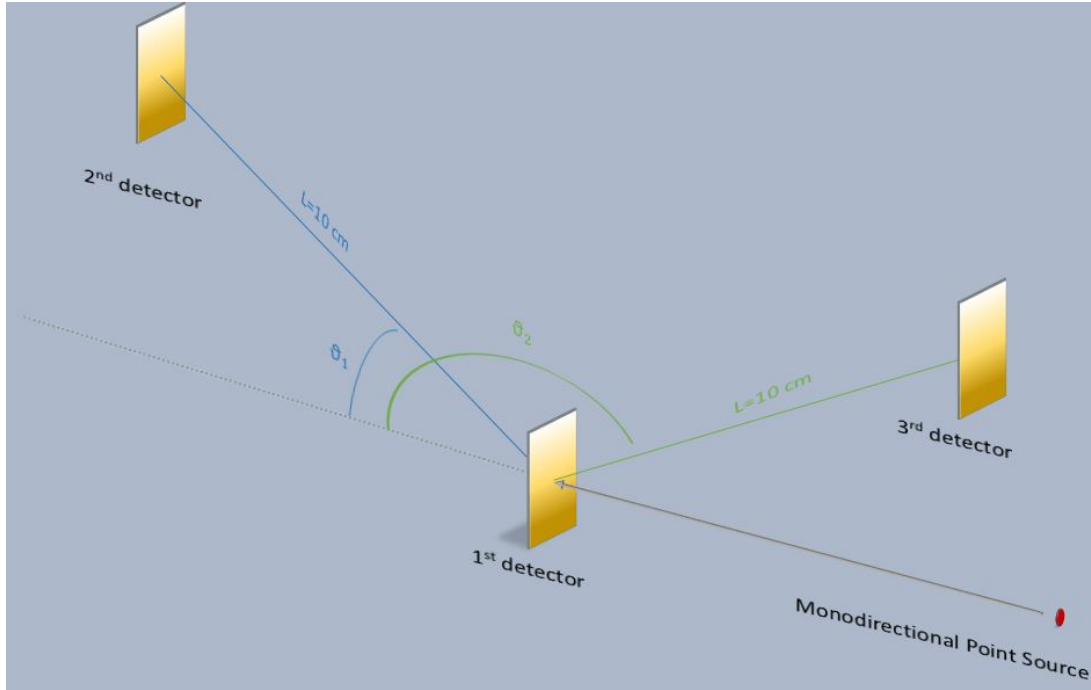


Figure 3.12: Two-diamond array NSC setup.

As discussed in the methodology section, both energy resolution and detection efficiency were defined for the detection system through simulation codes, as provided in Figure 3.13. It is evident from the figure that detection efficiency had significantly low values due to the compact size of diamond detectors beside the needs of double scattering events and relatively large separation distance to achieve convenient energy resolution. A proportional relationship between energy resolution and detection efficiency is seen from the figure as well.

In order to define the detection efficiency of the two-diamond NSC for experimental work, MCNP code was utilized to obtain the counts per hour for an isotropic $^{239}\text{Pu-Be}$ source. The source was located 50 cm from the detection system and modeled as point source with a neutron emission rate of $2.4 \times 10^6 \text{ n/s}$, which is similar to the neutron emission rate of Monsanto research corporation [62]. Figure 3.14 displayed the counts per hour for each separation distance.

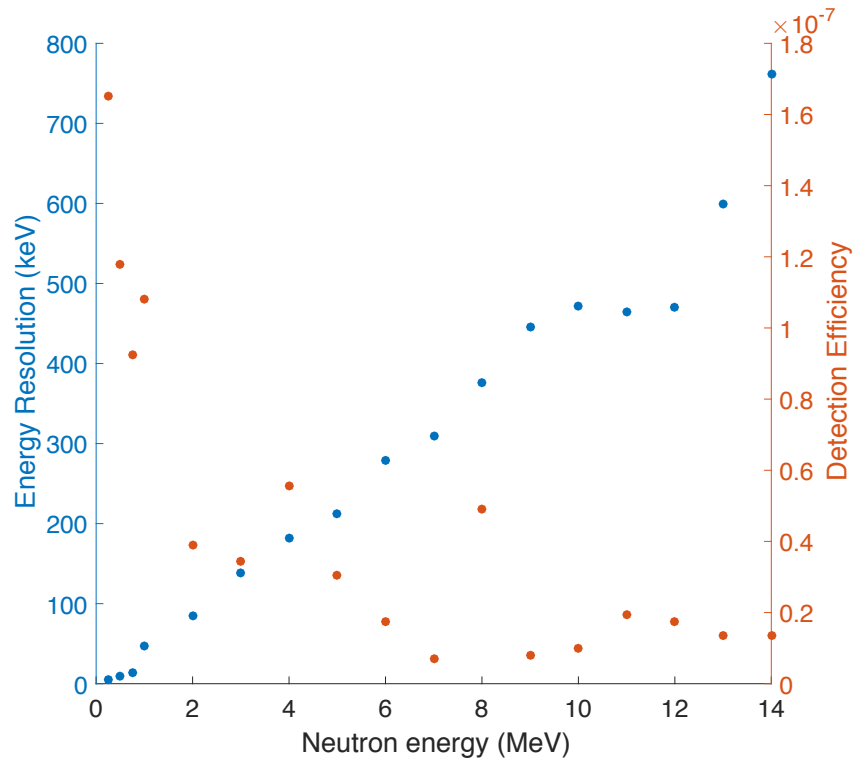


Figure 3.13: Detection efficiency and energy resolution of the two-diamond array system.

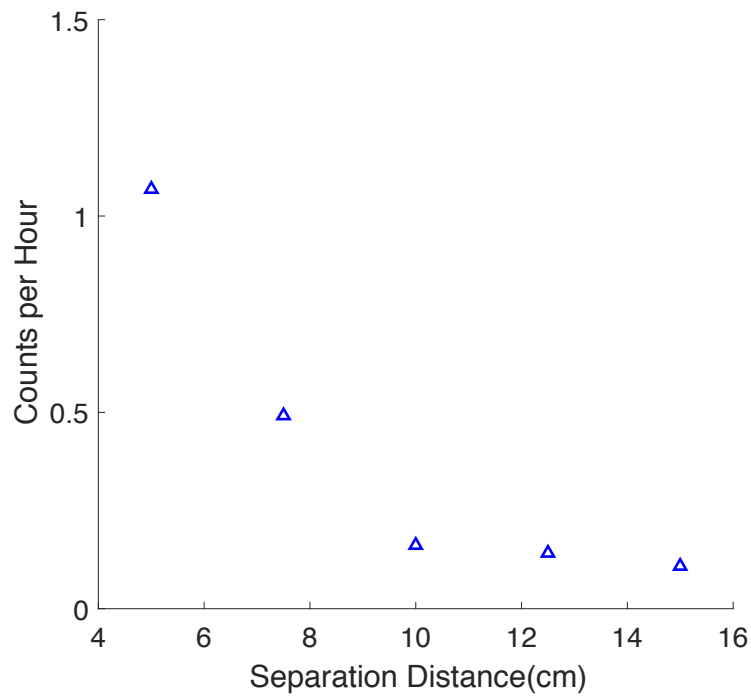


Figure 3.14: Two-diamond NSC system counts per hour for an isotropic ^{239}Pu -Be source.

The correction factor (CF) was essential for reconstructing the correct neutron energy spectrum from the measured response, as previously described. MCNP software was utilized to define the CF for any neutron source, where the CF represented the multiplying factor necessary to reconstruct the true neutron source energy spectrum. The two-diamond array geometry was modeled with a neutron source of one fixed value. In other words, the incident neutron was set as one histogram bin with the range 0.2-11.5 MeV (see Figure 3.15a). After running the simulation, the CF was defined for each bin as the ratio between the MCNP output spectrum and source value, as shown in Figure 3.15b.

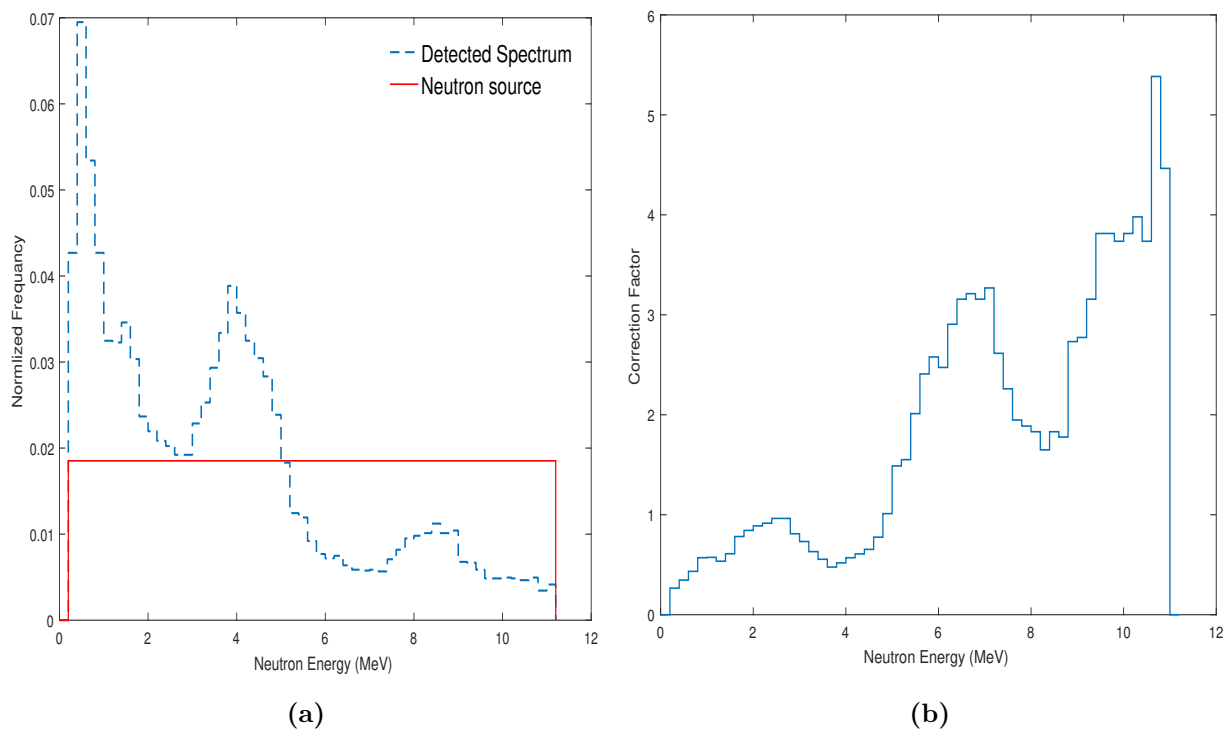


Figure 3.15: (a) Simulated neutron source and obtained spectrum. (b) Correction factor for the neutron source.

For the two poly-energetic neutron sources used, the two-diamond array NSC worked well to match the incident neutron spectrum. The results for a ^{252}Cf fission neutron source and ^{239}Pu -Be source are provided in Figure 3.16 and 3.17, respectively. After modification using CF, neutron spectra rendered better agreement with the neutron sources than an unmodified one. However, the higher energy (>8 MeV) of the modified spectrum for the ^{239}Pu -Be neutron source showed some fluctuations due to low counts.

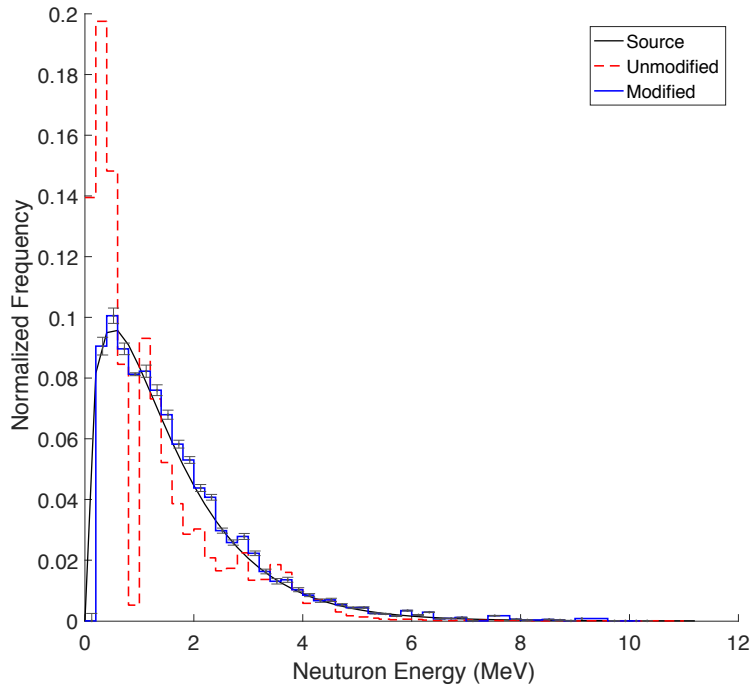


Figure 3.16: The reconstructed spectrum of ^{252}Cf source using two-diamond NSC.

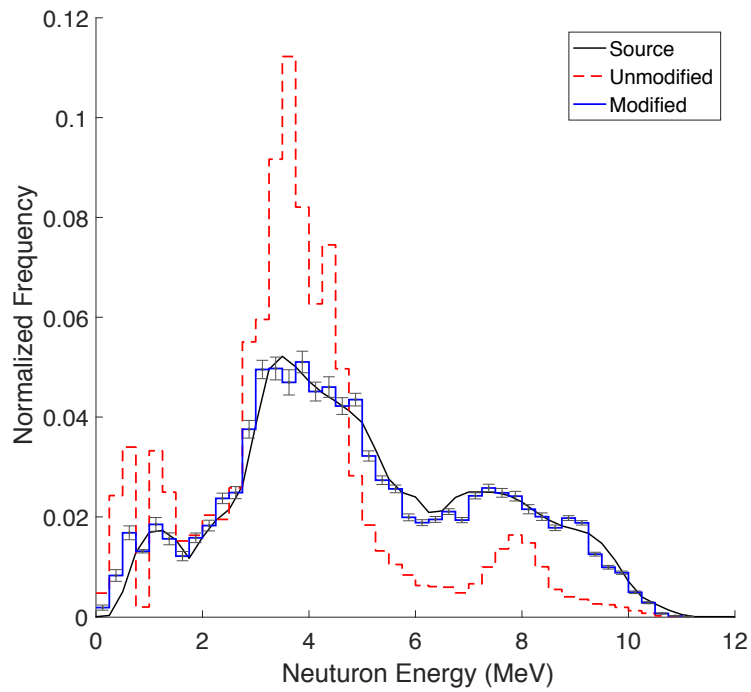


Figure 3.17: The reconstructed spectrum of $^{239}\text{Pu-Be}$ source using two-diamond NSC.

The simulated number of neutrons of ^{252}Cf (3×10^{11}) was equivalent to the measurement time of 6 hours of a ^{252}Cf isotropic source with a neutron emission rate of 2.314×10^{10} n/s located 50 cm away from the detection system, the source emission comparable to Frontier technology corporation ^{252}Cf source model no. 100 [63]. For isotropic $^{239}\text{Pu-Be}$ source, the emission rate was defined as 2.4×10^6 n/s, based on the expected neutron emission rate of University of Tennessee $^{239}\text{Pu-Be}$ source, and the distance between the source and the first diamond was 10 cm [62]. The expected measurement time would be approximately 97 days, which is extremely long time due to the low detection efficiency of the system.

To increase the detection efficiency and enhance energy resolution, a 16-pixel two-diamond system was simulated as well. Each pixel was 1.25×1.25 mm² in area. The separation distance between the diamond plates was reduced to 5 cm to achieve higher detection efficiency while also maintaining good energy resolution. Figure 3.18 displays the reconstructed incident neutron spectrum for each neutron source with and without the use of the CF. Good agreement of the incident neutron sources was also achieved for the 16-pixel two-diamond array.

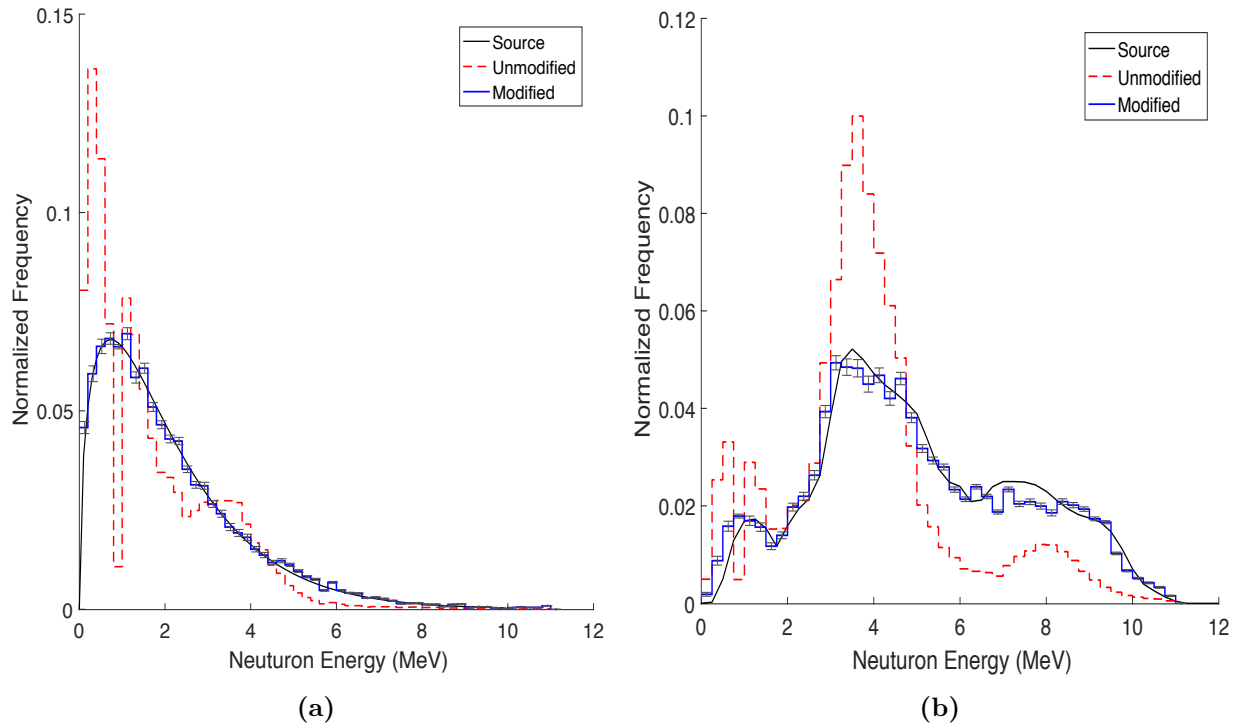


Figure 3.18: 16-pixel two-diamond array reconstructed spectrum for (a) ^{252}Cf source and (b) $^{239}\text{Pu-Be}$ source.

3.7.1.1 Experimental measurements

Two bare ^{239}Pu -Be neutron sources were used. Each source activity was 1 Ci with a neutron emission rate of 2.4×10^6 neutrons per second. Due to the nature of isotropic sources and the proximity of the second SDD and neutron sources, measurement was performed only for the 45° position. Additionally, the sources were aligned and placed 2 cm from the first SDD. More separation distance was needed to gain mono-directional neutrons for better energy resolution. However, for time consideration, both sources were kept in their positions to obtain more neutron counts. Also, for the same reason, the separation distance was reduced to 5 cm instead of 10 cm. To decrease the vibration of the table, all electronics were placed atop a wooden panel (see Figure 3.19).

The CFD mode was activated for the measurements to gain good timing resolution measurements. However, after three days of running, the system showed an insignificant amount of counts, mostly saturation counts. Consequently, the LED mode was chosen instead with 60 lsb threshold to avoid the low noise signals. The pulse height spectrum was measured for the second SDD because, being further from the sources, it demonstrated lower γ ray interactions than the first SDD. Figure 3.20 shows the pulse height spectrum of the second SDD. The two-peak interaction of inelastic scattering $^{12}\text{C}(n,\alpha)^9\text{Be}$ and $^{12}\text{C}(n,n')3\alpha$ were clearly seen in centered channel numbers 60 and 150, respectively. However, the first peak was broadened because of the elastic scattering of wide neutron spectrum of the ^{239}Pu -Be source.

The experiment was conducted for a total time of 370 hours. The output data proceeded offline through a Matlab code built to read both files and determine the ToF data of each interaction. Based on a previous neutron ToF calculation of the ^{239}Pu -Be source, the Matlab code accepted only events with ToF in the range (1,7.2) units in nanoseconds. The time range was calculated for the the upper and lower neutron energies of the ^{239}Pu -Be source based on the separation distance (5 cm). Additionally, the code extracted only events with a fine time stamp flag. The final step was converting the measured ToF into an energy histogram and modifying it by using the simulated CF. Figure 3.21 displays the modified spectrum along with the expected neutron source spectrum [64].



Figure 3.19: Arrangement of the two-diamond array NSC experiment.

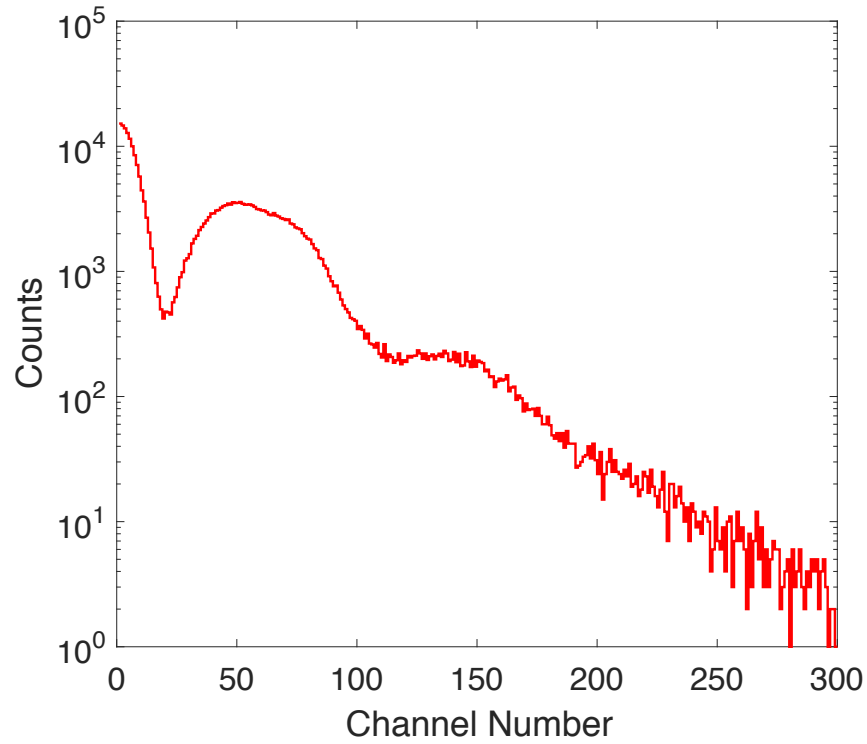


Figure 3.20: Pulse height spectrum of ^{239}Pu -Be source in the second SDD.

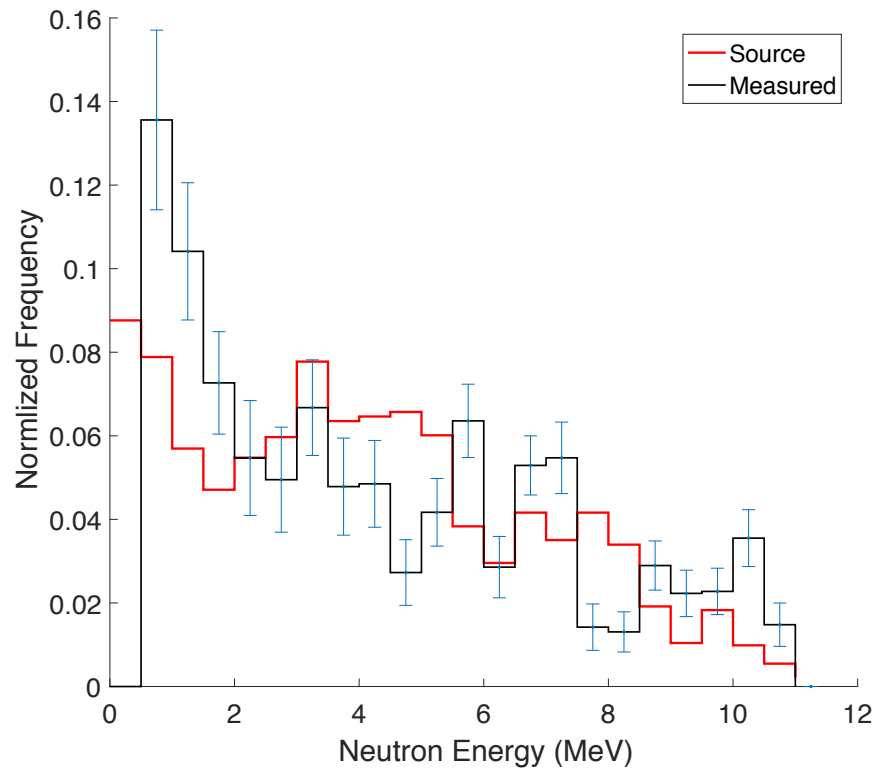


Figure 3.21: Reconstructed neutron spectrum of the ^{239}Pu -Be source.

The neutron spectrum of the ^{239}Pu -Be source depends mainly on the mass and weight fraction of Pu isotopes within the source which was undefined. In addition, the ^{239}Pu -Be sources were manufactured in 1960, which led to significant growth of daughter nuclei. The high decay constant of the daughter nuclide (^{241}Am) created an increase in the (α, n) interaction rates and, consequently, in the neutron yield of the sources [65]. Thus, the current neutron spectrum of the used sources may slightly differ from the expected neutron spectrum. Still, the experimental results matched the peak neutron energy regions of the ^{239}Pu -Be neutron spectrum. In addition, statistical fluctuations appeared in the spectrum due to the low counts of the system.

3.7.2 Diamond Array System

The structure of the diamond array was obtained through different design layouts. First, it was found that the optimum distance between the two planes was 5 cm for spectrum analysis. Furthermore, it was found that a 1-cm separation distance between diamond planes was best to pinpoint source location. Each of the two planes in the diamond array contained 16 diamond detectors, and each diamond detector was $5 \times 5 \times 0.5 \text{ mm}^3$ with an even array of 4×4 pixels. The minimum energy deposition that could be registered was set to 10 keV. Figure 3.22 provides the detection system setup.

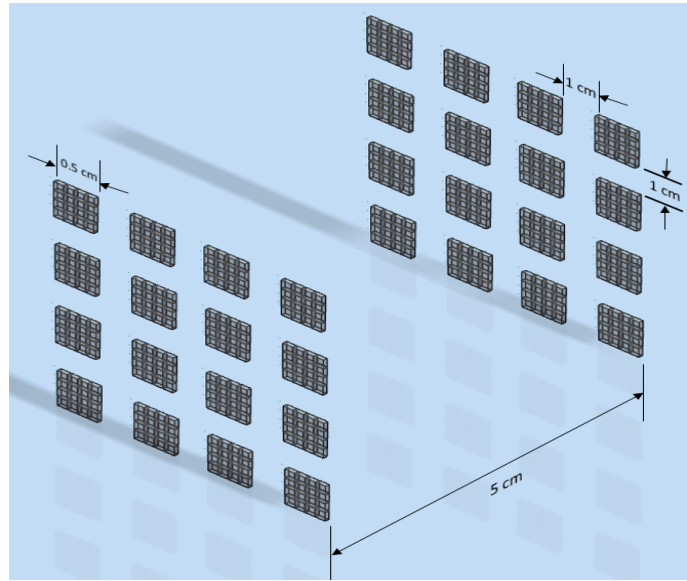


Figure 3.22: Schematic view of the diamond array NSC.

3.7.2.1 Spectral Analysis

As presented earlier, the CF was used for the diamond array system. Afterwards, the system demonstrated the ability of reconstructing an incident neutron source spectrum, as shown in Figure 3.23.

Both neutron sources spectra were built successfully. The modified spectrum was significantly enhanced through CF; however, fluctuations appeared in the reconstruction spectra due to the high variation of neutron-scattered angles in the system. Nevertheless, the diamond array system was able to detect as low as 257 KeV incident neutrons.

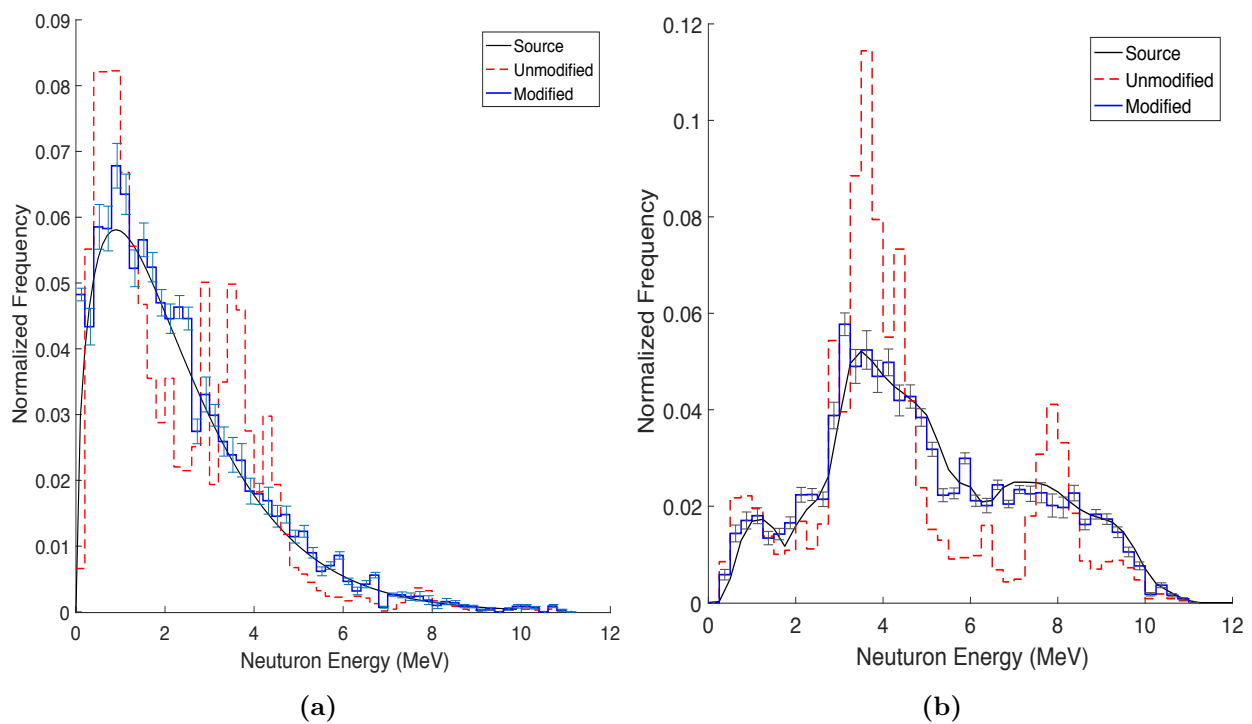


Figure 3.23: Diamond array system reconstructed spectrum of (a) ^{252}Cf source (b) $^{239}\text{Pu-Be}$ source.

3.7.2.2 Source Localization

To investigate the image resolution of the detection system, both mono-energetic and ^{252}Cf poly-energetic neutron sources were modeled as point sources in various coordinates in front of the diamond-array system. The front array of NSC was placed at the center of the axis

coordinates (0,0,0). Configuration of source positions is listed in Table 3.1. Diamond array NSC-generated images are displayed for all configurations in Figure 3.24.

All images pinpointed the sources with high accuracy. The image indicate the exact 2D coordinates for each source; the image resolution is discussed in the next section. The diamond array system manifested a high sensitivity in locating neutron sources even with low cones counts, as indicated in Figure 3.25. For only 50 cones, the diamond array NSC define the locations of two close sources.

As stated previously, the reconstructed image plane located the neutron source in 2D (z and x axes). However, dissimilarity of the y-component between the image plane and incident neutron source led to a significant reduction of image resolution. Figure 3.26 shows the reconstructed image in several different locations for configuration No. 4.

The difference between Y distances and the actual simulation resulted in image blurring, and aliasing presented as well in Figures 3.26a and 3.26c. Consequentially, a limitation of locating neutron sources was observed. To resolve this issue, the reconstructed code generated numerous images for multiple distances (Y), and the user defined the optimum image. This issue could be addressed as well through a machine-learning or image-processing algorithm. However, because this advanced algorithm is beyond the scope of this research, the first solution was utilized.

The measurements' time that the system would take for all configurations, which are listed in Table 3.1, were calculated based on neutron emission rate of ^{252}Cf and 4MeV mono-energetic beamline. Firstly, ^{252}Cf source of Frontier technical cooperation was utilized in this calculation. The ^{252}Cf source model no. 100 has a neutron emission rate of $2.314 * 10^{10}$ n/s based on 10 mg mass of ^{252}Cf isotopes within the source capsule [63]. The expected

Table 3.1: Configuration of simulated point sources.

Configuration No.	Neutron source	Coordinates (cm)
1	Mono-energetic (4 MeV)	(10,100,0)
2	^{252}Cf	(0,10,0)
3	^{252}Cf	(5,200,5)
4	Mono-energetic (4 MeV)	(10,100,0)
	Mono-energetic (4 MeV)	(0,100,10)

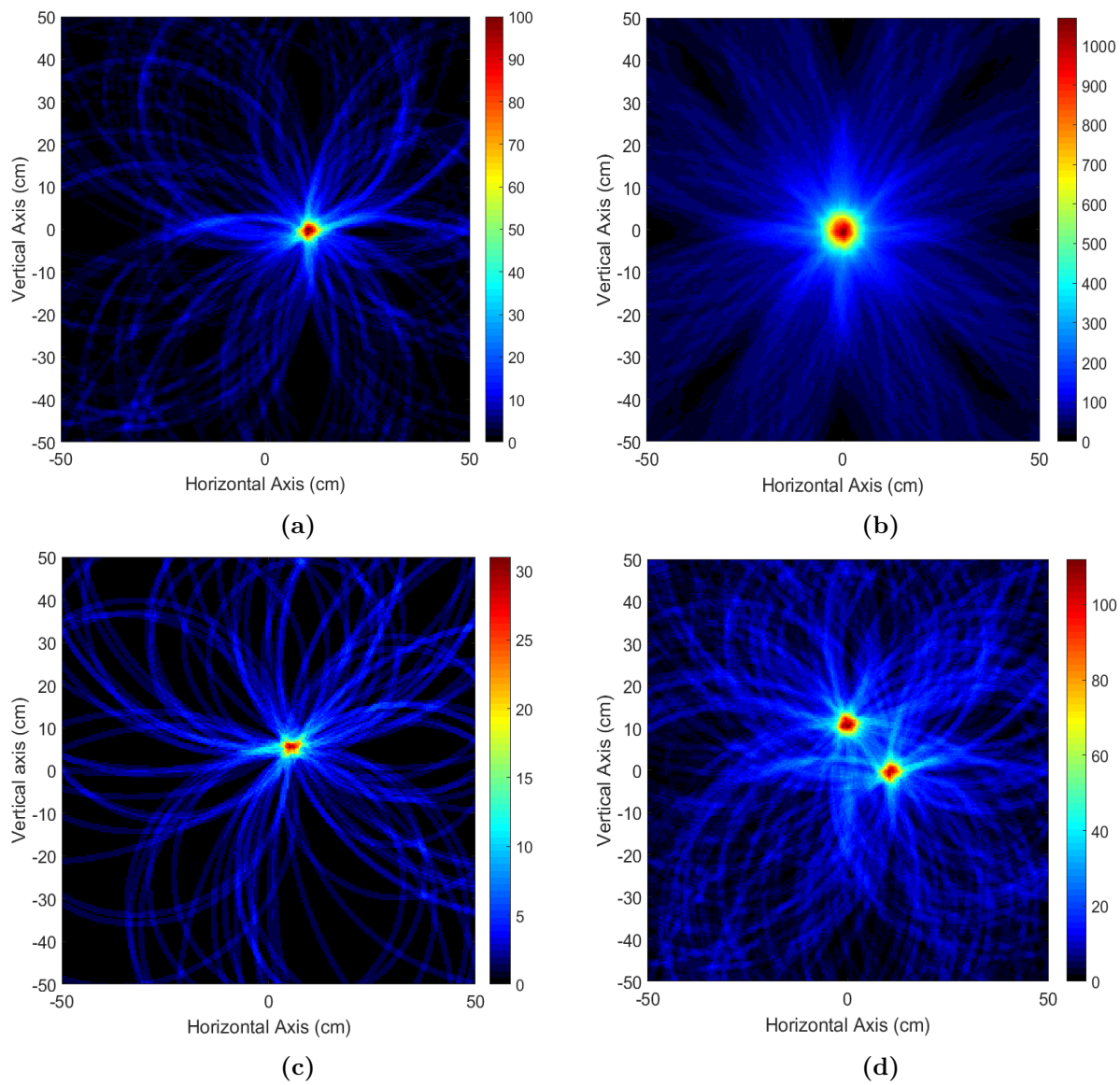


Figure 3.24: Diamond array system reconstructed images for configuration No. (a) 1 (b) 2 (c) 3 and (d) 4 as listed in Table 3.1.

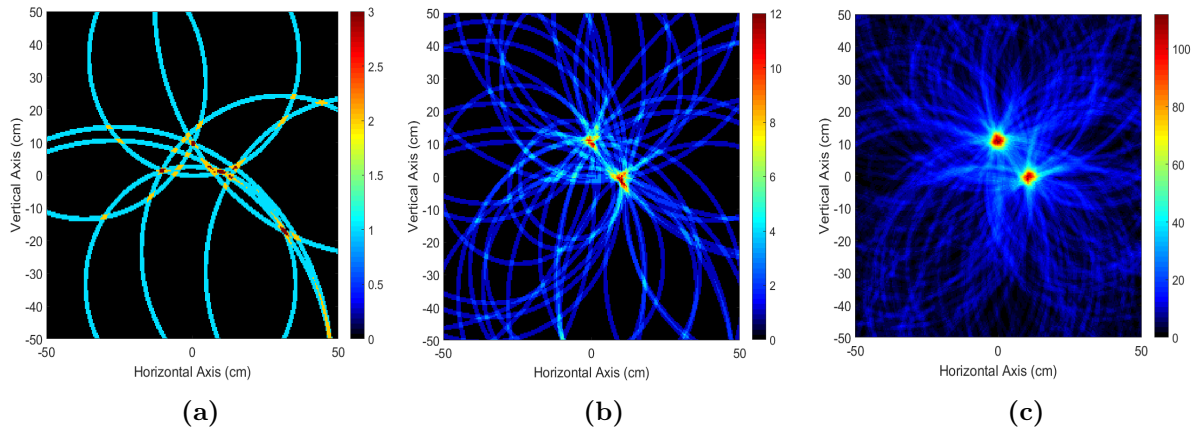


Figure 3.25: Reconstructed image planes for two 4 MeV mono-energetic neutron sources located at $(10, 100, 0)$ and $(0, 100, 10)$ for multiple cone rates (a) 10 cones (b) 50 cones (c) 500 cones.

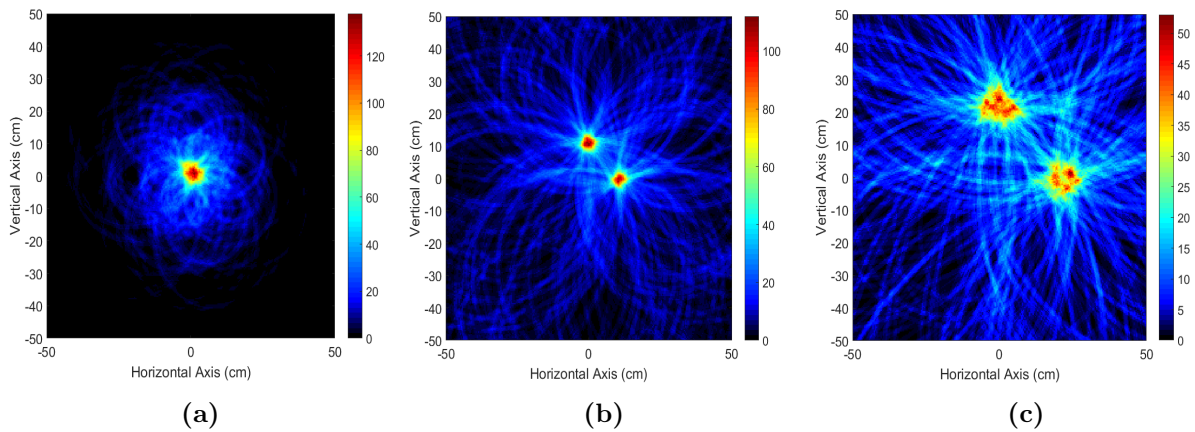


Figure 3.26: Reconstructed image planes for two 4 MeV mono-energetic neutron sources located at $(10, 100, 0)$ and $(0, 100, 10)$ for different Y distances (a) 20 cm (b) 100 cm (c) 200 cm.

measurements' time was calculated by assuming the ^{252}Cf neutron source as an isotropic point source instead of the source's cylindrical shape.

The beamline of the University of Ohio was considered as the mono-energetic neutron source, since there are no other neutron sources which can afford the value of 4 MeV neutron. The beamline generated 4 MeV neutrons with the interacted rate of 3000 n/s [66]. The measurements' time was calculated and listed in Table 3.2 for all configurations.

For configurations 1 and 4, very long measurements' time was calculated due to the low flux intensity of the beam. As an alternative, the mono-energetic neutron from the D-T generator (14.1 MeV) would provide much higher neutron rate ($5.0 * 10^{11}$ n/s) and, correspondingly, lower measurements' time [67]. For ^{252}Cf source configurations, the measurement times were found reasonable as a result of the high activity of the source. Furthermore, the significant difference between the measurement times of configurations 2 and 3 was due to the differences in source locations.

3.7.2.3 Image Resolution

The image resolution was calculated based on the point source of ^{252}Cf located at (0,0) and located 10 cm away from the center of the first array of diamond array NSC. In order to reduce the machine runtime, the source was simulated as a cone source with a history of 10^{10} neutron particles. Equation 3.12 was implemented to define the resolution of the image after creating 2D profiles for horizontal and vertical axes. The two profiles were plotted for 10 keV energy threshold and normalized (see Figure 3.27).

Table 3.2: Expected measurement time for each configuration.

Configuration No.	Neutron source	Coordinates (cm)	Measurements time
1	Mono-energetic (4 MeV)	(10,100,0)	925.92 hr
2	^{252}Cf	(0,10,0)	2.61 min
3	^{252}Cf	(5,200,5)	20.51 min
4	Mono-energetic (4 MeV) Mono-energetic (4 MeV)	(10,100,0) (0,100,10)	1851.85 hr

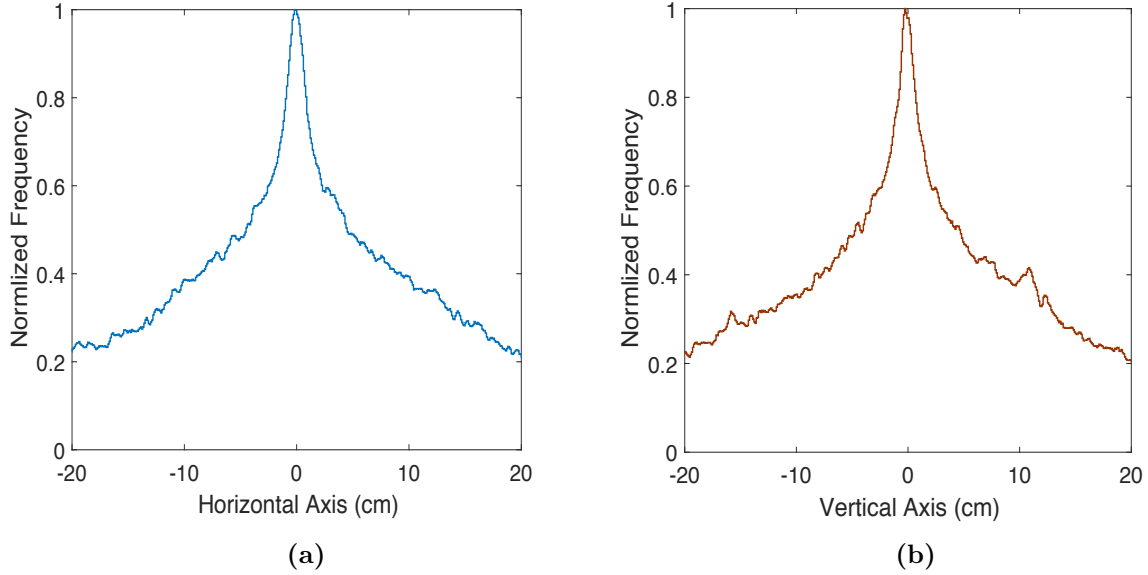


Figure 3.27: The 2D profiles of (a) horizontal and (b) vertical axes of the reconstructed image for a ^{252}Cf point source located at (0,10,0).

The image resolution of the diamond array system was determined for each axis direction. For horizontal axis, the mean value was found to be 0.22 cm with 1σ of 3.82 cm, while the vertical axis resolution was 4.01 cm with the mean value of 0.21 cm. The mean values for both directions were very close to the exact location of the ^{252}Cf point source. However, the uncertainties associated with the ToF equations and plotted cones are expected for slight variation of the source location. The imaging efficiency of the system was demonstrated by identifying the ratio of number of cones to the simulated neutron numbers and it was calculated as $1.186 \cdot 10^{-8}$ for the same threshold value (10 keV). Two more different threshold values were applied to define the image resolution for higher neutron energy depositions as shown in Table 3.3. The higher threshold demonstrated higher uncertainties and lower imaging efficiency due to the low plotted cones.

Table 3.3: Diamond array NSC resolution and number of cones for different energy thresholds.

Threshold (keV)	Number of Cones	σ_H (cm)	σ_V (cm)	Imaging efficiency
10	1186	3.83	4.01	$1.19 \cdot 10^{-7}$
30	720	3.83	4.34	$7.20 \cdot 10^{-8}$
50	456	4.32	4.67	$4.56 \cdot 10^{-8}$

The simulated number of neutron particles might be similar to the neutron emissions of Frontier technical cooperation ^{252}Cf source located at the same location of the simulation source in approximately 30 seconds [63]. However, measurements might take more time, since they were calculated by assuming the ^{252}Cf neutron source as an isotropic point source.

Chapter 4

Diamond Time-of-Flight Detector

4.1 Introduction

Neutron particles, most frequently, induce fission reactions with actinides nuclei. The heavy target nucleus absorbs the incident neutron and forms unstable nuclei that split instantaneously, releasing a significant amount of energy (≈ 200 MeV). The released energy is distributed amongst the produced fission fragments, β , neutrinos, γ rays, and neutrons. Fission neutrons are either delayed or spontaneously generated (within a very short time frame $\approx 10^{-14}$ second). Prompt neutrons are the dominant produced neutrons ($\approx 99\%$) of fission reaction. Additionally, released prompt neutrons are considered a major part in propagation fission reactions in nuclear reactors and also in detecting SNM materials using both passive and active neutron interrogation techniques [19, 47].

Due to the importance of prompt neutrons, Chi-Nu experiments were implemented to obtain more accurate evaluated data of the fission reaction with actinides to replace the Los Alamos model data. The Los Alamos model shows high uncertainties in many energy ranges in prompt neutron spectra for major actinides isotopes [68]. The Diamond Time-of-Flight Detector (DToF) was simulated to study both the feasibility of the obtained accurate spectra of prompt neutrons and the multiplicity factors for reactor design and nonproliferation application. The Monte Carlo simulation code was conducted in this simulation study using multiple targets of two SNM materials (^{235}U and ^{239}Pu).

4.2 MCNP code

MCNP6 codes were written with PTRAC card to measure the prompt fission neutron spectra of two valuable and prevalent SNM materials (^{235}U and ^{239}Pu). Also, the simulation study aimed to evaluate the effects of different thicknesses of the two SNM materials for the neutron multiplicity counter. Isabel models physics with Denser evaporation model were invoked to simulate the fission reaction [69].

The DToF was modeled as a target diamond detector (5 mm x 5 mm x 0.5 mm) coated with either a ^{235}U or ^{239}Pu target of various thicknesses (1, 10, 100, and 1000 μm). Two mono-energetic fast neutron sources (1 MeV and 4 MeV) were modeled as mono-directional point sources to induce the fission reaction in the SNM targets. The released prompt fission neutrons scattered through a diamond sphere surrounding the SNM targets, as shown in Figure 4.1. The sphere had a thickness of 1 cm to achieve good detection efficiency (for 2 MeV neutron $\approx 26\%$). However, the overall detection efficiency of the DToF reduced for the same neutron energy to approximately 2% because of the low thickness of the target diamond.

The high released energy of the fission reaction was used as a trigger to discriminate between fission and other interactions (elastic,inelastic and absorption). Therefore, prompt fission neutron spectrum was reconstructed based on the measurements of the interrogating fast neutron time (ToF 1) and the interaction of fission neutrons with the surrounding sphere (ToF 2). Additionally, the model accounted for the neutron multiplicity factor of each SNM thickness by computing the neutrons detected after each successful fission reaction.

4.3 Data Analysis

I modified the DNSC post-processing C++ code to analyze the PTRAC output files for this model. For every fission interaction in the target, the ToF of the prompt fission detected in the surrounding sphere was recorded beside interaction coordinates. Nevertheless, the interacted γ rays were neglected due to the capability of differentiate that easily through

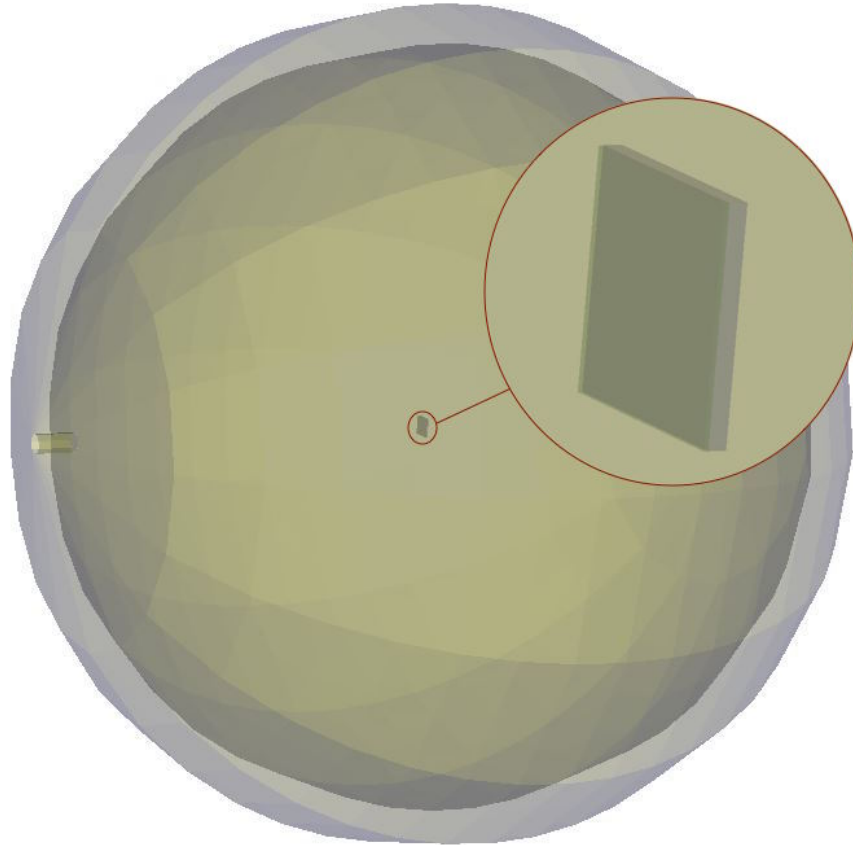


Figure 4.1: Schematic view of the DToF detection system.

ToF information. For efficiency-comparison purposes, the total number of fission reactions and generated prompt neutrons were recorded as well.

All of the recorded information was passed through a Matlab code to implement the plots of prompt neutron fission spectra. Moreover, graphs were corrected due to the variation in neutron interaction cross-section with carbon atoms (as discussed in the previous chapter). Each bin of prompt neutron fission spectra was divided by the average value of corresponding elastic scattering cross-section.

The code generated the neutron multiplicity factor for each thickness. Also, the total number of induced fission reactions was recorded to define the average of released neutrons per fission reaction ($\bar{\nu}$). $\bar{\nu}$ values were corrected due to the overall low detection efficiency of DToF system.

The total number of detected neutrons were recorded for each target thickness to prove a linear relationship between the two, as shown in Figure 4.2.

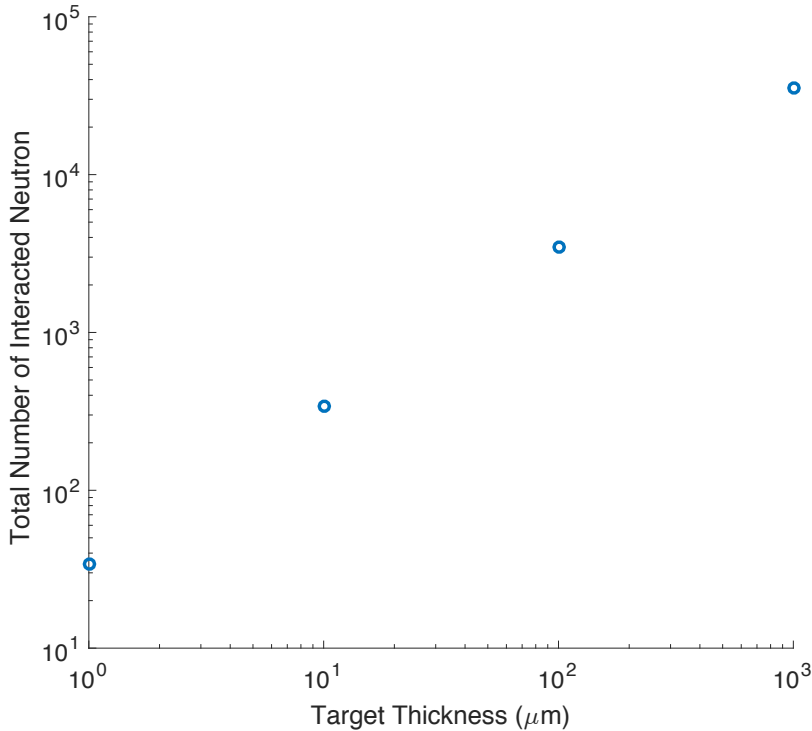


Figure 4.2: Total numbers of detected neutrons for ^{239}Pu target with 1 MeV incoming neutron.

4.4 Results

4.4.1 Prompt Fission Spectrum

The prompt neutron spectra have the shape of a Watt spectrum in both materials. The simulated results were conducted with the thickest targets ($1000 \mu\text{m}$) since they have produced the highest fission reactions and, correspondingly, has the highest detected neutrons, thus offering the best statistical results. The DToF prompt fission spectra are displayed in Figures 4.3 and 4.4 for the 1 and 4 MeV incident neutron, respectively. The simulated spectra were corrected for cross-section variation and, compared to the ENDF-evaluated data, showed good accuracy. Still, a more accurate correction factor is needed to avoid the spectra fluctuations.

From the simulated spectra, the 4 MeV neutron aligns more with the ENDF-evaluated spectrum. Also, plots indicate the use of coated SNM material with the diamond detector in such measurements.

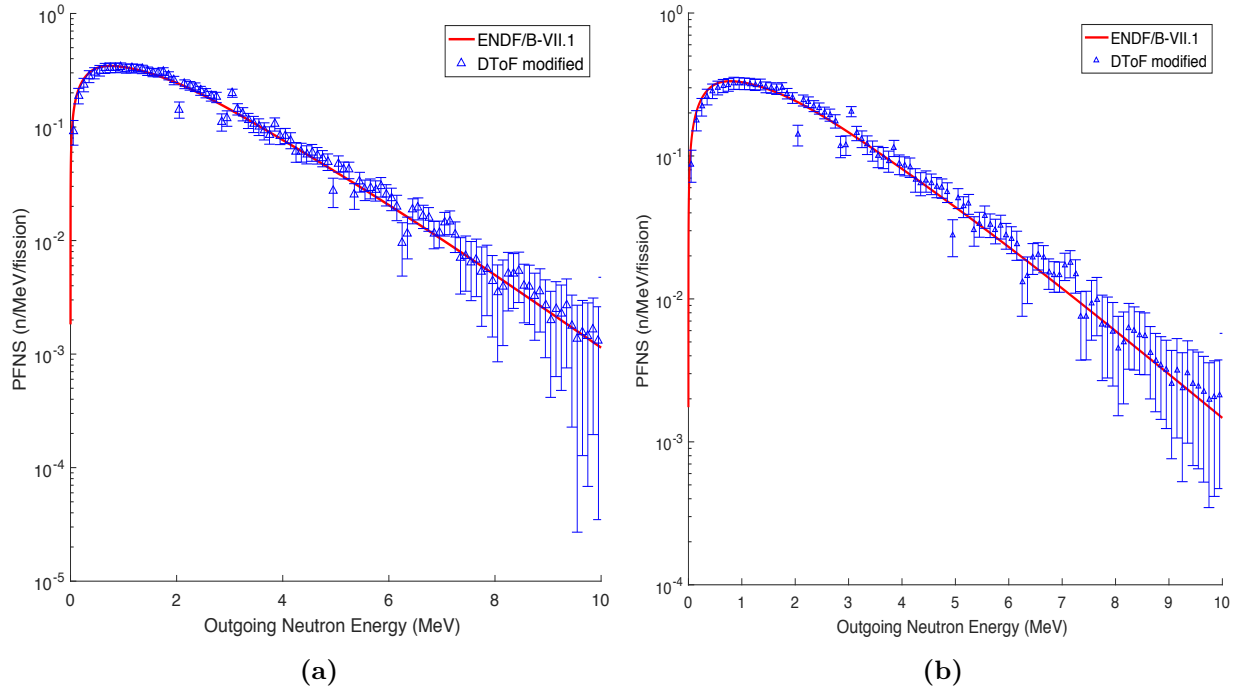


Figure 4.3: The prompt fission neutron spectra of the 1 MeV incident neutron with 1000 μm thick target of (a) ^{235}U (b) ^{239}Pu .

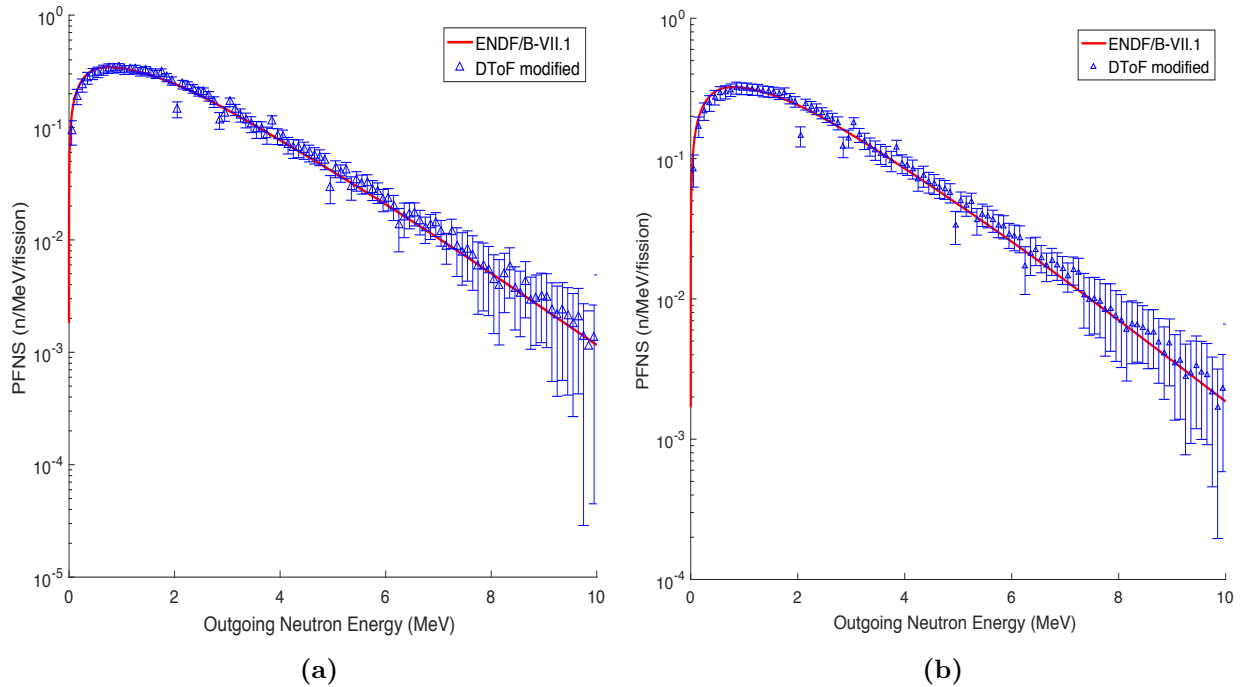


Figure 4.4: The prompt fission neutron spectra of the 4 MeV incident neutron with 1000 μm thick target of (a) ^{235}U (b) ^{239}Pu .

In the simulation, the mono-energetic neutron history was set as 10^8 for each incident neutron and target. Based on the neutron rate of the University of Ohio accelerator, the expected measurement time for each target was 27.8 hours, which is a very reasonable time compared to the duration of the Chi-Nu experiment for each target (9-12 weeks) [66, 70].

4.4.2 Neutron Multiplicity Counter

Neutron multiplicity factors are displayed in Figures 4.5 and 4.6 for the 1 and 4 neutron sources, respectively. The multiplicity factors of neutron interaction are needed to demonstrate the feasibility of the DToF system in SNM detection using the active interrogation technique. Higher thickness shows more multiplicity-counting. However, the higher thickness of the target might prevent the target diamond from detecting the fission fragments, which contain the majority of the fission released energy. Consequently, the DToF might not trigger the fission interaction.

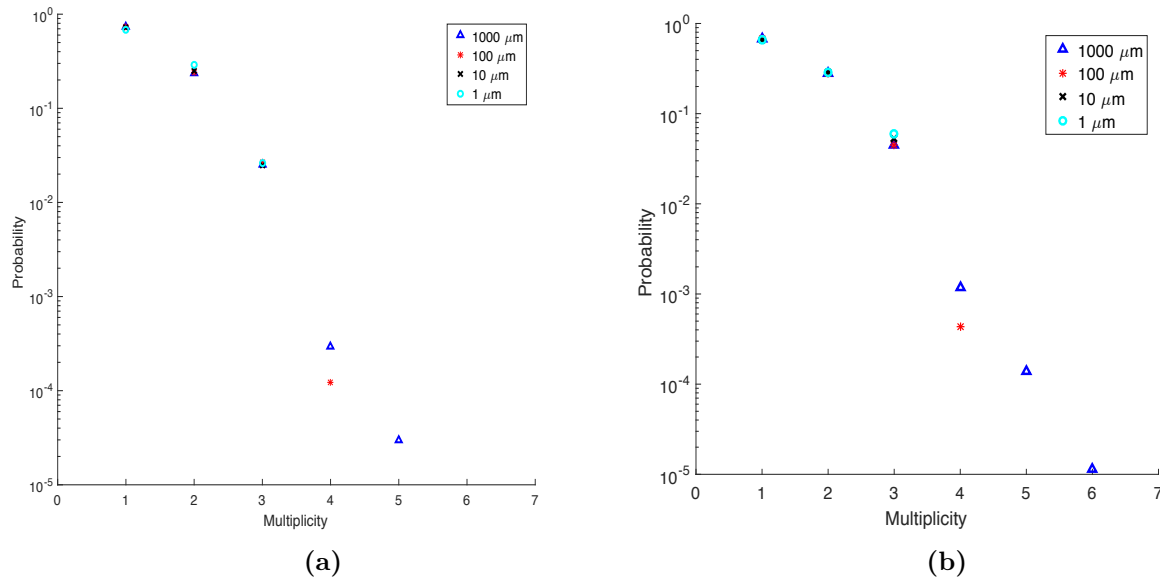


Figure 4.5: Neutron multiplicity factor for the 1 MeV neutron source and 1000 μm thick target of (a) ^{235}U (b) ^{239}Pu .

The 4 MeV neutron source demonstrated a higher probability of detected multiple neutrons (up to 4 neutrons per fission) for 1 μm for ^{239}Pu isotope. This result indicated the advantage of the DToF system in the field of the active interrogation detection system, even for thin SNM targets.

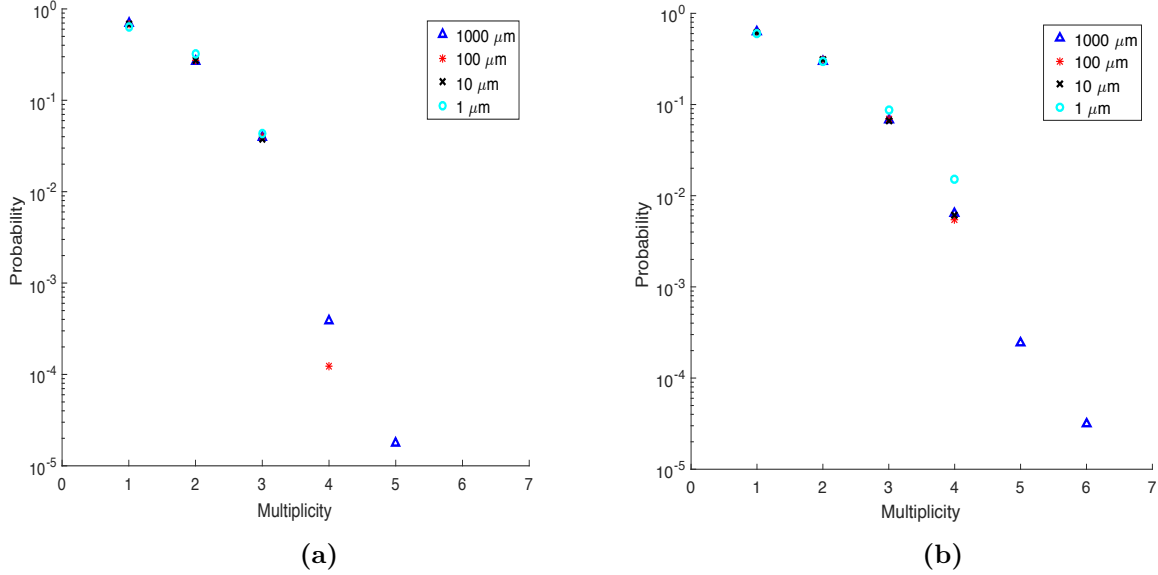


Figure 4.6: Neutron Multiplicity factor for the 4 MeV neutron source and 1000 μm thick target of (a) ^{235}U (b) ^{239}Pu .

4.4.3 $\bar{\nu}$ Calculation

$\bar{\nu}$ is the average number of fission neutrons per fission interaction. It is essential for designing nuclear reactors to propagate fission reactions in the reactor core. For simulated results, $\bar{\nu}$ must be corrected for low efficiency of the DToF system.

Basically, the detection efficiency is defined as the number of neutrons recorded by the DToF system (N) divided by the total neutrons generated within the target (S) [21]. Additionally, the efficiency is a function of solid angle and intrinsic resolution of the diamond detector. Because the diamond sphere is surrounded the target diamond, the solid angle is 4π . However, the low thickness of the diamond detector provided limited intrinsic efficiency, which must be taken into account. The detection efficiency was calculated through the MCNP code by finding the ratio between interacting neutrons and the total fission neutrons from the SNM target. Table 4.1 displays the detection efficiency of the DToF for the two material targets with different thicknesses. The overall detection efficiency for all neutron incident energies and all targets was approximately 3%. Based on the DToF detection efficiency, $\bar{\nu}$ was corrected and plotted as shown in Figure 4.7.

Table 4.1: Detection efficiency of the DToF system.

Target material	Neutron energy (MeV)	Target thickness (μm)	Detection efficiency (%)
U-235	1	1	2.87
		10	2.94
		100	3.11
		1000	3.06
	4	1	2.94
		10	3.13
		100	3.10
		1000	3.06
Pu-239	1	1	3.03
		10	3.09
		100	3.11
		1000	3.09
	4	1	3.01
		10	3.17
		100	3.14
		1000	3.11

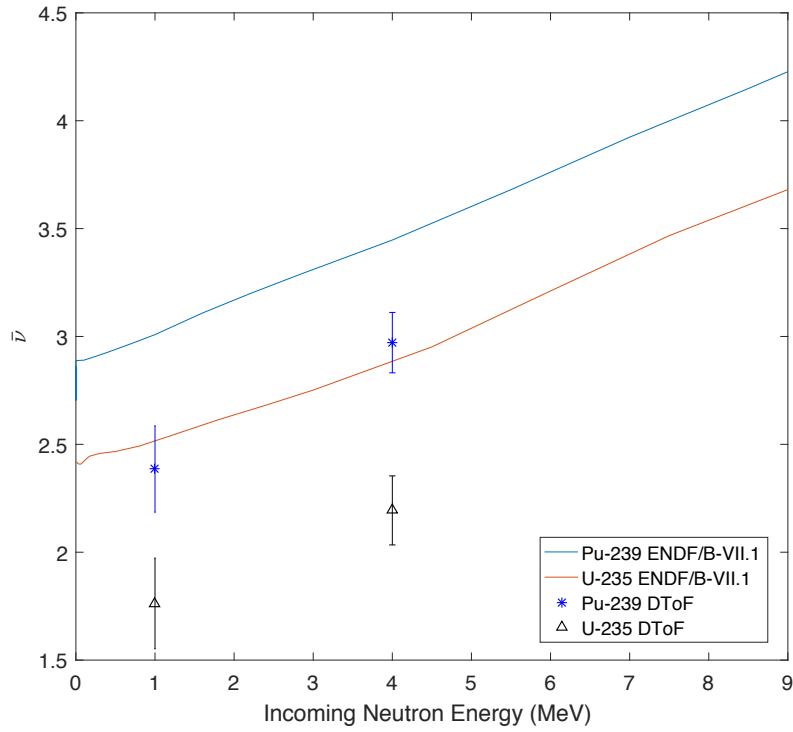


Figure 4.7: $\bar{\nu}$ measurements of the DToF detection system.

Chapter 5

$\Delta E/\Delta E$ Diamond Detector

5.1 Introduction

The NSRL accelerates a high energy beam of ions and can be used as a surrogate to Galactic Cosmic Rays (GCR) for shielding studies related to future space missions. The beam strikes thick targets and either escapes or is fully stopped within the shielding material. Moreover, the massive interactions between energetic ion projectiles and shielding nuclei produce fragments. Neutrons, protons, deuterons, tritons, and alpha particles are the most frequently produced particles [71]. In order to define those fragments, a $\Delta E/\Delta E$ diamond detector system measurement was conducted experimentally. The measured spectra were analyzed through comparison to Geant4 simulation.

5.2 Experimental Approach

The $\Delta E/\Delta E$ detection system consisted of two electronic grade SDDs (4 mm x 4 mm x 0.45 mm) set parallel to each other. Each SDD was mounted onto a previously designed PCB (see Section 3.4 for more details). The two PCBs were separated by 2 cm, and each connected to a CR-110 charge sensitive preamplifier. The preamplifiers and detector electronic boards were held in an aluminum enclosure, as Figure 5.1 indicates. The aluminum box was used both to reduce electromagnetic interference with detectors and to provide necessary protection [72].

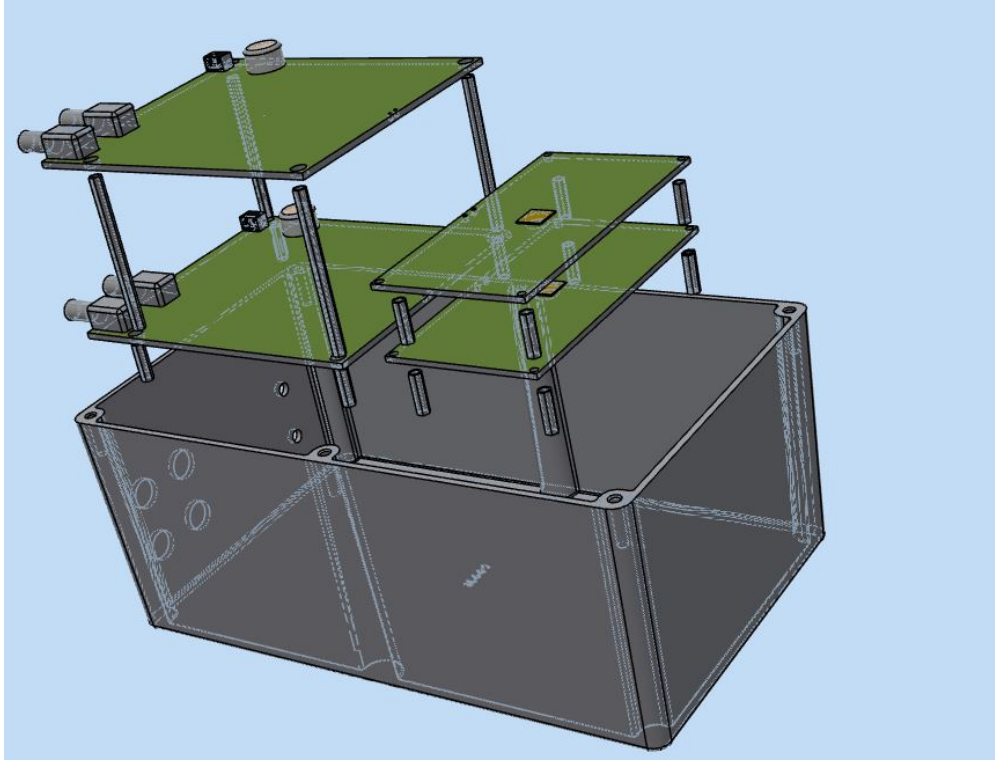


Figure 5.1: Layout of the $\Delta E/\Delta E$ detection system inside the aluminum enclosure.

After pre-amplification, each detector output signal was split into two pulses using a NSRL splitter. One pulse was delayed before being sent to the analog to digital converter (ADC); the other pulse was fed to a constant fraction discriminator (CFD) with a low-energy threshold for more accurate measurements. Both CFD outputs were fed into a fast-coincident module to represent a single type of particle that interacted with the two diamond sensors during a specific time period. The coincidence module produced two outputs: one pulse generated the trigger gate in the controller to start integrating the pulse while the other was delayed before being fed into an ADC. All ADC inputs were delayed to ensure that the pulses never reached the controller before the gate signal had arrived. Experimental data were recorded in list mode on an event-by-event basis and then displayed through a modified root framework. The schematic diagram of the electronics is presented in Figure 5.2. The NSRL beam spot size was 1 cm in diameter. Also, the beam had a Gaussian-distribution along the spot size. The beam struck two polyethylene targets. The up-stream target had an adjustable thickness (20, 40, or 60 g/cm^2) while the down-stream target had a fixed thickness (60 g/cm^2). Both targets were separated by 3.5 meters. The beam started with protons of

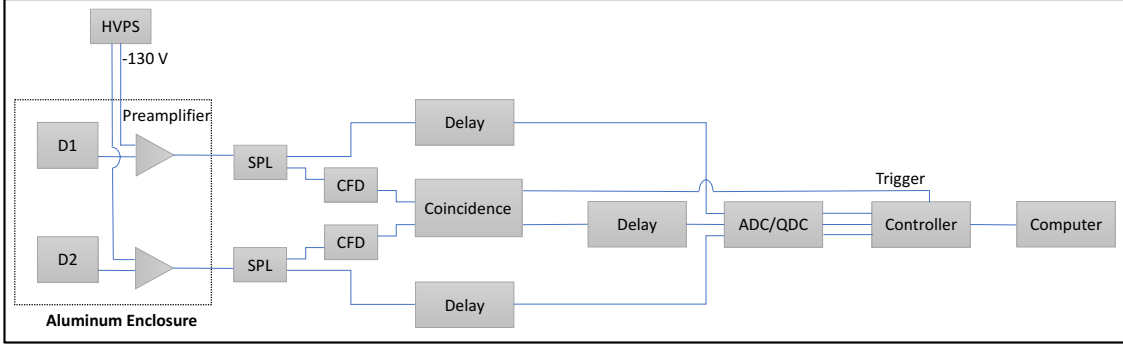


Figure 5.2: A schematic of the signal chain of the $\Delta E/\Delta E$ detection system.

energy 400, 800, and 2500 MeV. Heavier ions (Fe, He) were also accelerated. Each ion beam ran for almost 24 hours. All measured beams using the $\Delta E/\Delta E$ detection system are listed in Table 5.1 and provided in Appendix A. Only the first four runs were analyzed through comparison to a Geant4 simulation.

The $\Delta E/\Delta E$ detection system suited into two different locations based on beam projectile and energy. The detection system was placed along the beam axis behind the down-stream target (position 1) for high energetic protons (2500 and 800 MeV) because both projectiles could penetrate both targets. On the other hand, the $\Delta E/\Delta E$ system was placed in position 2 (45° off beam axis) for 400 MeV protons and heavier particles projectiles because they either fully stopped within the targets or provided an inconsiderable count rate in position 1. The two experimental arrangements are shown in Figure 5.3.

The coincidence mode was activated in position 1 in order to record only double interactions of single particle with the two detectors. However, due to the expected low count rates in position 2, the coincidence mode was disabled and pulse height spectra were

Table 5.1: $\Delta E/\Delta E$ detection system recorded runs.

Run No.	Beam Ion	Energy (MeV/nucleon)
1	Proton	2500
2	Proton	800
3	Proton	400
4	Fe	400
5	Fe	800
6	Fe He	1474 400,800

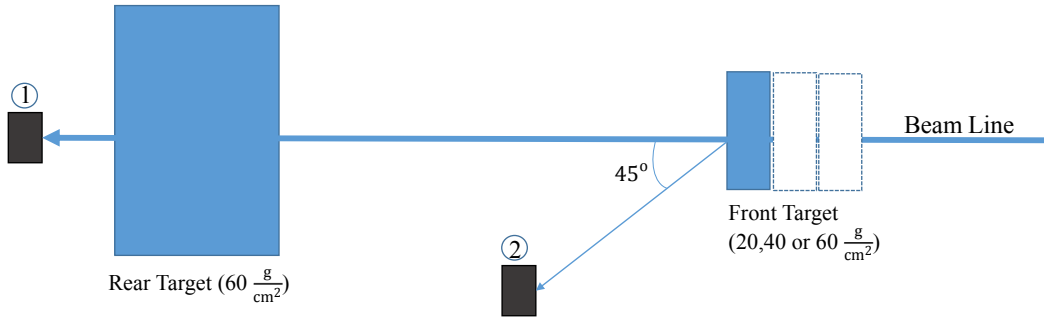


Figure 5.3: $\Delta E/\Delta E$ experimental arrangements.

recorded for each diamond whether the signals were correlated or not. Figure 5.4 depicts the aluminum enclosure suited in position 2 at the NSRL facility.

5.3 Geant4 Simulation

Geant4 is a Monte Carlo simulation for tracking particles based on C++ language and developed by RD44 collaboration. Geant4 has an advantage over MCNP in that it is capable of displaying all different interacted isotopes, which leads to a better spectrum analysis. In addition, the Geant4 simulation was developed for high-energy tracking physics experiments and has many libraries for those type of experiments [73].

A previous Geant4 simulation from the LHC was modified; the original hardonic simulation (Hard06) is available from Reference [74]. Adjustments included: the detector construction and physics list. The modified Geant4 simulation included the dimensions of the NSRL beam line room, as provided in Reference [75]. However, only the detection system, polyethylene targets, concrete wall, and floor were modeled. In the physics list file, the Bertini intra-nuclear cascade model with high precision neutron energies, lower than 20 MeV, was applied to simulate energetic ion interactions for all projectiles [76]. In addition, G4Lfission was used to implement neutron fission with nuclei. Located 70 cm from the front target, each projectile beam was simulated as a pencil beam and mono-energetic point source.

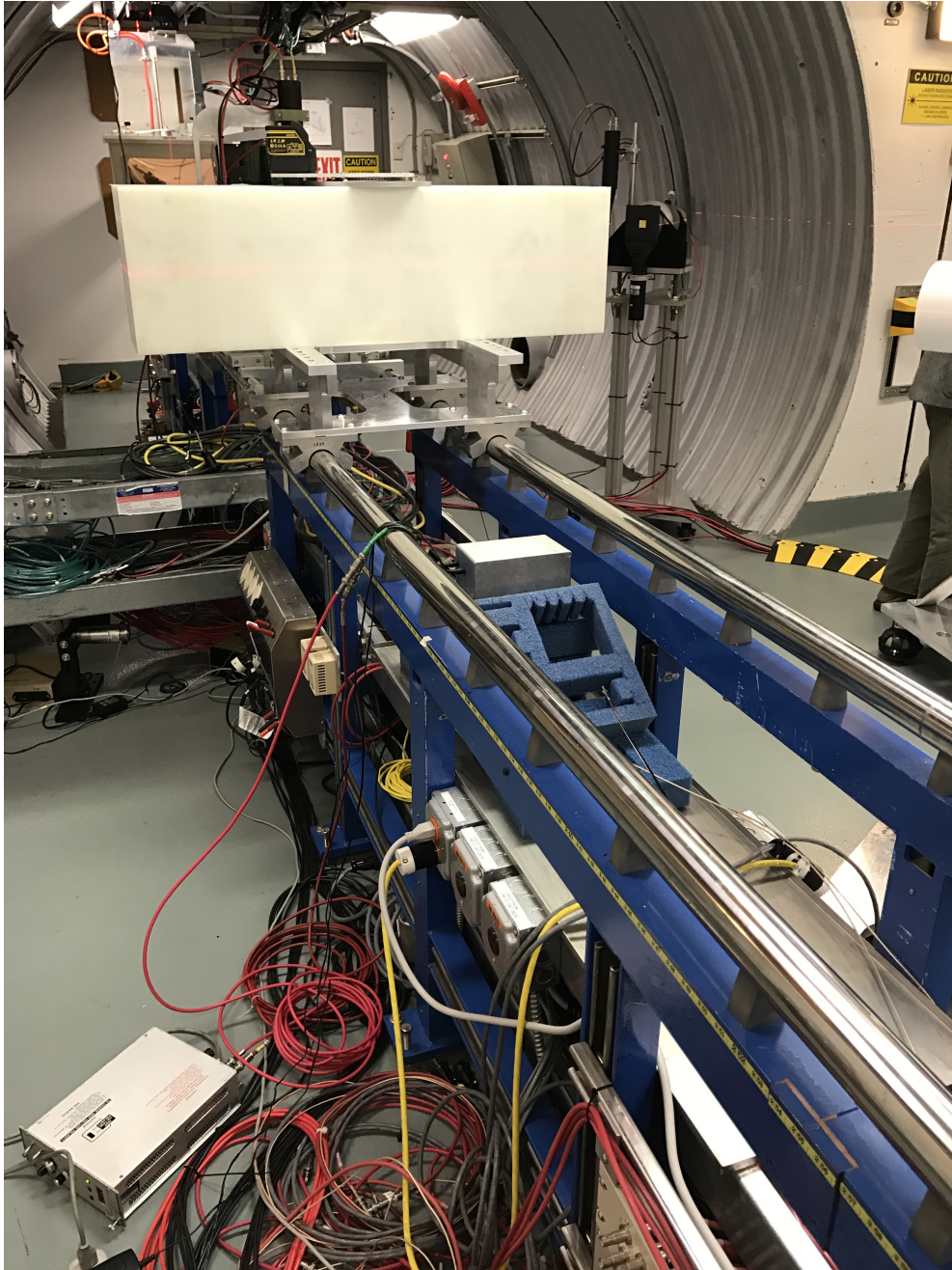


Figure 5.4: $\Delta E/\Delta E$ detection system located in position 2 at the NSRL beam room.

The simulation code generated two output files. The first indicated that all coincidence particles interacted with both diamonds. Moreover, the file included the type of particle, interaction timing, and energy deposition in each detector. On the other hand, pulse height spectrum information (the interacted particle type and deposited energy) in the first diamond detector only was printed out in the second output file. Simulated spectra of Geant4 code were normalized and binned according to experimental measurements. Furthermore, a minimum energy deposition was applied in the Matlab code to match CFD module threshold value.

5.4 Results

Matching measured and simulated spectra was the first step to analyze the data. Furthermore, the simulated 800 MeV proton beam pulse height spectrum of both SDDs were compared, as indicated in Figure 5.5a. The simulated $\Delta E/\Delta E$ was plotted as well to compare it to experimental work. It is evident that the simulated spectra in the two detectors are nearly identical. On the other hand, the measured spectra of the same projectile show significant dissimilarity (see Figure 5.5b). The second diamond spectrum could be affected by spray of energetic delta electrons because the two diamonds were too close to each other. Thus, the $\Delta E/\Delta E$ system orientation was changed and the same spectrum was observed. By comparing simulated and experimental results, the first SDD spectrum agrees well with simulation results. However, the second diamond pulse height spectrum shows significant variation. Expected reasons for differences are poor metal contact of the second diamond along with dysfunctionality of one or more of the modules in the electronic chain of the second SDD. Because of huge variation of second diamond pulse height spectrum with Geant4 results, only first diamond measurements were evaluated through the Geant4 simulation.

5.4.1 Position 1 Measurements

The usage of different thicknesses for the up-stream target generated many peaks in the measured spectra due to the increase in slower ions energy deposition, as seen in Figure 5.6. Moreover, high rates of secondary particles were recorded for the thickest target of

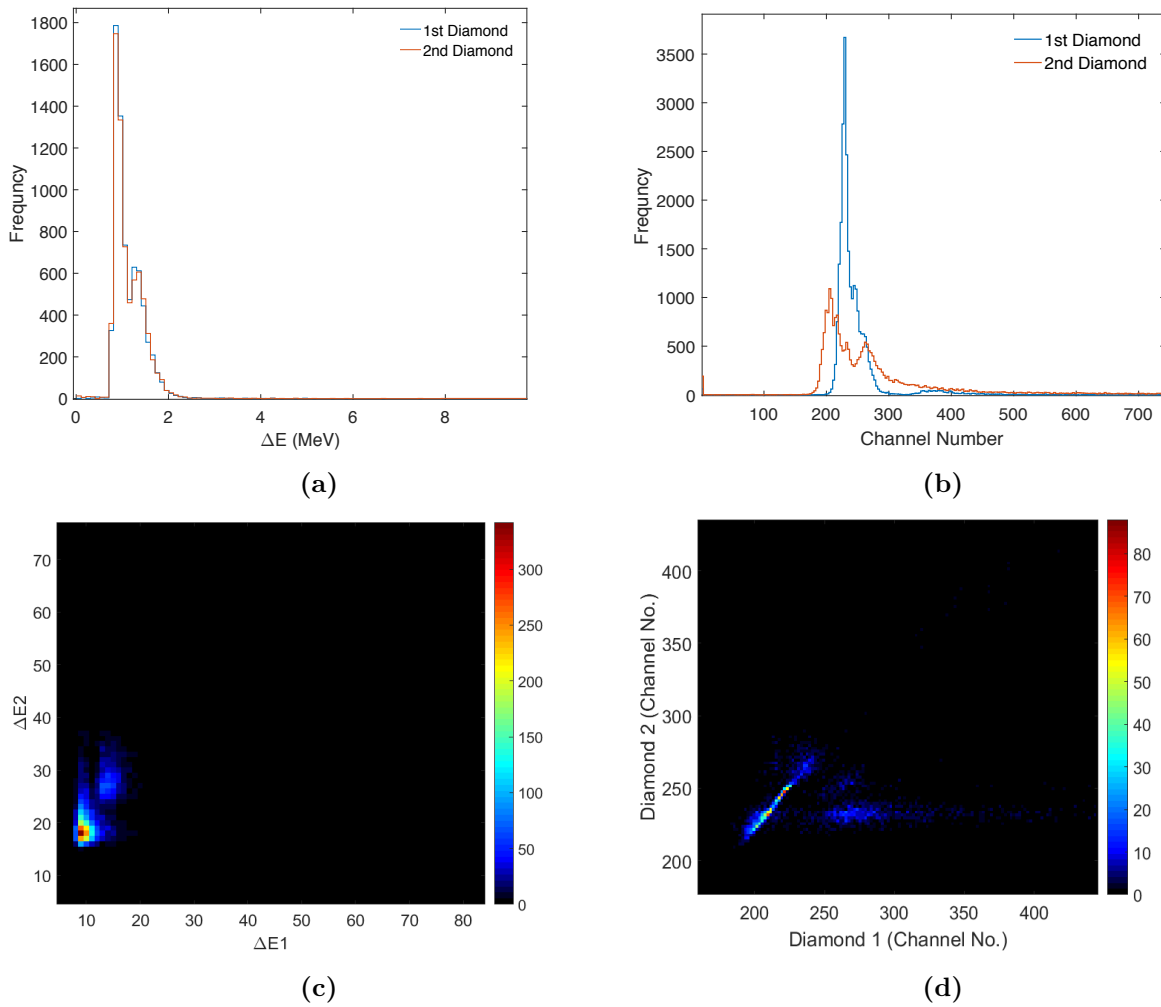


Figure 5.5: 800 MeV proton beam (a) Geant4 simulation spectra (b) experimental measured spectra (c) simulated $\Delta E/\Delta E$ measurements and (d) experimental $\Delta E/\Delta E$.

up-stream object (60 g/cm^2) due to the high rate of liberated particles. Additionally, since a 2.5 GeV proton beam is an extremely energetic beam, the simulated energy depositions in all thicknesses are almost similar (Figure 5.6b), the interacted particles being energetic enough to be located at the lowest region of the stopping power curve based on NIST data [77]. Nevertheless, the simulated spectra show lower peaks than the experimental results because of the slight variation of diamond detector location and simple simulated geometry of the Geant4 code.

To gauge the interacted charged particles, histograms of the secondary particles and projectiles that interacted with the diamond detector were plotted in Figure 5.7. Proton, pion, electron, and positron particles were observed. In fact, it was found that a proton was the dominant interacted particle and represents more than 95% of the spectrum counts. Pion, electron, and positron particles, on the other hand, mostly contributed to the lowest energy region of the spectrum.

5.4.2 Position 2 Measurements

As indicated in Figure 5.8 the measurement of the 400 MeV proton beam resulted in one high peak. The spectrum generated mainly from the interaction of the proton beam with the lowest thickness (20 g/cm^2) of up-stream polyethylene target. The other two thicknesses of the front target resulted in considerably high counts of light-charged particles located in the lowest energy spectrum region.

The $\Delta E/\Delta E$ system observed more ion species than Position 1 measurements since coincidence mode was deactivated. Detection of light and heavy ions indicated fast neutron interactions (scattering and absorption) with carbon atom. The observed neutron-induced ions are deuterium (^2H), ^3He , α , ^{11}B , and ^{12}C . Nevertheless, their contribution is insignificant to the simulated spectrum. Other liberated particles such as pion, electron, and positron were observed as well, as displayed in Figure 5.9.

Geant4 simulations were extended to measure the ToF of the light ion interaction between the two detectors and energy deposition in the first diamond detector. The simulation indicated the feasibility of such a measurement to differentiate between hydrogen species, as seen in Figure 5.10.

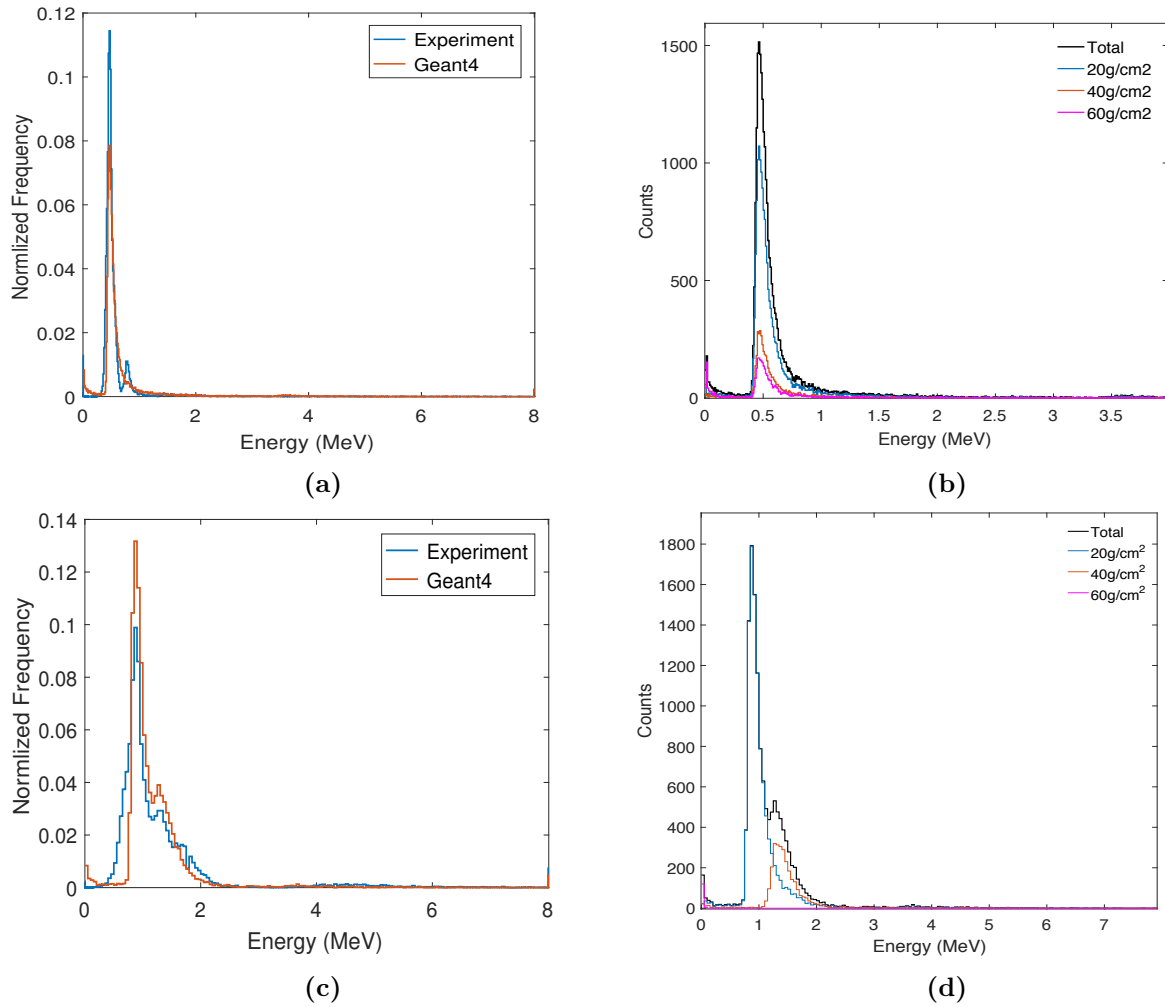
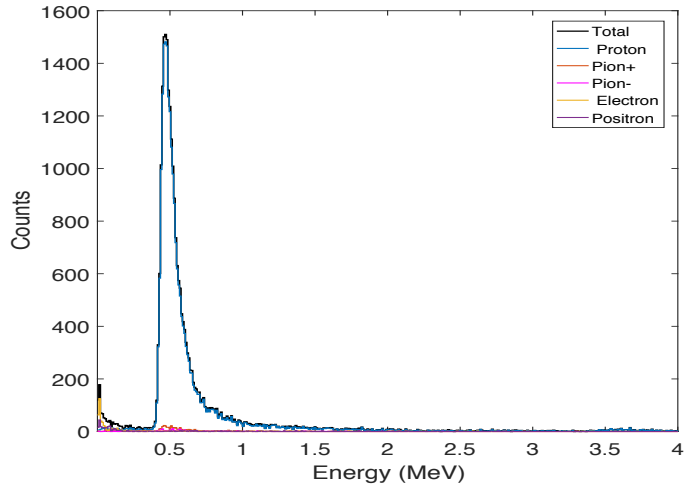
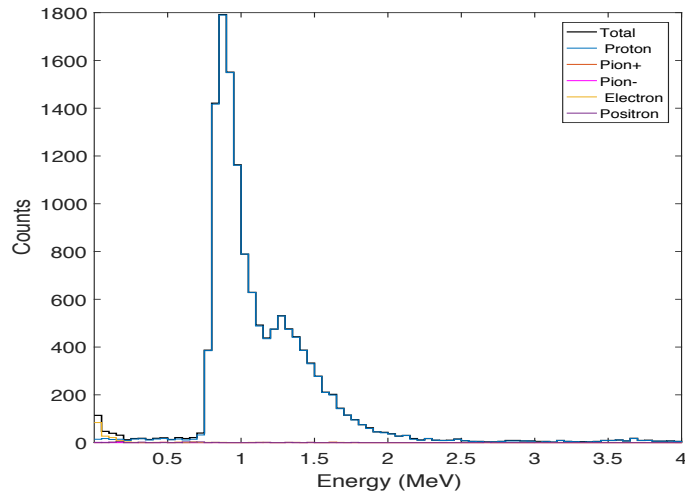


Figure 5.6: Experimental versus simulation spectra for (a) 2.5 GeV and (c) 800 MeV proton beams. Simulated spectra for different upstream target thicknesses of (b) 2.5 GeV and (d) 800 MeV proton projectiles.



(a)



(b)

Figure 5.7: Interacted particles with first diamond detector for proton beams (a) 2.5 GeV and (b) 800 MeV

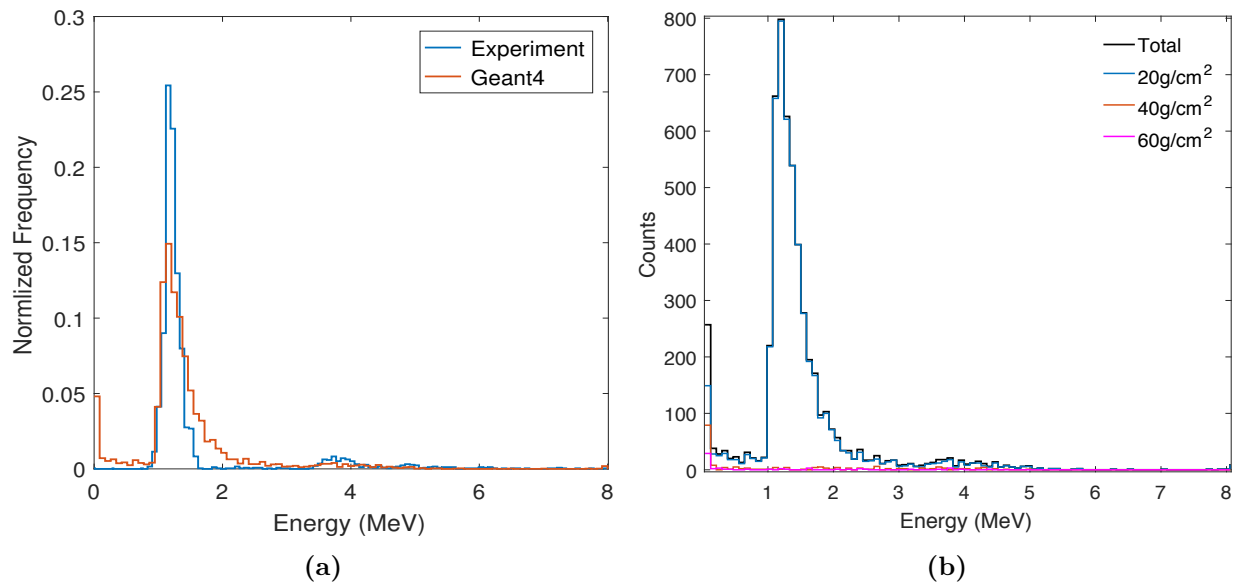


Figure 5.8: (a) 400 MeV beam measurements and experimental results. (b) Simulated spectra of 400 MeV proton beam for all upstream target thicknesses.

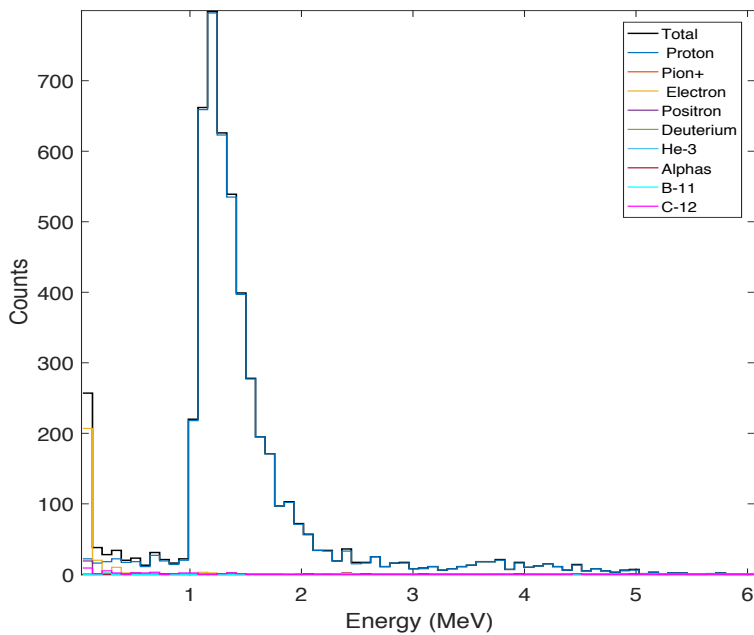


Figure 5.9: First diamond detector interacted particles of 400 MeV proton beam.

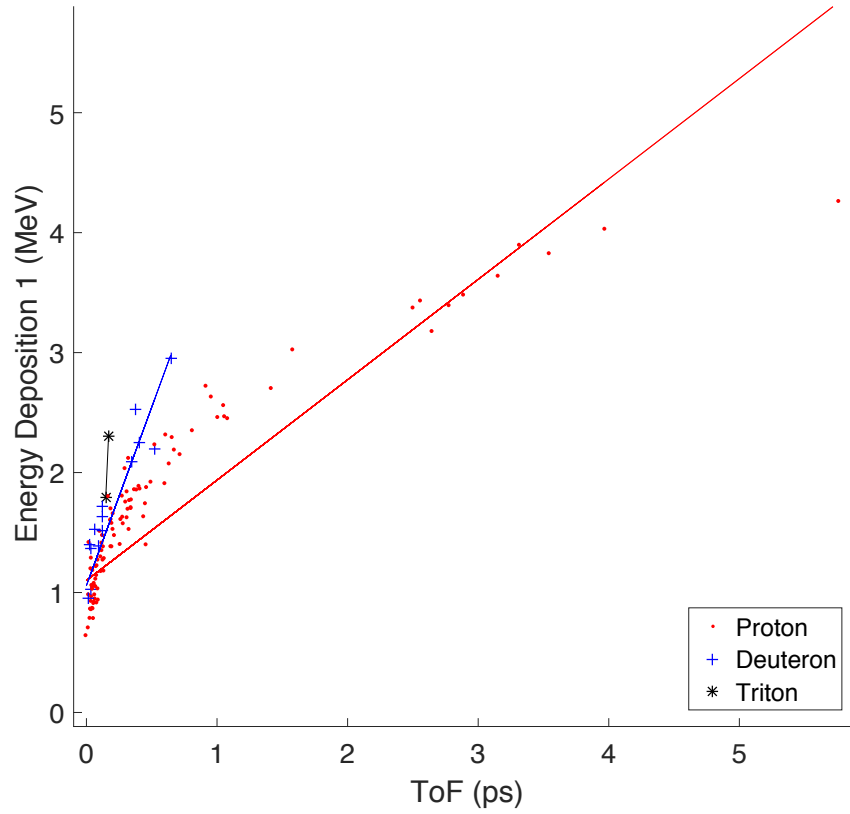


Figure 5.10: Identification of hydrogen isotopes ion using ToF and $\Delta E1$ for Fe-400 AMeV simulated projectile.

As evidenced by the figure above, the differentiating resolution between isotopes species increased for lower energy particles (higher deposited energy and ToF).

Chapter 6

Conclusions and Future Work

6.1 Conclusions

The fast signal response of CVD diamonds make DNSC very useful in ToF applications. Because of the variation of both the total and differential neutron elastic-scattering cross-sections with carbon, the correction method used with DNSC is an essential tool for finding the correct neutron source spectrum. The capability of the DNSC in reconstructing spectra and localizing neutron incident sources is demonstrated both computationally and experimentally.

The two diamond array NSC shows a better reconstructed spectrum compared to recent studies of a plastic scintillator NSC. The simulation results of two diamond array NSC identified ^{252}Cf and $^{239}\text{Pu-Be}$ neutron sources with high accuracy ($\approx 93\%$). The 16-pixel, two diamond array system indicates good agreement with the neutron incident source spectra and a significant improvement in detection efficiency, by one order of a magnitude, when compared to a similar system with non-pixelated diamond sensors. As expected, angular and depth uncertainties play an important role in defining energy resolution. The experimental result of the two-diamond system reveals all characteristic peaks of the $^{239}\text{Pu-Be}$ neutron source. In particular, the measurements matched the source peaks of 3 and 10 MeV. However, the reconstructed spectrum shows statistical fluctuations because of the low count rate of the detection system.

The computational results of the diamond array NSC indicate the systems capability to accurately locate multiple neutron sources in different scenarios. Moreover, the system defines the 3D-position coordinates of all simulated scenarios and adequately reconstructs the neutron spectra of ^{252}Cf and $^{239}\text{Pu-Be}$. The compact size of the diamond array NSC ($5 \times 5 \times 5 \text{ cm}^3$), with the advantage of radiation hardness, makes it a ideal system for reconstructing the neutron spectrum and imaging with high luminosity environment such as nuclear reactors.

The DToF system simulation results indicate good spectroscopy efficiency of the reconstructed prompt neutron spectra. The prompt neutron spectra are reconstructed for two actinides ^{235}U and ^{239}Pu and are modified using correction factors based on the neutron cross-section with carbon atom. However, a new correction technique is required for high-accuracy measurements. Additionally, DToF demonstrates the neutron multiplicity factors of both ^{235}U and ^{239}Pu -coated targets up to 5 neutrons. However, due to the overall detection efficiency ($\approx 3\%$) of the DToF, multiplication factors for more than two neutrons have unreasonable probability values. Consequently, the low detection efficiency results in a low multiplicity average neutron number ($\bar{\nu}$), after modification, for each incoming neutron and target.

The measured spectra of the SDDs in the $\Delta E/\Delta E$ diamond-detector system indicate that the first SDD has good agreement with computational results. However, the second SDD exhibited poor response due to the poor metallization of the contact and/or an electronic device in the experiment setup. From experiment results, the $\Delta E1$ measurements with no ToF information make defining interacted ions impractical. However, the expected ability to detect and identify the different isotopes of the $\Delta E/\Delta E$ diamond-detector system is proven computationally. The simulated detection system recognizes different isotopes of hydrogen. These results might be validated in an energetic-ion beamline facility by using fast electronics (a fast-shaping amplifier and high-sampling rate digitizer) to differentiate between particles via ToF of the interacted particle and $\Delta E1$ measurements. As stated in the results section, the proposed system would identify low energy ions more accurately than fast interacted ions because of the increase of both energy deposition and ToF.

6.2 Future Work

This dissertation work could be extended and enhanced in various ways. First, by using the same setup and procedure discussed in section 3.6, one could perform the two-diamond array experiment to validate the capability of demonstrating the neutron spectrum of a ^{252}Cf source in a lab. However, the measurements would take a longer time (two months) because the ^{252}Cf neutron source has a lower neutron yield ($\approx 10^4$ n/s) than the ^{239}Pu -Be source.

The design of the algorithm for the diamond-array system depends mainly on the user to define the image with the highest resolution. Even though the image construction algorithm localizes the neutron sources with high precision, a machine-learning algorithm needs to be implemented to automatically define the distance(Y) to the neutron source. Hence, the code generated the spectrum of the neutron source with the 3D coordinates for each configuration listed in Table 3.2. To increase the spectroscopy resolution of the system, a new algorithm could be added to the machine-learning code to define the true neutron source spectrum based on the modified spectrum.

Extending the capability of the diamond-array system by simulating four arrays instead of two is another recommended future project. In this updated simulation, the neutron source spectrum would be reconstructed by the interaction of the incident neutron in any two pixels of the system. In this model, we might have a 360° -view around the system.

The diamond-array system might be built experimentally using only four pixelated diamonds in each panel. However, this could be done using 16 different combinations of only two pixelated diamonds (each with 16 pixels) with 32 charge-sensitive preamplifiers. Furthermore, an aluminum frame would be necessary to hold the detectors in the correct locations for each geometrical setup. A diamond detector would be needed for each panel, but the configuration of the two diamonds would have to be changed every 1-2 days, with each orientations time frame depending on the source activity. For instance, if the system required a day for each orientation, finishing all the necessary configurations would require 16 days. The system would be used to indicate the feasibility of neutron source localization only.

Due to the isotopes discrimination capability that was demonstrated by the Geant4 simulation for the $\Delta E/\Delta E$ system, the detection system could be utilized again in an energetic beam-line with the CIVIDEC C6 fast amplifiers and the CAEN digitizer. Unlike the performed $\Delta E/\Delta E$ in this dissertation, the reading would have to be recorded separately for each thickness of the up-stream targets.

Bibliography

- [1] J. Webster, T. Grimes, B. Archambault, K. Fischer, N. Kostry, A. Lentner, J. Lapinskas, and R. Taleyarkhan, “Beyond he-3 nuclear sensors?tmfdfs for real-time snm monitoring with directionality,” in *Technologies for Homeland Security (HST), 2011 IEEE International Conference on*, pp. 372–378, IEEE, 2011. 1
- [2] G. F. Knoll, *Radiation detection and measurement*. John Wiley & Sons, 2010. 1, 24, 28
- [3] G. Schmid, J. Koch, R. Lerche, and M. Moran, “A neutron sensor based on single crystal cvd diamond,” *Nuclear Instruments and Methods in Physics Research Section A: Accelerators, Spectrometers, Detectors and Associated Equipment*, vol. 527, no. 3, pp. 554–561, 2004. 1, 17
- [4] B. A. Perdue, “Modeling neutron-scattering backgrounds in the chi-nu detector array,” tech. rep., Los Alamos National Laboratory (LANL), 2011. 2
- [5] R. Balmer, J. Brandon, S. Clewes, H. Dhillon, J. Dodson, I. Friel, P. Inglis, T. Madgwick, M. Markham, T. Mollart, *et al.*, “Chemical vapour deposition synthetic diamond: materials, technology and applications,” *Journal of Physics: Condensed Matter*, vol. 21, no. 36, p. 364221, 2009. 3
- [6] E. S. Ltd, “The element six cvd diamond handbook.” Available at https://e6cvd.com/media/wysiwyg/pdf/E6_CVD_Diamond_Handbook_A5_v10X.pdf, 2006. 3, 4, 5, 18
- [7] F. Bundy, H. T. Hall, H. Strong, and R. W. Jun, “Man-made diamonds,” *nature*, vol. 176, no. 4471, p. 51, 1955. 3
- [8] P. M. Martineau, S. C. Lawson, A. J. Taylor, S. J. Quinn, D. J. Evans, and M. J. Crowder, “Identification of synthetic diamond grown using chemical vapor deposition (cvd),” *Gems & Gemology*, vol. 40, no. 1, pp. 2–25, 2004. 3, 4
- [9] J. Isberg, J. Hammersberg, E. Johansson, T. Wikström, D. J. Twitchen, A. J. Whitehead, S. E. Coe, and G. A. Scarsbrook, “High carrier mobility in single-crystal plasma-deposited diamond,” *Science*, vol. 297, no. 5587, pp. 1670–1672, 2002. 4, 5

- [10] S. Michimasa, M. Takaki, M. Dozono, S. Go, H. Baba, E. Ideguchi, K. Kisamori, H. Matsubara, H. Miya, S. Ota, *et al.*, “Development of cvd diamond detector for time-of-flight measurements,” *Nuclear Instruments and Methods in Physics Research Section B: Beam Interactions with Materials and Atoms*, vol. 317, pp. 710–713, 2013. 4, 26
- [11] M. Friedl, *Diamond detectors for ionizing radiation*. PhD thesis, Austrian Academy of Sciences, 1999. 4
- [12] W. De Boer, J. Bol, A. Furgeri, S. Müller, C. Sander, E. Berdermann, M. Pomorski, and M. Huhtinen, “Radiation hardness of diamond and silicon sensors compared,” *physica status solidi (a)*, vol. 204, no. 9, pp. 3004–3010, 2007. 5
- [13] N. Randazzo, S. Aiello, G. Chiodini, G. A. Cirrone, G. Cuttone, M. De Napoli, V. Giordano, S. Kwan, E. Leonora, F. Longhitano, *et al.*, “Comparative timing performances of s-cvd diamond detectors with different particle beams and readout electronics,” in *Nuclear Science Symposium and Medical Imaging Conference (NSS/MIC), 2012 IEEE*, pp. 1949–1951, IEEE, 2012. 5
- [14] W. A. Yarbrough and R. Messier, “Current issues and problems in the chemical vapor deposition of diamond,” *Science*, vol. 247, no. 4943, pp. 688–696, 1990. 5
- [15] C. Bauer, I. Baumann, C. Colledani, J. Conway, P. Delpierre, F. Djama, W. Dulinski, A. Fallou, K. Gan, R. Gilmore, *et al.*, “Recent results from the rd42 diamond detector collaboration,” *Nuclear Instruments and Methods in Physics Research Section A: Accelerators, Spectrometers, Detectors and Associated Equipment*, vol. 383, no. 1, pp. 64–74, 1996. 5
- [16] N. Tranchant, M. Nesladek, D. Tromson, Z. Remes, A. Bogdan, and P. Bergonzo, “Time of flight study of high performance cvd diamond detector devices,” *physica status solidi (a)*, vol. 204, no. 9, pp. 3023–3029, 2007. 5

- [17] E. Lukosi, *Theoretical and experimental investigations in characterizing and developing multiplexed diamond-based neutron spectrometers*. PhD thesis, University of Missouri–Columbia, 2012. 5, 10, 22, 29
- [18] J. Chadwick, “The existence of a neutron,” *Proceedings of the Royal Society of London. Series A*, vol. 136, no. 830, pp. 692–708, 1932. 6
- [19] J. J. Duderstadt and L. J. Hamilton, *Nuclear reactor analysis*, vol. 1. Wiley New York, 1976. 6, 50
- [20] Z. Ge, Z. Zhao, H. Xia, Y. Zhuang, T. Liu, J. Zhang, and H. Wu, “The updated version of chinese evaluated nuclear data library (cendl-3.1),” *J. Korean Phys. Soc.*, vol. 59, no. 2, pp. 1052–1056, 2011. 6, 21
- [21] N. Tsoufanidis, *Measurement and detection of radiation*. CRC press, 2013. 7, 27, 28, 56
- [22] A. Zimbal, L. Giacomelli, R. Nolte, and H. Schuhmacher, “Characterization of monoenergetic neutron reference fields with a high resolution diamond detector,” *Radiation Measurements*, vol. 45, no. 10, pp. 1313–1317, 2010. 7
- [23] M. Pillon, M. Angelone, A. Krása, A. Plompen, P. Schillebeeckx, and M. Sergi, “Experimental response functions of a single-crystal diamond detector for 5–20.5 mev neutrons,” *Nuclear Instruments and Methods in Physics Research Section A: Accelerators, Spectrometers, Detectors and Associated Equipment*, vol. 640, no. 1, pp. 185–191, 2011. 7, 8, 9
- [24] M. Rebai, A. Milocco, L. Giacomelli, E. P. Cippo, M. Tardocchi, A. Fazzi, A. Pietropaolo, and G. Gorini, “Response of a single-crystal diamond detector to fast neutrons,” *Journal of Instrumentation*, vol. 8, no. 10, p. P10007, 2013. 8
- [25] C. Cazzaniga, E. A. Sundén, F. Binda, G. Croci, G. Ericsson, L. Giacomelli, G. Gorini, E. Griesmayer, G. Grosso, G. Kaveney, *et al.*, “Single crystal diamond detector measurements of deuterium-deuterium and deuterium-tritium neutrons in

- joint european torus fusion plasmas,” *Review of Scientific Instruments*, vol. 85, no. 4, p. 043506, 2014. 8, 9
- [26] D. W. Anderson, *Absorption of ionizing radiation*. University Park Press, 1984. 9
- [27] H. A. Bethe, “Nuclear physics b. nuclear dynamics, theoretical,” *Reviews of Modern Physics*, vol. 9, no. 2, p. 69, 1937. 9
- [28] M. Pomorski, E. Berdermann, A. Caragheorghopol, M. Ciobanu, M. Kiš, A. Martemiyarov, C. Nebel, and P. Moritz, “Development of single-crystal cvd-diamond detectors for spectroscopy and timing,” *physica status solidi (a)*, vol. 203, no. 12, pp. 3152–3160, 2006. 10, 11, 25
- [29] K. Ogasawara, T. Broiles, K. Coulter, M. Dayeh, M. Desai, S. Livi, D. McComas, and B. Walther, “Single crystal chemical vapor deposit diamond detector for energetic plasma measurement in space,” *Nuclear Instruments and Methods in Physics Research Section A: Accelerators, Spectrometers, Detectors and Associated Equipment*, vol. 777, pp. 131–137, 2015. 10
- [30] W. Trischuk, R. Collaboration, *et al.*, “Diamond particle detectors for high energy physics,” *Nuclear and Particle Physics Proceedings*, vol. 273, pp. 1023–1028, 2016. 11
- [31] L. Fernandez-Hernando, D. Chong, R. Gray, C. Ilgner, A. Macpherson, A. Oh, T. Pritchard, R. Stone, and S. Worm, “Development of a cvd diamond beam condition monitor for cms at the large hadron collider,” *Nuclear Instruments and Methods in Physics Research Section A: Accelerators, Spectrometers, Detectors and Associated Equipment*, vol. 552, no. 1, pp. 183–188, 2005. 11
- [32] M. Mathes, M. Cristinziani, H. Kagan, S. Smith, W. Trischuk, J. Velthuis, and N. Wermes, “Characterization of a single crystal diamond pixel detector in a high energy particle beam,” *Journal of Instrumentation*, vol. 3, no. 12, p. P12002, 2008. 11
- [33] M. Červ, “The atlas diamond beam monitor,” *Journal of Instrumentation*, vol. 9, no. 02, p. C02026, 2014. 11

- [34] S. Lagomarsino, M. Bellini, C. Corsi, S. Fanetti, F. Gorelli, I. Lontos, G. Parrini, M. Santoro, and S. Sciortino, “Electrical and raman-imaging characterization of laser-made electrodes for 3d diamond detectors,” *Diamond and Related Materials*, vol. 43, pp. 23–28, 2014. 11
- [35] I. H. McLaren and W. C. Wiley, “Mass spectrometer,” Apr. 24 1956. US Patent 2,743,370. 12
- [36] N. J. Carron, *An introduction to the passage of energetic particles through matter*. CRC Press, 2006. 12
- [37] A. Smith, P. Fields, and J. Roberts, “Spontaneous fission neutron spectrum of cf 252,” *Physical Review*, vol. 108, no. 2, p. 411, 1957. 12
- [38] J. E. Turner, “Atoms, radiation, and radiation protection,” *Atoms, Radiation, and Radiation Protection, 2nd Edition, by James E. Turner, pp. 576. ISBN 0-471-59581-0. Wiley-VCH, April 1995.*, p. 576, 1995. 13
- [39] H. R. Bowman, S. G. Thompson, J. Milton, and W. J. Swiatecki, “Velocity and angular distributions of prompt neutrons from spontaneous fission of cf 252,” *Physical Review*, vol. 126, no. 6, p. 2120, 1962. 13
- [40] N. Mascarenhas, J. Brennan, K. Krenz, J. Lund, P. Marleau, J. Rasmussen, J. Ryan, and J. Macri, “Development of a neutron scatter camera for fission neutrons,” in *Nuclear Science Symposium Conference Record, 2006. IEEE*, vol. 1, pp. 185–188, IEEE, 2006. 13, 17
- [41] M. L. Roush, M. Wilson, and W. F. Hornyak, “Pulse shape discrimination,” *Nuclear Instruments and Methods*, vol. 31, no. 1, pp. 112–124, 1964. 13
- [42] J. Brennan, E. Brubaker, R. Cooper, M. Gerling, C. Greenberg, P. Marleau, N. Mascarenhas, and S. Mrowka, “Measurement of the fast neutron energy spectrum of an ^{241}Am -Be source using a neutron scatter camera,” *IEEE Transactions on Nuclear Science*, vol. 58, no. 5, pp. 2426–2430, 2011. 14, 15

- [43] N. Mascarenhas, J. Brennan, K. Krenz, P. Marleau, and S. Mrowka, “Results with the neutron scatter camera,” *IEEE Transactions on Nuclear Science*, vol. 56, no. 3, pp. 1269–1273, 2009. 15, 16
- [44] N. Mascarenhas, P. Marleau, M. Gerling, R. L. Cooper, S. Mrowka, and J. S. Brennan, “Method for improving the angular resolution of a neutron scatter camera,” Dec. 25 2012. US Patent 8,338,795. 15
- [45] J. S. Brennan, E. Brubaker, M. D. Gerling, P. Marleau, S. Mrowka, and J. T. Steele, “Recent investigations using the neutron scatter camera,” tech. rep., Sandia National Laboratories (SNL-CA), Livermore, CA (United States), 2012. 15
- [46] K. Weinfurter, J. Mattingly, E. Brubaker, and J. Steele, “Model-based design evaluation of a compact, high-efficiency neutron scatter camera,” *Nuclear Instruments and Methods in Physics Research Section A: Accelerators, Spectrometers, Detectors and Associated Equipment*, vol. 883, pp. 115–135, 2018. 15, 16
- [47] R. C. Runkle, A. Bernstein, and P. Vanier, “Securing special nuclear material: Recent advances in neutron detection and their role in nonproliferation,” *Journal of Applied Physics*, vol. 108, no. 11, p. 13, 2010. 17, 50
- [48] J. T. Goorley, M. R. James, T. E. Booth, F. B. Brown, J. Bull, L. J. Cox, J. Durkee, J. Elson, M. Fensin, R. Forster, *et al.*, “Initial mcnp6 release overview-mcnp6 version 1.0,” *Los Alamos National Laboratory, Los Alamos, NM, LA-UR-13-22934*, vol. 1, 2013. 18, 19
- [49] M. Chadwick, M. Herman, P. Obložinský, M. E. Dunn, Y. Danon, A. Kahler, D. L. Smith, B. Pritychenko, G. Arbanas, R. Arcilla, *et al.*, “Endf/b-vii. 1 nuclear data for science and technology: cross sections, covariances, fission product yields and decay data,” *Nuclear data sheets*, vol. 112, no. 12, pp. 2887–2996, 2011. 18
- [50] R. J. McConn, C. J. Gesh, R. T. Pagh, R. A. Rucker, and R. Williams III, “Compendium of material composition data for radiation transport modeling,” tech. rep., Pacific Northwest National Laboratory (PNNL), Richland, WA (US), 2011. 18

- [51] J. F. Briesmeister *et al.*, *MCNP—A general Monte Carlo code for neutron and photon transport*. Los Alamos National Laboratory Los Alamos, 1986. 18
- [52] B. Watt, “Energy spectrum of neutrons from thermal fission of u 235,” *Physical Review*, vol. 87, no. 6, p. 1037, 1952. 19
- [53] Z. R. Harvey, “Neutron flux and energy characterization of a plutonium-beryllium isotopic neutron source by monte carlo simulation with verification by neutron activation analysis,” Master’s thesis, University of Nevada, Las Vegas, 2010. 19
- [54] J. K. Shultis and R. E. Faw, *Fundamentals of Nuclear Science and Engineering Second Edition*. CRC press, 2007. 22, 24
- [55] P. E. Vanier, L. Forman, I. Dioszegi, C. Salwen, and V. J. Ghosh, “Calibration and testing of a large-area fast-neutron directional detector,” in *Nuclear Science Symposium Conference Record, 2007. NSS’07. IEEE*, vol. 1, pp. 179–184, IEEE, 2007. 24
- [56] M. S. Cetiner, *Development of an ion time-of-flight spectrometer for neutron depth profiling*. The Pennsylvania State University, 2008. 25, 26, 27
- [57] ORTEC, “Fast-timing discriminator.” Available at <http://www.ortec-online.com/-/media/ametektortec/other/fast-timing-discriminator-introduction.pdf?1a=en>, 2002. 26
- [58] T. RIU, “Cern courier archive: 1975,” *CERN Courier*, 2018. 26
- [59] S. Cova, M. Ghioni, and F. Zappa, “Optimum amplification of microchannel-plate photomultiplier pulses for picosecond photon timing,” *Review of scientific instruments*, vol. 62, no. 11, pp. 2596–2601, 1991. 27
- [60] R. Alig, S. Bloom, and C. Struck, “Scattering by ionization and phonon emission in semiconductors,” *Physical Review B*, vol. 22, no. 12, p. 5565, 1980. 27
- [61] T. G. Wulz, “Advanced radiation detection devices: 3d diamond detectors and ksr2i5: Eu scintillating crystals,” 2017. 29

- [62] M. Anderson, “Neutron energy spectra of ^{239}Pu , ^{238}Pu , and $^{238}\text{Pu}^{180}(\alpha, n)$ sources,” *MLM-1422, Mound Laboratory, Monsanto Research Corporation (October 31, 1967)*. 34, 38
- [63] F. T. Cooperation, “Standard californium-252 sources.” Available at <http://www.frontier-cf252.com/standard-californium-252-sources-model-100-series.html>, 2006. 38, 44, 49
- [64] M. Anderson and R. Neff, “Neutron energy spectra of different size ^{239}Pu (α, n) sources,” *Nuclear instruments and Methods*, vol. 99, no. 2, pp. 231–235, 1972. 39
- [65] G. M. Ghita, *Comprehensive modeling of special nuclear materials detection using three-dimensional deterministic and Monte Carlo methods*. University of Florida, 2008. 42
- [66] C. R. Brune, S. M. Grimes, D. C. Ingram, and T. N. Massey, “Neutron source capabilities at ohio university,” 2017. 47, 55
- [67] M. Martone, M. Angelone, and M. Pillon, “The 14 mev frascati neutron generator,” *Journal of nuclear materials*, vol. 212, pp. 1661–1664, 1994. 47
- [68] R. Haight, H. Lee, T. Taddeucci, J. O’Donnell, B. Perdue, N. Fotiades, M. Devlin, J. Ullmann, A. Laptev, T. Bredeweg, *et al.*, “The prompt fission neutron spectrum (pfns) measurement program at lances,” *Nuclear Data Sheets*, vol. 119, pp. 205–208, 2014. 50
- [69] A. Y. Konobeyev, U. Fischer, A. Koning, H. Leeb, S. Leray, and Y. Yariv, “What can we expect from the use of nuclear models implemented in mcnpx at projectile energies below 150 mev? detailed comparison with experimental data,” *Journal of the Korean Physical Society*, vol. 59, no. 2, pp. 927–930, 2011. 51
- [70] R. C. Haight, H. Y. Lee, S. M. Mosby, J. M. O’Donnell, C. J. Solomon Jr, T. N. Taddeucci, N. Fotiadis, M. J. Devlin, J. L. Ullmann, T. A. Bredeweg, *et al.*, “Chi-nu level 2 review,” tech. rep., Los Alamos National Laboratory (LANL), 2015. 55

- [71] T. Nakamura and L. Heilbronn, *Handbook on Secondary Particle Production and Transport by High-energy Heavy Ions:(with CD-ROM)*. World Scientific, 2006. 58
- [72] A. Alghamdi, L. Heilbronn, L. Castellanos, and E. Lukosi, “ δ_e / δ_e measurements of energetic ions using cvd diamond,” *Manuscript submitted for publication*. 58
- [73] R. Brun, R. Hagelberg, and M. Hansroul, *Geant, Simulation Program for Particle Physics Experiments; User Guide and Reference Manual*. CERN. Data Handling Division, 1978. 61
- [74] CERN, “Geant4 example hadr06.” Available at http://geant4.web.cern.ch/geant4/UserDocumentation/Doxygen/examples_doc/html/ExampleHadr06.html, 2013. 61
- [75] N. A. McGirl, L. A. Castellanos, A. P. Srikrishna, L. Heilbronn, C. La Tessa, A. Rusek, M. Sivertz, S. Blattnig, M. Cloudsley, T. Slaba, *et al.*, “Accelerator-based measurements relevant for shielding design in space,” in *Aerospace Conference, 2016 IEEE*, pp. 1–11, IEEE, 2016. 61
- [76] A. Heikkinen, “Implementing the bertini intra-nuclear-cascade in the geant4 hadronic framework,” *The Monte Carlo Method: Versatility Unbounded in a Dynamic Computing World, Chattanooga, Tennessee*, 2005. 61
- [77] M. J. Berger, “Estar, pstar, and astar: Computer programs for calculating stopping-power and range tables for electrons, protons, and helium ions,” *Unknown*, 1992. 65

Appendices

A $\Delta E/\Delta E$ detection system recorded runs.

All runs listed in Table 5.1 using $\Delta E/\Delta E$ detection system are provided in this appendix.

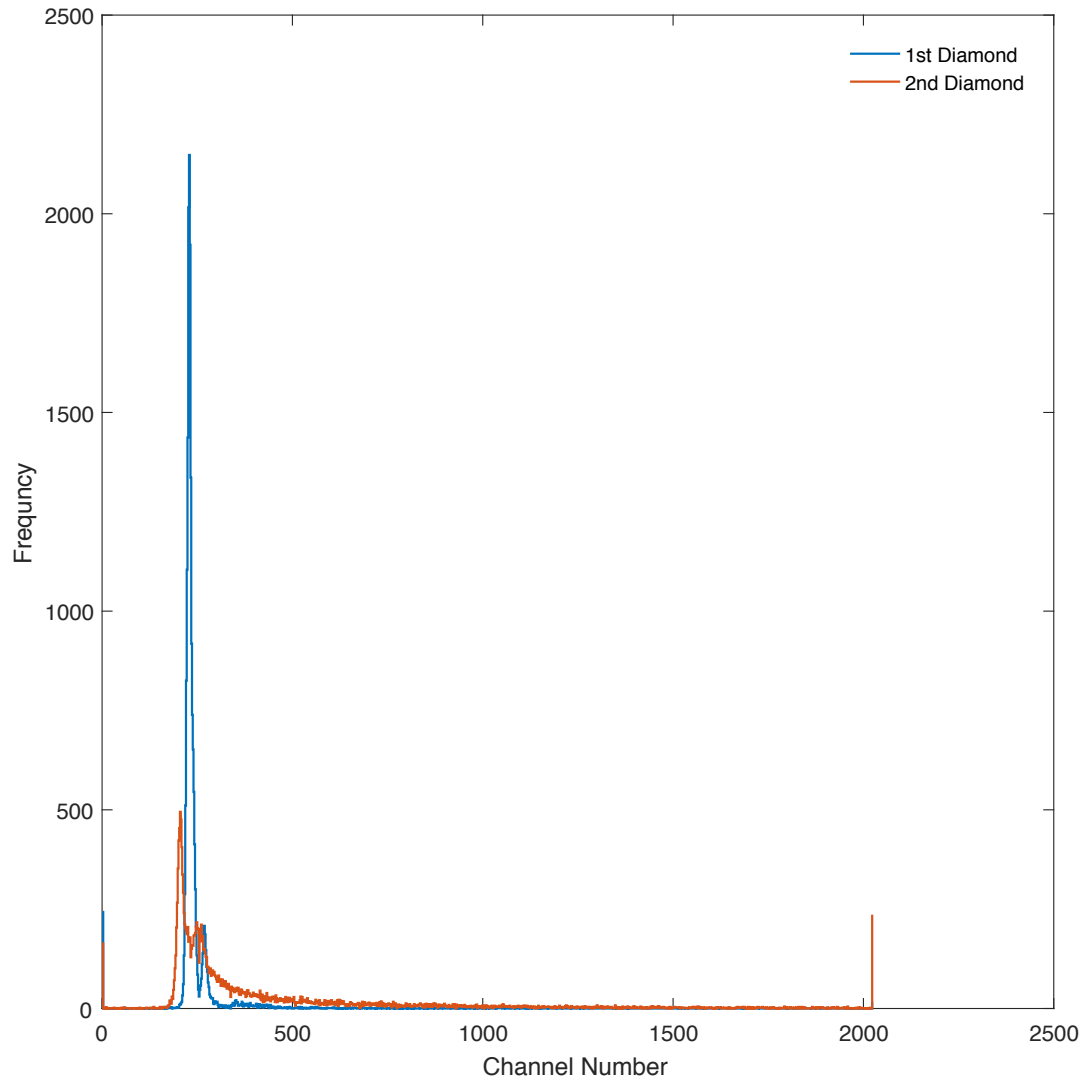


Figure A.1: $\Delta E/\Delta E$ spectral analysis of 2.5 GeV proton beam.

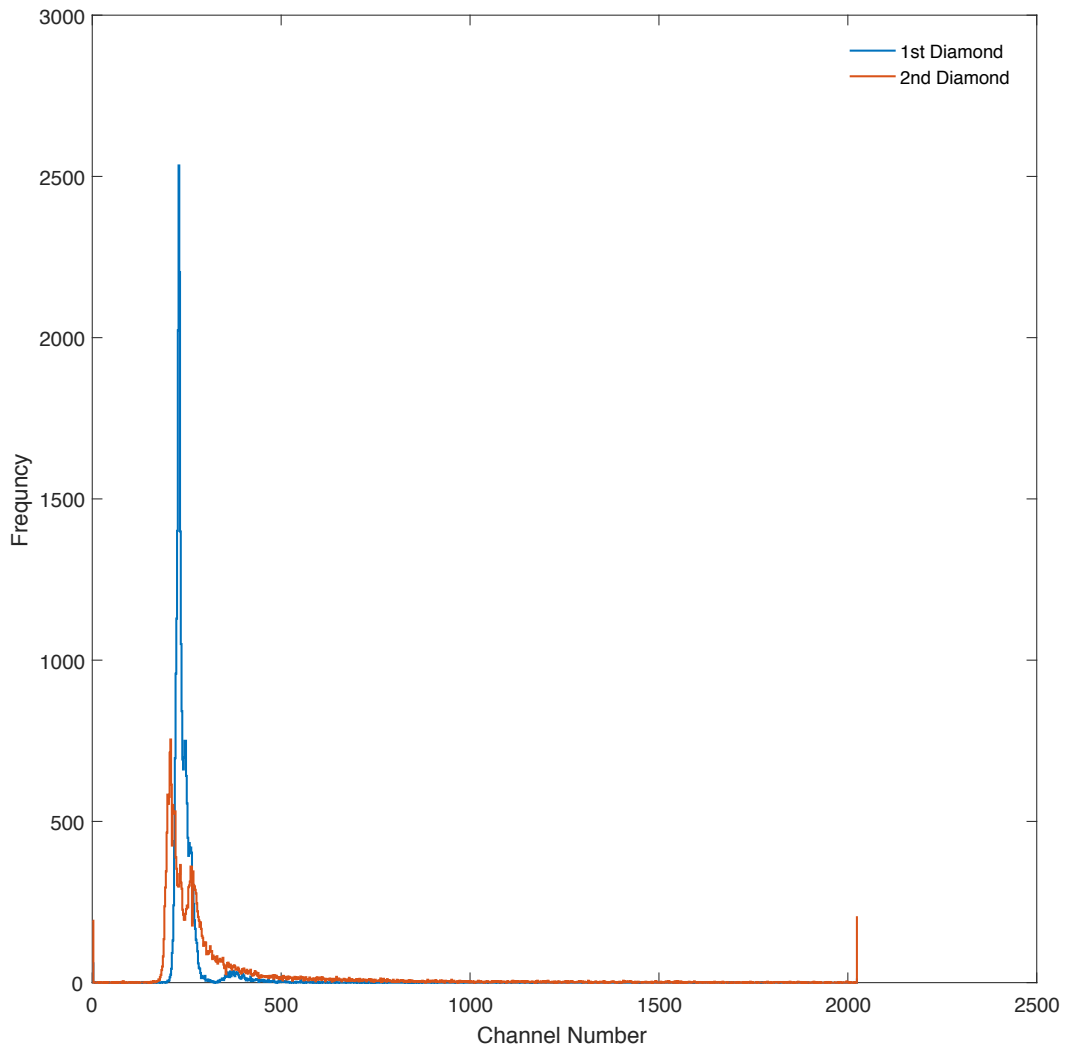


Figure A.2: $\Delta E/\Delta E$ spectral analysis of 800 MeV proton beam.

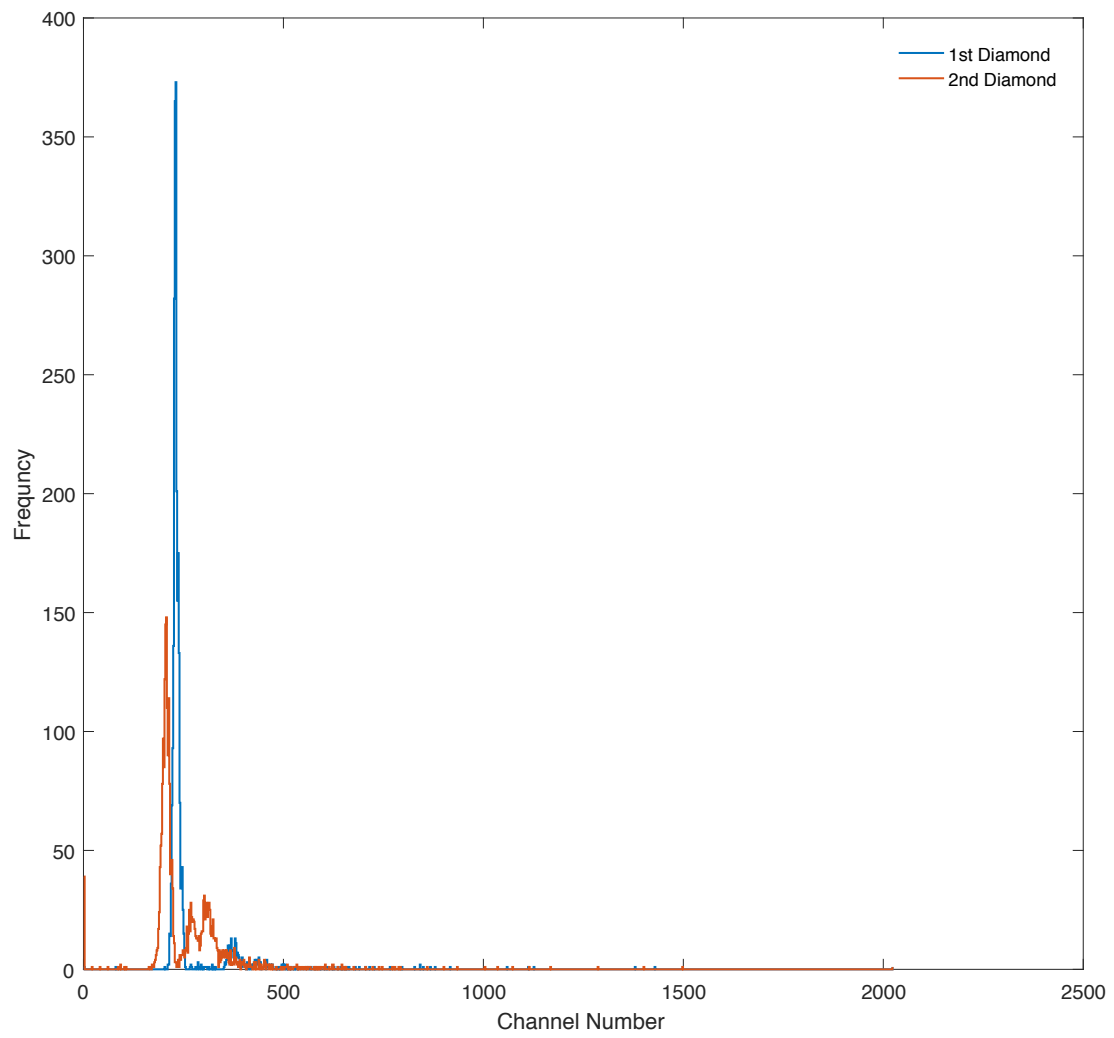


Figure A.3: $\Delta E/\Delta E$ spectral analysis of 400 MeV proton beam.

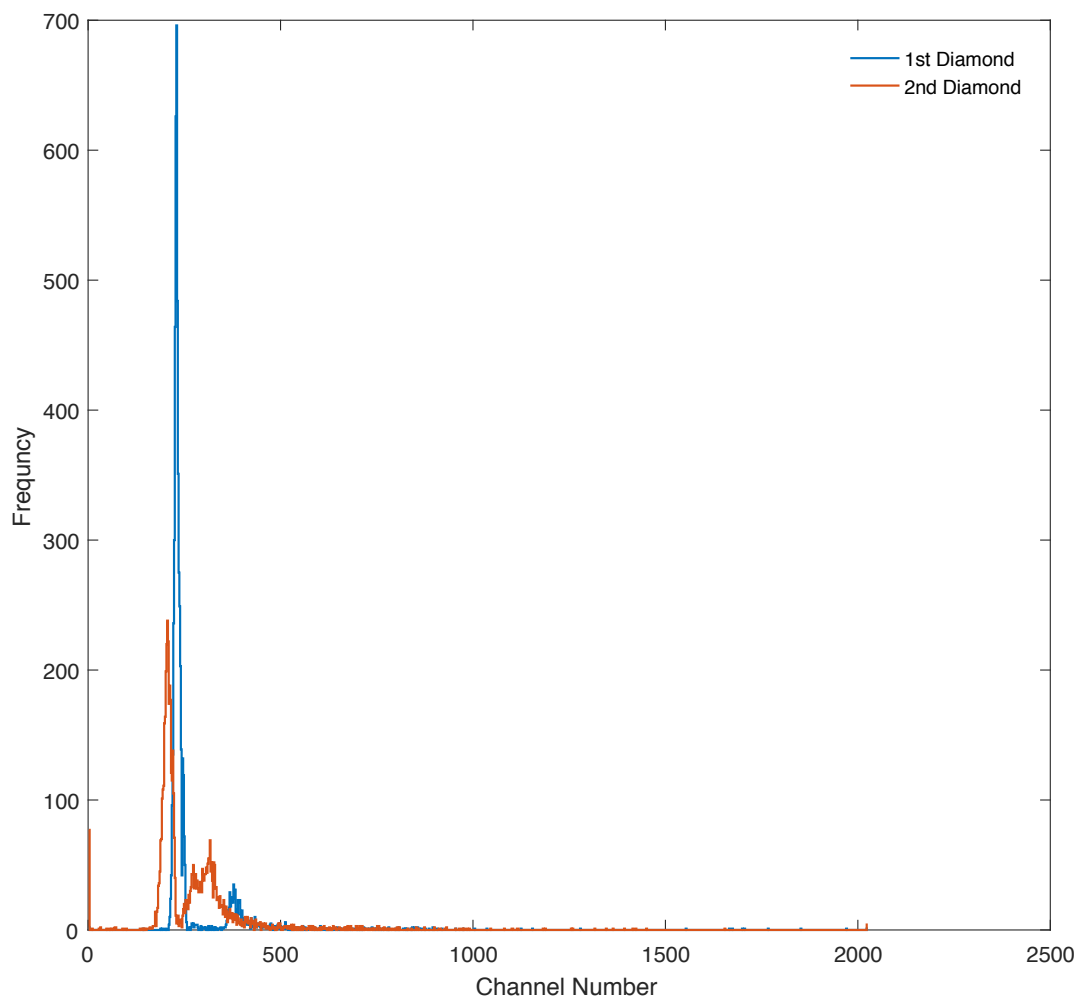


Figure A.4: $\Delta E/\Delta E$ spectral analysis of 400 MeV iron beam.

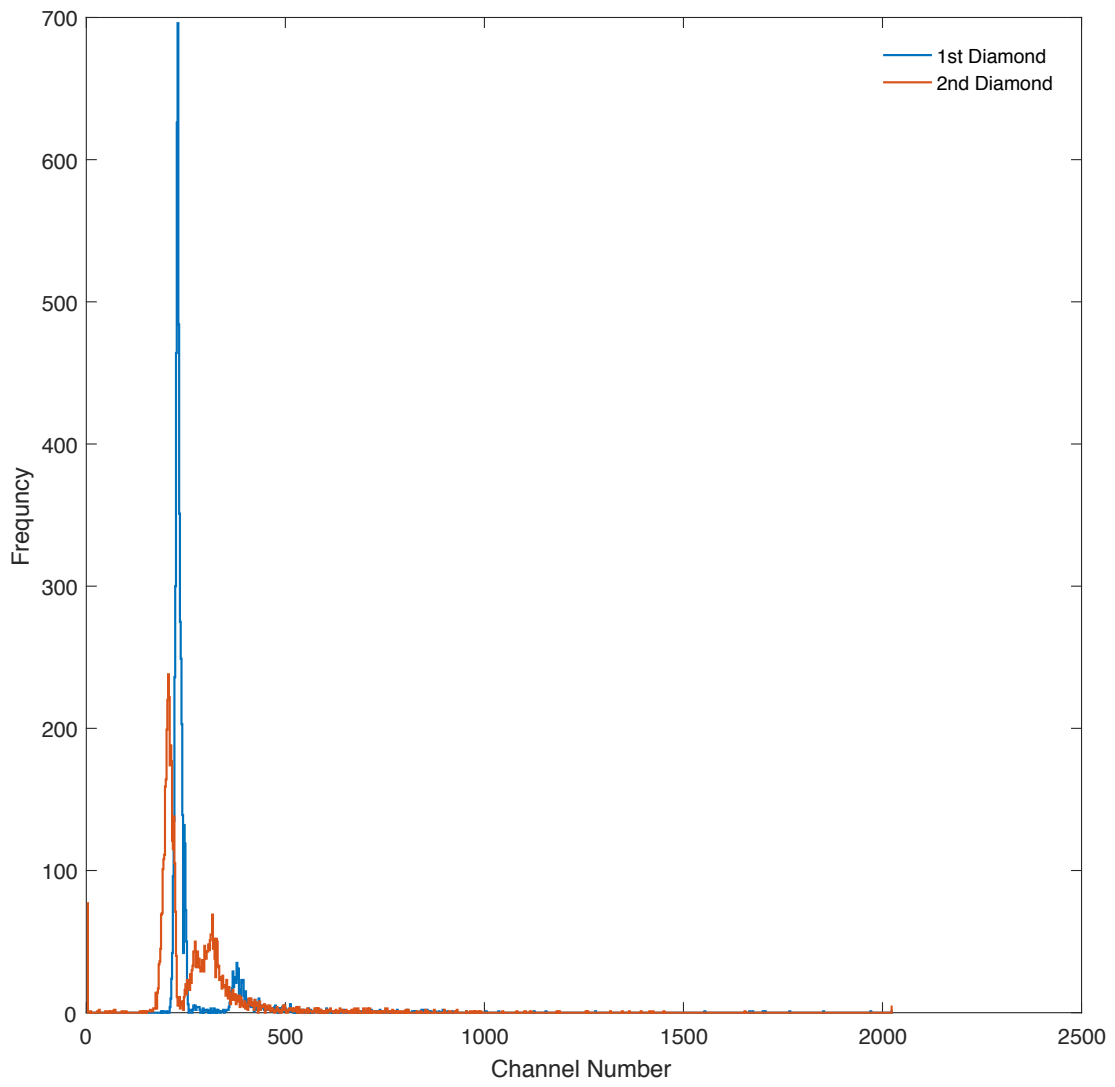


Figure A.5: $\Delta E/\Delta E$ spectral analysis of 800 MeV iron beam.

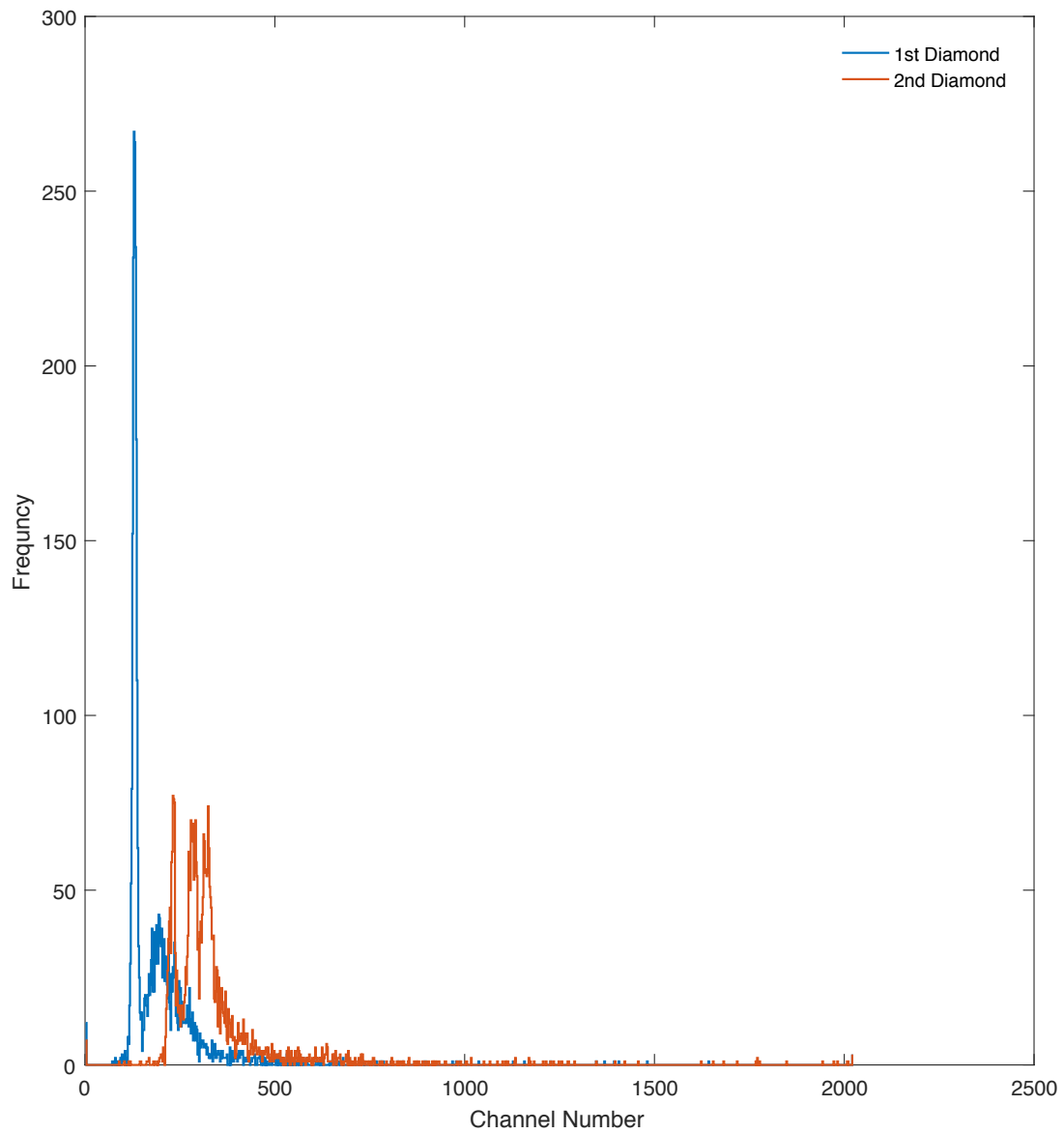


Figure A.6: $\Delta E/\Delta E$ spectral analysis of 1474 MeV iron beam and 400 and 800 MeV helium beams

Vita

Ahmed A. Alghamdi is an engineer from Saudi Arabia. He gained a bachelor of science in Electrical Engineering from Umm Al-Qura University in 2009. After one year, he earned a full scholarship from his Saudi government for pursuing a Master and PhD in Nuclear Engineering. In 2011, he moved to the United States for that purpose. He attended Missouri University of Science and Technology where he completed his Master of Science in Nuclear Engineering in 2013. Later that year he relocated to Knoxville, Tennessee, in pursuit of a Ph.D. in Nuclear Engineering. He studied under Dr. Eric Lukosi, researching novel applications using diamond detectors. He earned a Doctor of Philosophy in Nuclear Engineering in May 2018.